Titre: Title:	Silicon-Integrated GeSn Mid-Infrared Emitters : Theoretical Modeling and Device Demonstration
Auteur: Author:	Gérard Tanguy Eric Gnato Daligou
Date:	2021
Type:	Mémoire ou thèse / Dissertation or Thesis
Référence: Citation:	Daligou, G. T. E. G. (2021). Silicon-Integrated GeSn Mid-Infrared Emitters : Theoretical Modeling and Device Demonstration [Master's thesis, Polytechnique Montréal]. PolyPublie. https://publications.polymtl.ca/9954/

POLYTECHNIQUE MONTRÉAL
affiliée à l'Université de Montréal

Silicon-Integrated GeSn Mid-Infrared Emitters : Theoretical Modeling and Device Demonstration

GÉRARD TANGUY ERIC GNATO DALIGOU
Département de génie physique

Mémoire présenté en vue de l'obtention du diplôme de *Maîtrise ès sciences appliquées*
Génie physique

Décembre 2021

POLYTECHNIQUE MONTRÉAL
affiliée à l'Université de Montréal

Ce mémoire intitulé :

Silicon-Integrated GeSn Mid-Infrared Emitters : Theoretical Modeling and Device Demonstration

présenté par **Gérard Tanguy Eric Gnato DALIGOU**
en vue de l'obtention du diplôme de *Maîtrise ès sciences appliquées*
a été dûment accepté par le jury d'examen constitué de :

Stéphane KÉNA-COHEN, président
Oussama MOUTANABBIR, membre et directeur de recherche
Eoin O'REILLY, membre externe

DEDICATION

To my family and all the people who have been on this intellectual journey...

ACKNOWLEDGEMENTS

First and foremost, I would like to express my deepest gratitude to my supervisor, Professor Oussama Moutanabbir, for his invaluable guidance over the last two years. I am also grateful to him for allowing me to join the Nano and Quantum Semiconductors (NQS) Laboratory. I truly admire his dynamism, his diligence in research, as well as his critical and creative thinking. All these qualities combined with his perception of the academic research environment inspired me and helped me reaffirm my desire to pursue a career in academia.

It is a real pleasure to be part of the stimulating working environment that is the NQS group. All the interactions and collaborations with the different members were very beneficial for me. Thus, I would like to thank all of my colleagues and friends. I especially want to thank Anis and Patrick for their guidance and the thoughtful discussions about the multi-band ***k.p*** formalism. I would not have been able to establish the theoretical framework without their help. I would also like to express my tremendous appreciation to Mahmoud for his generous help and training in the fabrication and characterization of light-emitting devices. Thanks to him and Cédric, I acquired a set of skills that would still benefit me beyond my candidature. All these experimental studies would not have been possible without the GeSn samples grown and provided by Simone. I would therefore like to thank him for that. I would also like to acknowledge his answers to my naive questions, which helped me write about the CVD growth process. Moreover, I would like to thank the jury members for their time and comments on my thesis.

Finally, I would like to highlight my appreciation to both Polytechnique Montréal and Ecole Polytechnique in France for the double degree opportunity. Last but not least, I would like to thank my family members for their support and encouragement from overseas and all of my friends here, in France and Ivory Coast.

RÉSUMÉ

Le développement de technologies de plus en plus innovantes combiné à notre insatiable appétit pour les données conduit à une demande grandissante en bandes passantes et une consommation excessive d'énergie par les centres de données. Cette énorme consommation d'électricité se traduit majoritairement par une dissipation d'énergie sous forme de chaleur aussi bien néfaste pour l'environnement que pour les dispositifs électroniques eux-même. L'introduction de la photonique intégrée sur silicium (Si), compatible avec la technologie CMOS, a été proposée pour remédier à ces problèmes. Cependant, le développement de dispositifs photoniques efficaces et performants reste une tâche ardue du fait de la bande interdite indirecte du Si et du germanium (Ge). En effet, cette propriété limite sévèrement les taux d'émission et d'absorption de ces matériaux, les rendant donc inefficaces. Dans le but de trouver une solution à cette inefficacité, la piste des alliages semi-conducteurs du groupe IV a récemment été explorée. Les alliages de germanium-étain (GeSn) par exemple, présentent une possibilité d'obtenir une bande interdite directe ajustable en fonction de la composition de Sn et de la contrainte appliquée au matériau. Ils ont et continuent de susciter énormément d'intérêt aussi bien du point de vue théorique pour une meilleure compréhension de leurs propriétés optiques que du point de vue expérimental pour la conception de dispositifs.

Dans cette optique, un cadre théorique est développé pour étudier les propriétés de luminescence des alliages de GeSn. Il s'appuie sur le modèle $\boldsymbol{k.p}$ à huit bandes, combiné à l'approximation de la fonction d'enveloppe (EFA) pour estimer les spectres d'absorption et d'émission spontanée d'un matériau massif unique. Contrairement au modèle de densité conjointe d'états (JDOS), dans lequel l'élément de matrice de quantité de mouvement est considéré constant, les forces des transitions optiques sont explicitement calculées dans notre modèle. On montre également qu'elles dépendent du vecteur d'onde $\vec{\boldsymbol{k}}$ et de la polarisation du champ électromagnétique incident. En outre, une méthode relativement simple est utilisée pour estimer les intégrales sur la première zone de Brillouin. Cette approche tient compte explicitement de l'impact de la déformation du réseau sur les directions dites représentatives de l'espace réciproque.

Ensuite, le modèle développé est utilisé pour étudier les propriétés de photoluminescence (PL) des couches de GeSn déformées et relaxées. Les différences entre notre approche et le modèle JDOS ont été mises en évidence à chacune des étapes du calcul. En outre, il a été démontré que le modèle décrit efficacement les observations expérimentales, et une valeur de $\sim 1,6\,\text{ns}$ a été extraite à 4 K pour la durée de vie radiative des porteurs en régime permanent (τ_{rad}) de

l'échantillon de $Ge_{0.83}Sn_{0.17}$ déformé. Cette durée de vie augmente tout en restant de l'ordre des ns sur la gamme de température de 4-80 K. De plus, il a été démontré que la relaxation du réseau cristallin augmente τ_{rad}. Par exemple, il a été montré que τ_{rad} évolue suivant la loi de puissance $a + bT^c$ avec des valeurs de c autour de $2,27$ pour le matériau relaxé et $1,97$ pour le matériau déformé. A 80 K, la valeur de $\sim 9,5$ ns est atteinte pour τ_{rad}(relaxé), alors que τ_{rad}(déformé) est $\sim 3,5$ ns. Ces résultats mettent en avant la possibilité d'utiliser notre cadre théorique pour la description des propriétés physiques des alliages de $Ge_{1-x}Sn_x$.

Enfin, des diodes électroluminescentes ont été fabriquées à partir de couches *p-i-n* à double hétérostructures de GeSn avec une couche intrinsèque de contenant 9,4% de Sn. Ces dispositifs ont des diamètres variables dans l'intervalle 20-160 µm. Leurs performances ont été étudiées en effectuant des mesures I-V dans des conditions d'obscurité à 300 K. L'un des résultats que l'on peut extraire de ces mesures est le claquage atteint par le dispositif de 40 µm de diamètre à seulement 11 V. En outre, une émission d'électroluminescence à environ ~ 2.5 µm est démontrée à 300 K et il est prouvé qu'elle résulte de la recombinaison des porteurs à l'intérieur de la couche intrinsèque à bande interdite directe. De plus, un épaulement assez intriguant a été observé autour de 0.54 eV dans les spectres d'émission. Son origine a été étudiée en réalisant des mesures de PL en fonction de la température, mais aucune explication concrète n'a été trouvée.

Les résultats de cette thèse mettent en évidence le potentiel du GeSn en tant que matériau efficace et adéquat pour l'intégration monolithique de la photonique et de la microélectronique au Si, recherchée depuis longtemps. De plus, ils soulignent le besoin de modèles théoriques et de simulations de plus en plus précis pour espérer développer des dispositifs efficaces à base de GeSn.

ABSTRACT

The insatiable desire for data fueled by the continuous development of new highly connected technologies leads to an input/output bottleneck and excessive energy consumption by the data centers. This tremendous electricity consumption results mainly heat generation, which represents a major issue for the environment and for the electronic devices themselves. Silicon (Si) integrated photonics, compatible with the CMOS processing technologies, has been proposed as a viable solution to extend the bandwidth and reduce power consumption. However, developing efficient and effective Si-based photonic devices is still one of the most arduous tasks to perform due to the indirect bandgap of both Si and germanium (Ge). Indeed, this property severely limits their emission and absorption rates, therefore making them inefficient. Group IV semiconductors alloys have been recently explored as possible materials to overcome this limitation. The Germanium-Tin (GeSn) alloys, for instance, may have a bandgap energy that is adjustable depending on the Sn composition and the lattice strain. They have been attracting a great deal of interest both from the theoretical standpoint for a better understanding of their physical properties and from the experimental side for designing and fabricating efficient devices.

With this perspective, a theoretical framework is developed to investigate the luminescence properties of GeSn alloys. This framework relies on the band structure of these materials obtained within the eight-band $\boldsymbol{k.p}$ formalism and combined with the envelope function approximation (EFA) to estimate the absorption and spontaneous emission spectra of single bulk material. Unlike the joint density of states (JDOS) model, in which the momentum matrix element is considered constant, the oscillator strengths are explicitly computed in our model. They are also shown to be dependent on the wave vector $\vec{\boldsymbol{k}}$ and the polarization of the incident electromagnetic field. Furthermore, a simple though accurate method is used to compute the integrals over the first Brillouin zone (BZ). This approach accounts explicitly for the impact of the lattice strain on the representative directions of the $\vec{\boldsymbol{k}}$-space.

Next, using the framework mentioned above, the photoluminescence (PL) properties of both strained and relaxed GeSn were investigated. The differences between our approach and the JDOS model were highlighted at each step of the computations. Besides, the model was shown to fit the experimental data, and a value of $\sim 1.6\,\text{ns}$ was extracted at 4 K for the steady-state radiative carrier lifetime (τ_{rad}) of the as-grown $Ge_{0.83}Sn_{0.17}$ sample. This lifetime increases with the temperature while staying in the order of ns over the 4-80 K temperature range. Furthermore, the strain relaxation in the material was shown to increase τ_{rad}. For

instance, τ_{rad} is shown to evolve following the power-law $a + bT^c$ with a value of c around 2.27 for the strained-relaxed material compared to 1.97 for the as-grown material. At 80 K, the value of $\sim 9.5\,\text{ns}$ is reached for τ_{rad}(relaxed), while τ_{rad}(as-grown) is $\sim 3.5\,\text{ns}$. These results show the possibility of using the framework to describe the physical properties of $Ge_{1-x}Sn_x$ materials.

Finally, light-emitting devices (LEDs) were fabricated from GeSn *p*-*i*-*n* double heterostructures with an *i* layer of 9.4% Sn. These devices have varying diameters in the 20-160 µm range. Their performance was investigated with I-V measurements under dark conditions at 300 K. One of the results of these measurements was the breakdown reached by the 40 µm diameter device at just 11 V. Besides, an electroluminescence emission at around $\sim 2.5\,\mu\text{m}$ was demonstrated at 300 K and proved to result from the carrier's recombination inside the direct bandgap *i*-layer. Furthermore, an intriguing shoulder around 0.54 eV was observed in the emission spectra. Its origin was studied using temperature-dependent PL, but no concrete explanation was extracted.

The results in this thesis highlight the potential of GeSn as an effective material system for the monolithic integration of photonics with Si microelectronics. Additionally, they stress the need for more accurate theoretical models and simulations for developing efficient GeSn devices.

TABLE OF CONTENTS

LIST OF TABLES

LIST OF FIGURES

LIST OF SYMBOLS AND ACRONYMS

AP	Atmospheric Pressure
APD	avalanche photodiode
BL	Bottom Layer
BOE	Buffered Oxide Etch
BZ	Brillouin Zone
CMOS	Complementary Metal-Oxide-Semiconductor
CVD	Chemical Vapor Deposition
CW	Continuous Wave
DH	Double Heterostructure
EBL	Electron Beam Lithography
EFA	Envelope Function approximation
EL	Electroluminescence
FTIR	Fourier Transform Infrared
FWHM	Full Width at Half Maximum
ICP	Inductively Coupled Plasma
IoT	Internet of Things
IPA	IsoPropyl Alcohol
IVBA	Inter-Valence Bands Absorption
JDOS	Joint Density Of States
LED	Light-Emitting Device
LP-CVD	Low-Pressure Chemical Vapor Deposition
MBE	Molecular Beam Epitaxy
ML	Middle layer
MQW	Multi Quantum Wells
MWIR	Mid-Wave Infrared
NIR	Near-Infrared
OEIC's	Optoelectronic Integrated Circuits
PBA	Parabolic Band Approximation
PECVD	Plasma Enhanced Chemical Vapor Deposition
PIC	Photonic Integrated Circuit
PL	Photoluminescence
PVD	Physical Vapor Deposition
QW	Quantum Wells

RF	Radio-Frequency
RIE	Reactive Ion Etching
RP	Reduced-pressure
RSM	Reciprocal space mapping
SBEMA	Single-band effective mass approximation
SLA	Special-lines approximation
SRH	Shockley-Read-Hall
SWIR	Short-Wave Infrared
TE	Transverse electric
TL	Top layer
TM	Transverse magnetic
UHV	Ultra-High Vacuum
VS	Virtual Substrate
XRD	X-ray Diffraction

LIST OF APPENDICES

CHAPTER 1 INTRODUCTION

We live in an era in which the appetite for data is growing exponentially with no signs of slowing down. Cloud computing, 5G networks, mobile data traffic, cryptocurrencies, or the so-called internet of things (IoT): all these technologies have been fueling the insatiable desire for data and higher bandwidth. The increasing number of internet users results in the exponential growth of the global data traffic, which is expected to increase from 33 ZB in 2018 to 175 ZB in 2025[1] [6].

The availability of faster and smarter devices has brought telecommunications and information technology to a new age. Cloud computing allows the users to harness the power of online storage and supercomputers to have real-time access to products and services and run nearly every aspect of their lives. 5G technology should enable a massive number of IoT devices to connect and communicate with one another, and therefore be reliable for applications such as self-driving cars. However, this need for vast access to data puts stress on data centers and leads to considerable energetic and environmental costs. For instance, data centers were predicted to use between 196 TWh and 400 TWh in 2020 (1-2% of the global electricity demand) [7, 8]. With the impact of the COVID-19 pandemic and the perpetual need for data, there is no doubt that the energy consumption would still increase if no efficient solution is found. It should be noted that the power consumed by the data centers is, for the most part, converted into heat by the servers. Different techniques have been exploited to efficiently use the excess thermal energy generated and keep the servers to optimum temperatures. However, a more viable solution would be to develop more energy-efficient devices for the telecommunications industry.

One promising solution proposed to overcome the limitations discussed above is the introduction of the photonic integrated circuits (PICs) technology. Optical and optoelectronic technologies have been used since the mid-90s to transfer data over long distances via optical fibers [9]. However, there are still some challenges to implementing optical interconnects at the chip level. Indeed, the development of optical communications for chip-to-chip applications requires low power dissipation, small latency, high levels of integration, and high-volume manufacturability [10]. These conditions imply that the fabrication of PICs should be compatible with the conventional silicon integrated circuit infrastructure, i.e., the complementary metal-oxide-semiconductor (CMOS) technology. PICs circuits generally include devices such as photodetectors and light-emitting sources. Developing such components requires materials

[1] $1\,\mathrm{ZB} = 10^{21}$ bytes

with efficient light absorption and emission, and therefore with good optical properties. Silicon (Si) and Germanium (Ge) have rather poor optical properties due to their indirect bandgap. On the other hand, III-V semiconductors such as GaAs, InP, GaAs, or GaN have a direct bandgap. This property has been exploited for developing high-gain lasers and efficient photodetectors [11]. These devices have been integrated over the silicon platform either via wafer bonding (heterogeneous integration) or butt-coupling (hybrid approach) [12–16]. However, these techniques result in the higher price of complicated packaging and higher interconnect parasitic capacitance [17]. On top of that, III-V substrates also suffer from their limited scalability, which prevents high-volume manufacturing. The monolithic integration of optical components based on group IV semiconductors with silicon electronics could offer cost advantages and ease of integration with the CMOS technology [18].

For the monolithic integration to be effective, the limitations imposed by the indirect bandgap of Si and Ge have to be overcome. It has been reported that the bandgap directness of Ge can be tuned with tensile strain and n-type doping [19, 20]. These approaches resulted in the demonstration of Ge-on-Si lasers and light-emitting diodes operating at room temperature with a biaxial tensile strain value of $\sim 0.25\%$ and n-type doping level in the order of $10^{19} - 10^{20}\,\mathrm{cm}^{-3}$ [21–25]. However, these lasers could not be practical due to the extremely high thresholds ($\geq 100\,\mathrm{kA/cm}^2$) and their very poor efficiencies. Ge photodetectors with good coverage of the C-band ($1530 - 1565\,\mathrm{nm}$) have also been demonstrated [26]. However, their efficiency drops significantly in the L-band ($1565 - 1625\,\mathrm{nm}$). Besides tensile strain and doping, alloying Ge with tin (Sn) can also result in direct bandgap semiconductors. This potential has motivated tremendous efforts to investigate the GeSn material system and develop all-group IV optoelectronic devices.

Besides the potential of GeSn in optical communications, this material system can also benefit other sectors. One of the key properties of GeSn materials is the tunability of the bandgap energy in the short-wave infrared (SWIR)[2] to mid-wave infrared (MWIR)[3] range. This property can be exploited to develop devices for sensing and spectroscopy applications [18, 27].

Given the potential of the GeSn material system and the set of possible applications, more investigation should be done to identify, estimate and optimize the required parameters to develop efficient devices. The current work contributes a part to the study of the optoelectronic properties of GeSn semiconductors. The aim is to provide an accurate theoretical and numerical framework to describe the luminescence properties of the $\mathrm{Ge}_{1-x}\mathrm{Sn}_x$ semiconductors. The fabrication and characterization of GeSn light emitters are also investigated. The thesis is

[2]SWIR: $1.5 - 3\,\mu\mathrm{m}$
[3]MWIR: $3 - 8\,\mu\mathrm{m}$

organized into seven chapters. Chapter 2 provides an overview of the progress observed in the GeSn material system and describes the current state-of-the-art of the field. Chapter 3 presents the mathematical and physical ideas used to describe the luminescence properties of GeSn structures. While chapter 4 gives a general description of the experimental methods and techniques used in this work, the main results are the subject of the following three chapters. Indeed, chapter 5 presents detailed analyses of the $Ge_{0.83}Sn_{0.17}$ optical properties using the theoretical framework from chapter 3. The values of the radiative carrier lifetime are extracted from these analyses. The fabrication and characterization of GeSn-based light emitters are included in chapter 5. Finally, chapter 6 summarizes the work and discusses research perspectives. The appendices at the end present different calculations about the carrier dynamics and the recombination mechanisms.

CHAPTER 2 LITERATURE REVIEW

It was as early as 1982 when the idea of allowing Sn with Germanium to form a possible direct bandgap group IV semiconductor was theoretically elaborated [28]. Despite the bandgap directness and the enhanced mobility presented, GeSn remained for a long time a speculative material mainly because of the very low solid solubility of Sn in Ge [29]. Many attempts to circumvent this limitation were presented in the literature [30]. However, it was not until the beginning of this century that a direct bandgap GeSn, as well as the first optically injected GeSn laser, were experimentally demonstrated [31]. These achievements led to more GeSn-based optical devices, including light emitters and photodetectors [18, 32].

This chapter is meant to give a general overview of the progress of the GeSn material system. By reviewing the electronic and optical properties of the material, this chapter highlights the advances and the shortcomings of various GeSn-based devices.

2.1 GeSn as a direct bandgap semiconductor

$Ge_{1-x}Sn_x$ semiconductors have been attracting a great deal of interest in recent years because of their potential to achieve the monolithic integration of photonics with Si microelectronics. Whereas Si and Ge are indirect bandgap semiconductors, the diamond cubic Sn[1] (α-Sn) is a semimetal with an inverted band structure at the Γ point (see figure 2.1).

Allowing Sn with Ge is predicted to lower the conduction bands at both the Γ and the L valleys. However, the decrease at the Γ valley is estimated to be faster, as presented in figure 2.2. In that case, a direct bandgap semiconductor should be obtained for higher Sn compositions. Indeed, using the virtual-crystal approximation (VCA) and a second-nearest-neighbor tight-binding model, Jenkins and Dow predicted the transition from an indirect to a direct bandgap material to occur at a Sn content of ~ 20 at.% [33]. A few years later, in 1989, Mäder et al. reported the higher value of 26 at.% [34]. More recent studies estimated the crossover to be as low as 6 at.% for unstrained $Ge_{1-x}Sn_x$ materials [35, 36].

[1] Sn has two main allotropes. The gray tin (α-Sn), stable at temperatures below 13 °C, crystallize in the diamond structure while white tin (β-Sn), the more familiar and stable form at room temperature, is tetragonal [28]. With a crystalline structure similar to that of Ge, α-Sn is the material of choice for the synthesis of GeSn alloys. For the sake of simplification, α-Sn will be referred to as Sn in the following parts of the document.

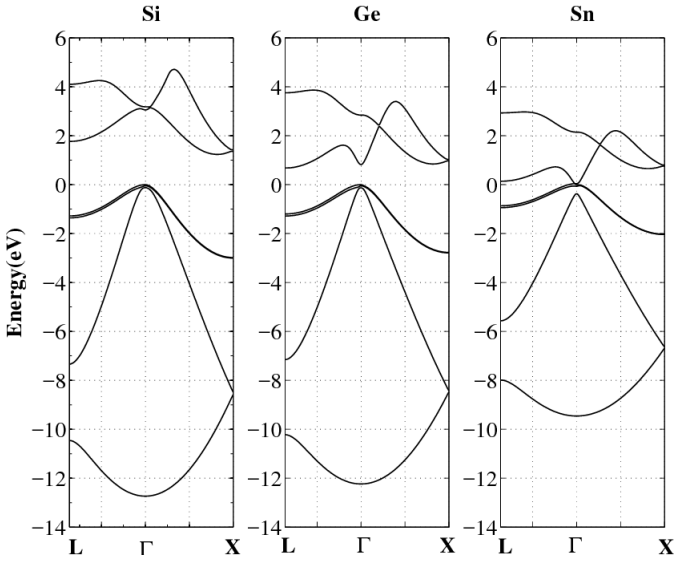

Figure 2.1 Calculated electronic bandstructure of Si, Ge, and α-Sn [1]. © IOP Publishing. Reproduced with permission. All rights reserved.

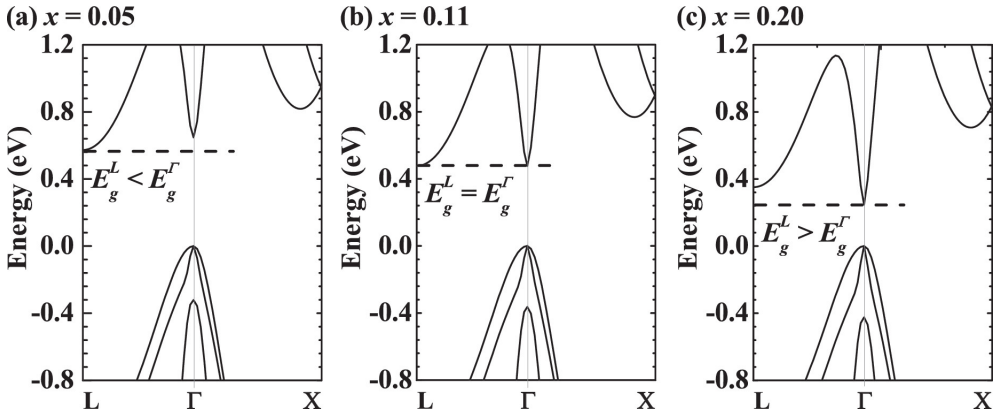

Figure 2.2 Electronic band structures of $Ge_{1-y}Sn_y$ for (a) $y = 0.05$, (b) $y = 0.11$, and (c) $y = 0.20$, showing the transition from indirect [panel (a)] to direct bandgap [panel (c)]. Reprinted from [2] , with the permission of AIP Publishing.

Furthermore, the value of the crossover point was found to depend on the strain in the material [35, 37, 38]. Indeed, compressive biaxial strain is shown to influence the band structure of Ge oppositely compared to the incorporation of Sn [35]. In that case, an increase of compressive strain moves the indirect-to-direct transition to larger Sn composition. However, as presented in section 2.2, the growth of GeSn even with a Sn content of 6 at.% is not trivial.

2.2 Epitaxial growth of GeSn alloys

The epitaxial growth of GeSn presents multiple challenges which had limited the progress of the early studies. One of the main challenges is the difficulty to grow high-quality single-crystalline direct bandgap GeSn due to the equilibrium solid solubility of Sn being as low as 1 at.% in Ge [29]. Additionally, Sn has a strong tendency to segregate to the surface and undergo a transition from its α phase to the β phase (metallic) at above 13.2 °C [39, 40].

Soon after Goodman's work, Oguz et al. reported, in 1983, the synthesis of the first microcrystalline GeSn thin films using pulsed UV laser crystallization [41]. Later in 1987, the deposition of monocrystalline $Ge_{1-x}Sn_x$ layers with x up to 8 at.% by bias sputtering deposition on Ge(100) and GaAs(100) was demonstrated [42]. Besides these studies, and despite the challenges, the growth of GeSn epi-layers was achieved using various physical vapor deposition (PVD) techniques such as solid-phase epitaxy [43–45], pulsed laser deposition [46], and sputtering [47]. However, it was mainly the epitaxial processes using molecular beam epitaxy (MBE) [39, 40, 48–56] and chemical vapor deposition (CVD) [57–61] that motivated the revived interest in the GeSn material system. While MBE was the method of choice until the 1990s, for the epitaxial growth of GeSn with appropriate crystalline quality [56, 62], it failed to offer device quality films due to the very low growth temperatures ($100 - 200$ °C), the formation of dislocation defects, and the limited layer thickness required for monocrystalline growths [63]. On the other hand, CVD offers the possibility of selective growth, uniform deposition over large wafers, and higher growth rates [63]. However, the lack of suitable Sn precursors prevented the epitaxial growth of GeSn layers using CVD for many years. In 2001, Taraci et al. reported the first GeSn epi-layers containing up to 25 at.% Sn, grown directly on Si in an ultra-high vacuum (UHV)-CVD reactor using $C_6H_5SnD_3$ and Ge_2H_6 as Ge and Sn precursors, respectively [64]. Later in 2011, Vincent et al. introduced the stable and commercially available tin-tetrachloride ($SnCl_4$) as Sn precursor and achieved the epitaxial growth of high-quality $Ge_{0.92}Sn_{0.08}$ layers in atmospheric pressure (AP)-CVD environment [65]. The development of accessible, cost-effective, and stable chemicals precursors for both Sn ($SnCl_4$) and Ge (Ge_2H_6, GeH_4) opened the way to the growth of monocrystalline GeSn epi-layers using a broad range of CVD techniques such as AP-CVD [66, 67], and reduced-pressure (RP)-CVD [61, 68–72].

The epitaxial growth of GeSn on Si is performed using a Ge-virtual substrate (VS) as an interlayer [68]. For that reason, the grown layers are typically compressively strained. This strain accumulation was found to induce a composition gradient as the layer grows thicker [69, 73]. The use of intermediate GeSn multi-layer heterostructure has been demonstrated to be efficient for the growth of layers with uniform and high Sn content (10-20 at. %

range) [61, 68, 74].

2.3 GeSn-based optoelectronic devices

The epitaxial growth of high-quality GeSn materials enabled the development of group IV optoelectronic devices. Indeed, the availability of these materials enabled the demonstration of direct bandgap emissions in the SWIR and MWIR ranges [5, 31, 61]. These emissions served as building blocks for more elaborated Silicon-compatible GeSn-based light emitters.

2.3.1 Light emitters

In 2015, the first demonstration of an optically pumped GeSn laser emitting at a wavelength of $\sim 2.3\,\mu m$ was reported [31]. Fabricated from a sample of 560 nm thick layer of $Ge_{0.874}Sn_{0.126}$, grown on a Ge-VS/Si(001) substrate, the 5-µm-wide and 1-mm-long Fabry-Perot waveguide cavities represented a promising result towards the integration of silicon optoelectronic devices. However, they suffered from their low operation temperature ($T \leq 90$ K) and the high threshold excitation density of $\sim 325\,kW/cm^2$. These issues combined with the pulsed optical pumping prevented the use of this GeSn laser for practical applications [75].

Since then, substantial progress has been made to reach higher operation temperatures. For instance, Zhou et al. showed an optically pumped $Ge_{0.80}Sn_{0.20}$ edge-emitting laser based on the ridge and planar waveguide structures [76]. Even though they demonstrated a near-room temperature operation, it was at the expense of the threshold excitation density, which was about $796\,kW/cm^2$ at the maximum operating temperature of 270 K for the 100 µm wide ridge structure. Similarly, Chretien et al. reported an optically pumped GeSn-based laser with an operating temperature up to 273 K and a high lasing threshold of $\sim 2\,MW/cm^2$ [77]. Going from a step-graded GeSn epitaxial stack encapsulated by two SiGeSn barriers, they designed tensile-strained and free-standing microbridges placed between broadband mirrors to offer optical feedback.

Different attempts to improve the lasing threshold were also presented in the literature. Indeed, Stange et al. investigated the lasing properties of undercut microdisks cavities fabricated from SiGeSn/GeSn multi Quantum Wells (MQW) heterostructures [78]. They reported a lasing threshold on the order of $35\,kW/cm^2$ with a 1064 nm pump [79]. However, a maximum operating temperature of 120 K was found due to the limited bandgap directness of the 13 at.% GeSn alloy used for the wells. Furthermore, a significant reduction of the laser threshold was demonstrated using a highly tensile strained (1.4%), 5.4 at.% GeSn material [80]. The choice of a GeSn material with a low Sn composition in this study is justified by the relatively

low density of misfit dislocations and impurities at the interface with Germanium which is shown to scale with the Sn content and to contribute to the high pumping levels required to achieve lasing [66, 78]. The initially indirect bandgap $Ge_{0.946}Sn_{0.054}$ was encapsulated with a silicon nitride stressor layer and converted into a direct bandgap optical gain material with a directness $\Delta E_{L-\Gamma}$ of 70 meV. The material quality advantage and the tensile strain combined with processing technology and thermal management enabled lasing with a low threshold of 1.1 kW/cm^2 in continuous wave (CW) operation. However, the lasing operating temperature was limited to 70 K for the CW and 100 K for pulsed operation.

Given all the previous information, it should be noted that GeSn lasers integrating higher operation temperatures, lower thresholds, and CW operation is yet to be found. Improving the growth protocols to achieve higher Sn content while maintaining good material quality should benefit the development of such devices.

In addition to lasers, GeSn-based light-emitting devices (LEDs) have also been demonstrated [81–83]. However, more research is required to improve their performances and reach room temperature operation.

2.3.2 Photodetectors and sensors

As stated in the previous sections, the incorporation of Sn into the Ge lattice enables the tunability of the bandgap in the SWIR to MWIR range. By exploiting this quality of the GeSn material system, photodetectors can be engineered for optical communications, sensing, and imaging applications.

In 2019, a high-speed GeSn/Ge MQW photodiode integrated on a 300 mm Si wafer was demonstrated [84]. This device exhibited a detection cut-off beyond 2 µm, a 3-dB bandwidth above 10 GHz in addition to a low leakage current density of 44 mA/cm^2 (at a reverse bias of 1 V), similar to that of Ge-on-Si photodiodes. The demonstration of a GeSn-on-Si avalanche photodiode (APD) for light detection around 2 µm was also reported [85]. In this device, the separate $Ge_{0.9}Sn_{0.1}$ MQW and Si layers were respectively employed for light absorption and carrier multiplication, resulting in a thermal coefficient of the avalanche breakdown voltage estimated at 0.053 $\%K^{-1}$, smaller than that of APDs with III-V multiplication material.

The fabrication of GeSn-based MWIR detectors is not yet fully explored in the literature; however, recent studies show that GeSn materials can be engineered to cover this wavelength range [68, 86].

This literature review covered the progress observed in the GeSn material system. Despite the material challenges and the discrepancies in the theoretical estimation of the bandgap energy,

the collective efforts of the researchers combined with the availability of suitable commercial precursors enabled the CVD growth of high-quality monocrystalline layers. This milestone led to the demonstration of different optoelectronic devices such as LEDs, photodiodes, as well as optically and electrically pumped GeSn-based lasers. However, many challenges still need to be addressed before achieving the monolithic integration of GeSn on the Si platform. Alternative growth protocols are still required to engineer higher Sn content materials and improve their crystalline quality. The optimization of the microfabrication processes also needs to be addressed to enhance the performance of the devices. From a theoretical point of view, establishing accurate models and simulations is crucial to estimate the properties of the GeSn materials and design more efficient devices. The next chapters suggest possible approaches in terms of the theoretical and numerical estimations of the properties of GeSn. The fabrication of GeSn-based LEDs for room-temperature emission is also studied.

CHAPTER 3 MODELING OF THE LUMINESCENCE PROPERTIES OF GeSn-BASED LIGHT EMITTERS

Semiconductors emit light through carrier pair recombination processes. For an intrinsic semiconductor, at thermal equilibrium, the carriers' densities are fixed by the law of mass action ($np = n_i^2$), and the resulting emission intensity is typically very low. The creation of excess electron-hole pairs could be a solution for increasing this intensity. It could be done by doping the material but, the emission intensity is not expected to increase considerably at thermal equilibrium. Another solution would be to illuminate the material or even bias the device (p-n or p-i-n devices) in order to inject more carriers in the active region and emit some light. These processes are commonly known as photoluminescence (PL) and electroluminescence (EL), respectively. Both of them emerge from the optical and electronic transitions that happen inside the materials. This chapter highlights our effort to better understand the fundamental physics underlying the GeSn luminescence properties.

The luminescence spectrum intensity can be determined using the direct inter-band emission theory and the spontaneous emission spectrum r^{spon} [87]. This parameter is necessary to quantify the rate of photons emitted spontaneously. It is calculated using the Fermi golden rule [88,89] and the perturbation theory as described in equation (3.1) below. In this equation, $n_r e^2/\pi c^3 \varepsilon_0 \hbar^4$ is a material-related constant with e the elementary charge, n_r the refractive index of the material, and c the speed of light in a vacuum. V is the volume of the states in the $\vec{\boldsymbol{k}}$-space. We sum over the different values of $\vec{\boldsymbol{k}}_c$ and $\vec{\boldsymbol{k}}_v$ in the Brillouin zone (BZ) to account for the possible transitions between the conduction and the valence bands. The Dirac delta function limits the transitions to those with an energy difference of $\hbar\omega$, the photon energy. The summations over the spins of the initial states η and the final states σ have been written out explicitly instead of a simple factor of 2. Moreover, $M_{cv}^2(\vec{\boldsymbol{k}}_c, \vec{\boldsymbol{k}}_v) = \left|\left\langle \Phi_c^\eta(\vec{\boldsymbol{k}}_c)\right| \frac{\hbar}{m_0}\hat{\boldsymbol{e}}.\vec{\boldsymbol{p}} \left|\Psi_v^\sigma(\vec{\boldsymbol{k}}_v)\right\rangle\right|^2$ represents the strength of the transition from the state $|\Phi_c^\eta\rangle$ to $|\Psi_v^\sigma\rangle$ with $\hat{\boldsymbol{e}}$ the polarization unit vector and $\vec{\boldsymbol{p}}$ the momentum matrix operator. Finally, we use the Fermi-Dirac statistics to account for the probability occupation of the different states. f is the Fermi-Dirac distribution given by $f(\epsilon, \mu) = \left[1 + \exp\left(\frac{\epsilon-\mu}{k_B T}\right)\right]^{-1}$ in which ϵ is the energy and μ the Fermi-level of the charge carrier described by the function.

$$r^{spon}(\hbar\omega) = \frac{1}{V}(\hbar\omega)\left(\frac{n_r e^2}{\pi c^3 \varepsilon_0 \hbar^4}\right)\sum_{\vec{\boldsymbol{k}}_c,\vec{\boldsymbol{k}}_v}\sum_{\eta,\sigma}\left|\left\langle \Phi_c^{\eta}(\vec{\boldsymbol{k}}_c)\left|\frac{\hbar}{m_0}\hat{\boldsymbol{e}}.\vec{\boldsymbol{p}}\right|\Psi_v^{\sigma}(\vec{\boldsymbol{k}}_v)\right\rangle\right|^2 \times\delta\left(\epsilon_c^{\eta}(\vec{\boldsymbol{k}}_c)-\epsilon_v^{\sigma}(\vec{\boldsymbol{k}}_v)-\hbar\omega\right)f\left(\epsilon_c^{\eta},\mu_e\right)\left[1-f\left(\epsilon_v^{\sigma},\mu_h\right)\right] \tag{3.1}$$

The central objective of this chapter is to bring new ideas to implement a theoretical framework to describe the GeSn luminescence properties using the multi-band ***k.p*** formalism. The model presented in this chapter is focused on single bulk material that can also be seen as a top layer or i-layer in a device heterostructure. The hypotheses and approximations used in this framework are outlined and justified in the methodology. The obtained results are discussed in the subsequent chapters.

The computation of the spontaneous emission spectrum requires prior knowledge of the band structure of the semiconductors, the momentum matrix elements, and the quasi-Fermi levels, as seen in equation (3.1). The computations of the integral over the BZ and the Dirac delta function also need to be addressed. Depending on the experimental considerations, we can make some hypotheses and approximations to obtain a simple yet accurate model to explain the experimental observations.

For a single bulk direct bandgap semiconductor, the optical matrix element $M_{cv}^2(\vec{\boldsymbol{k}})$ is usually considered isotropic and independent of the wave vector $\vec{\boldsymbol{k}}$ [88]. In that case, we have

$$M_{cv}^2(\vec{\boldsymbol{k}}) = M_b^2 = \frac{P^2}{3} \tag{3.2}$$

, where P is the Kane parameter.

3.1 Spontaneous emission spectrum and the single-band effective mass approximation

The single-band effective mass approximation (SBEMA) is used by various research groups in the literature for the computation of materials band-structure close to the center of the BZ (at $\vec{\boldsymbol{k}} = \vec{\boldsymbol{0}}$) [90–94]. In the situation where each band is considered separately without the influence of the others, the effective mass approximation is used to obtain isotropic and parabolic dispersion relations [88]. In that case, each band is characterized by its extremal

energy value and its effective mass, as presented in equations (3.3).

$$\begin{aligned}
\epsilon_c^{\eta}(\vec{\boldsymbol{k}}) &= E_c^{\eta} + \frac{\hbar^2\left|\vec{\boldsymbol{k}}\right|^2}{2m_c^*}, \\
\epsilon_{hh}^{\sigma}(\vec{\boldsymbol{k}}) &= E_{hh}^{\sigma} - \frac{\hbar^2\left|\vec{\boldsymbol{k}}\right|^2}{2m_{hh}^*}, \\
\epsilon_{lh}^{\sigma}(\vec{\boldsymbol{k}}) &= E_{lh}^{\sigma} - \frac{\hbar^2\left|\vec{\boldsymbol{k}}\right|^2}{2m_{lh}^*}, \\
\epsilon_{so}^{\sigma}(\vec{\boldsymbol{k}}) &= E_{so}^{\sigma} - \frac{\hbar^2\left|\vec{\boldsymbol{k}}\right|^2}{2m_{so}^*}
\end{aligned} \tag{3.3}$$

With the energy conservation imposed by the Dirac delta function in equation (3.1), the energy of the emitted photon $\hbar\omega$ is given by

$$\hbar\omega = E_c^{\eta} - E_v^{\sigma} + \frac{\hbar}{2}\left(\frac{\left|\vec{\boldsymbol{k}}_c\right|^2}{m_c^*} + \frac{\left|\vec{\boldsymbol{k}}_v\right|^2}{m_v^*}\right) \tag{3.4}$$

If we assume the bands to be the same for the different spin values (spin $\uparrow$ and spin $\downarrow$) and consider only the $\vec{\boldsymbol{k}}$-conserving transitions, equation (3.4) becomes

$$\hbar\omega = E_c - E_v + \frac{\hbar\left|\vec{\boldsymbol{k}}\right|^2}{2}\left(\frac{1}{m_c^*} + \frac{1}{m_v^*}\right) = E_{c,v} + \frac{\hbar\left|\vec{\boldsymbol{k}}\right|^2}{2m_{c,v}} \tag{3.5}$$

The parabolic dispersion relations, combined with equation (3.2), have the merit of simplifying the computation of the spontaneous emission spectrum defined in equation (3.1). They lead, for example, to equation (3.6) which is a relatively simple formula for this quantity (see appendix A for the derivation).

$$r^{spon}(\hbar\omega) = \left(\frac{n_r e^2 \hbar\omega M_b^2}{\pi c^3 \varepsilon_0 \hbar^4}\right) \sum_v \rho_{JDOS}\left(\hbar\omega - E_{c,v}\right) f\left(\epsilon_c(\hbar\omega), \mu_e\right)\left[1 - f\left(\epsilon_v(\hbar\omega), \mu_h\right)\right] \tag{3.6}$$

$\rho_{JDOS}(E)$ is better known as the joint density of states (JDOS) and is proportional to $\sqrt{E}$. For a non-degenerately doped semiconductor exposed to an external excitation so that a sufficiently weak injection takes place, we expect the quasi-Fermi levels to lie within the bandgap and away from the different band edges by several $k_B T$. In that case, the Fermi distribution can be approximated [95] by the Boltzmann distribution $f_B(\varepsilon, \mu) = \exp\left(-\frac{\varepsilon-\mu}{k_B T}\right)$

(see figure 3.1), and equation (3.6) becomes

$$r^{spon}(\hbar\omega) \approx \sum_v D_v \left(\hbar\omega - E_{c,v}\right)^{1/2} \exp\left(-\frac{\hbar\omega - E_{c,v}}{k_B T}\right), \quad \hbar\omega \geq E_{c,v} \tag{3.7}$$

where

$$D_v = \frac{\left(2m_{c,v}\right)^{3/2}}{2\pi^2\hbar^3}\left(\frac{n_r e^2 \hbar\omega M_b^2}{\pi c^3 \varepsilon_0 \hbar^4}\right) \exp\left(\frac{\mu_e - \mu_h - E_{c,v}}{k_B T}\right). \tag{3.8}$$

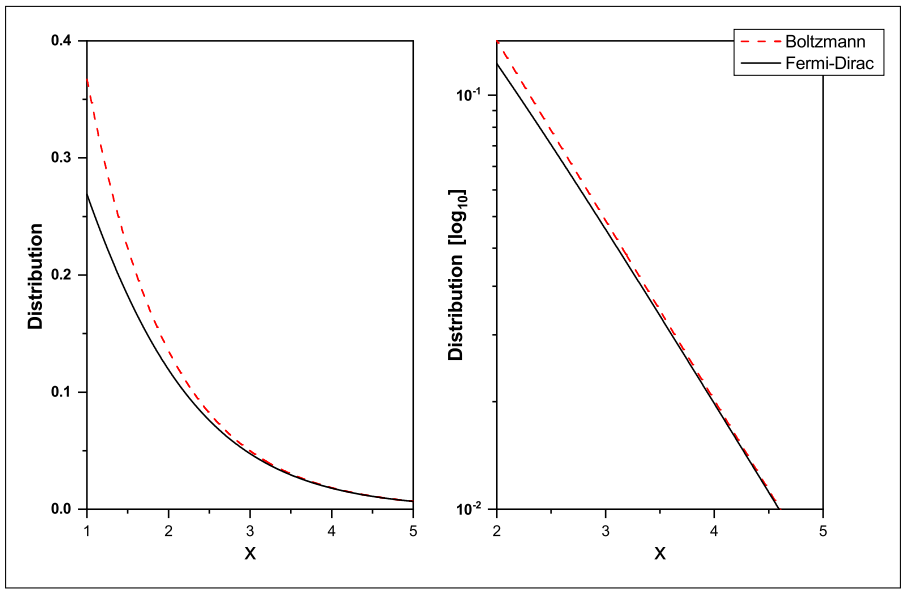

Figure 3.1 Comparison of the Fermi-Dirac and Boltzmann distribution. (a) Linear scale (b) log scale. x is either $\frac{E-\mu_e}{k_B T}$ for the electrons or $\frac{\mu_h - E}{k_B T}$ for the holes.

The coefficient $\hbar\omega$ in D_v is usually neglected relative to the exponential and the square root functions inside of equation (3.7) [3, 87]. In that case, the emission peak position is located at $E_{c,v} + k_B T/2$, and the full width at half maximum is around $1.8 k_B T$ for a semiconductor at thermal equilibrium, as presented in figure 3.2.

The exponential dependence of D_v is directly related to the carrier densities inside the material. In fact, for the electrons density n and holes density p, the spontaneous spectrum r^{spon} can be written as (see appendix B for the derivation)

$$r^{spon}(\hbar\omega) \approx \hbar\omega \left[\sum_v \left(\frac{2m_{c,v}}{m_c}\right)^{3/2} \frac{\left(\hbar\omega - E_{c,v}\right)^{1/2}}{K_v(T)} \exp\left(-\frac{\hbar\omega - E_{c,v}}{k_B T}\right)\right] np, \quad \hbar\omega \geq E_{c,v} \tag{3.9}$$

with $K_v(T)$ a coefficient defined by equation (B.6) in appendix B.

Since n, p, $K_v(T)$ and the masses are not dependent on the energy $\hbar\omega$, equation (3.9) can be

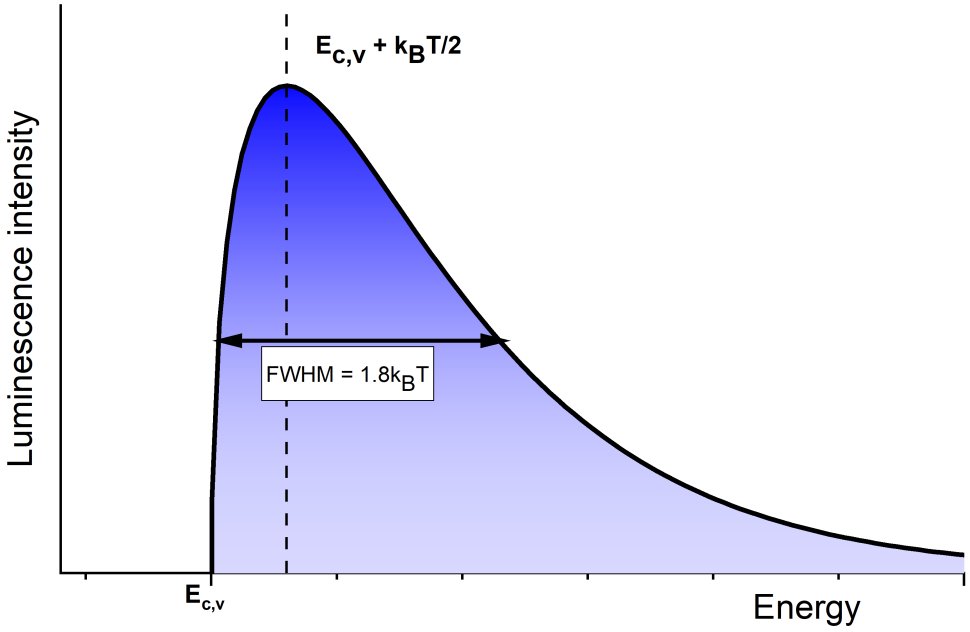

Figure 3.2 Theoretical spontaneous emission spectrum for low injection regime and parabolic band approximation. Adapted from [3]

rewritten as

$$r^{spon}(\hbar\omega) = \sum_{v} A_v(T)\hbar\omega \left(\hbar\omega - E_{c,v}\right)^{1/2} \exp\left(-\frac{\hbar\omega - E_{c,v}}{k_B T}\right), \quad \hbar\omega \geq E_{c,v} \tag{3.10}$$

3.2 Sub-bandgap emission and broadening mechanisms

The theoretical spontaneous emission spectrum developed previously is not sufficient for an accurate description of the PL spectrum. Indeed, there is a sub-bandgap emission below $E_{c,v}$ which is not highlighted in equation (3.7). This emission results from carrier disorders and broadening mechanisms in the materials [96–98]. To account for that, the theoretical spectrum r^{spon}_{ideal} from equation (3.10) is convoluted with a broadening function $\mathcal{B}$ resulting in equation (3.11).

$$r^{spon}(\hbar\omega) = \int_{-\infty}^{+\infty} r^{spon}_{ideal}(\epsilon) \times \mathcal{B}(\hbar\omega - \epsilon)\mathrm{d}\epsilon \tag{3.11}$$

The broadening function $\mathcal{B}$ is usually chosen as a Gaussian or a Lorentzian to account for the inhomogeneous and homogeneous broadening mechanisms. The Lorentzian function was reported to sometimes overestimate the effects of the homogeneous broadening due to its slowly decaying tails. When this is the case, the hyperbolic secant function is used as a

replacement [99]. In addition to these functions, Katahara et al. [100] suggested a new set of functions given by

$$\mathcal{B}(\epsilon) = \frac{1}{2\gamma\Gamma\left(1+\frac{1}{\theta}\right)} \exp\left(-\left|\frac{\epsilon-\epsilon_1}{\gamma}\right|^{\theta}\right) \tag{3.12}$$

where Γ is the Gamma function, γ is the width of the broadening function and ϵ_1 is the characteristic energy of emission. The exponent θ may vary between 0.5 and 2.

The relatively simple equation obtained when combining equations (3.10) and (3.11) can be very useful. Indeed, it is widely used in the literature [5, 101, 102] to fit the temperature-dependent PL spectrum in order to extract the bandgap $E_g(T)$ $(= \min\left[E_{c,hh}(T), E_{c,lh}(T)\right])$. In that case, $A_v(T)$ plays the role of a scaling factor which also varies with the temperature. The accuracy of this fit process relies on the accuracy of the non-degenerate semiconductor condition and the parabolic band approximation in addition to the fulfillment of the low-injection regime.

The SBEMA leads to a set of relatively easy analytical formulas for the computation of the spontaneous recombination spectrum, as we can see with the model developed above. For a non-degenerately doped semiconductor in weak-injection conditions, equation (3.7) is the appropriate formula to use since most carriers are located almost at $\vec{\boldsymbol{k}} = \vec{\mathbf{0}}$. However, a different picture is expected when increasing values of the excitation power or even the doping concentration. Indeed, the increasing densities of carriers inside the material would shift the quasi-Fermi levels towards the band edges. In that case, the semiconductor would not be non-degenerate anymore and, the calculations are not as simple as presented before. For a biaxially strained semiconductor, the $\vec{\boldsymbol{k}}$ direction degeneracies are expected to be broken. In this situation, the band dispersions would be more and more anisotropic. The isotropy argument put forward by the SBEMA is therefore increasingly challenged and, a more accurate description of the band structure is required. With all these limitations, some questions arise. For example, how can we take into account the anisotropy of the band structures in strained materials? What can we do for degenerately-doped semiconductors? How do we deal with excitation regimes other than the weak injection? Can we develop a framework to go beyond the limitations of the SBEMA/JDOS model and extract more parameters in addition to the semiconductor bandgap? We will address most of these questions in section 3.3 and chapter 5, with the multi-band $\boldsymbol{k.p}$ formalism.

3.3 Spontaneous emission spectrum and the multi-band *k.p* formalism

The computation of the spontaneous emission spectrum, using the multi-band ***k.p*** formalism, follows the methodology summarized by the chart in figure 3.3. As mentioned before, the

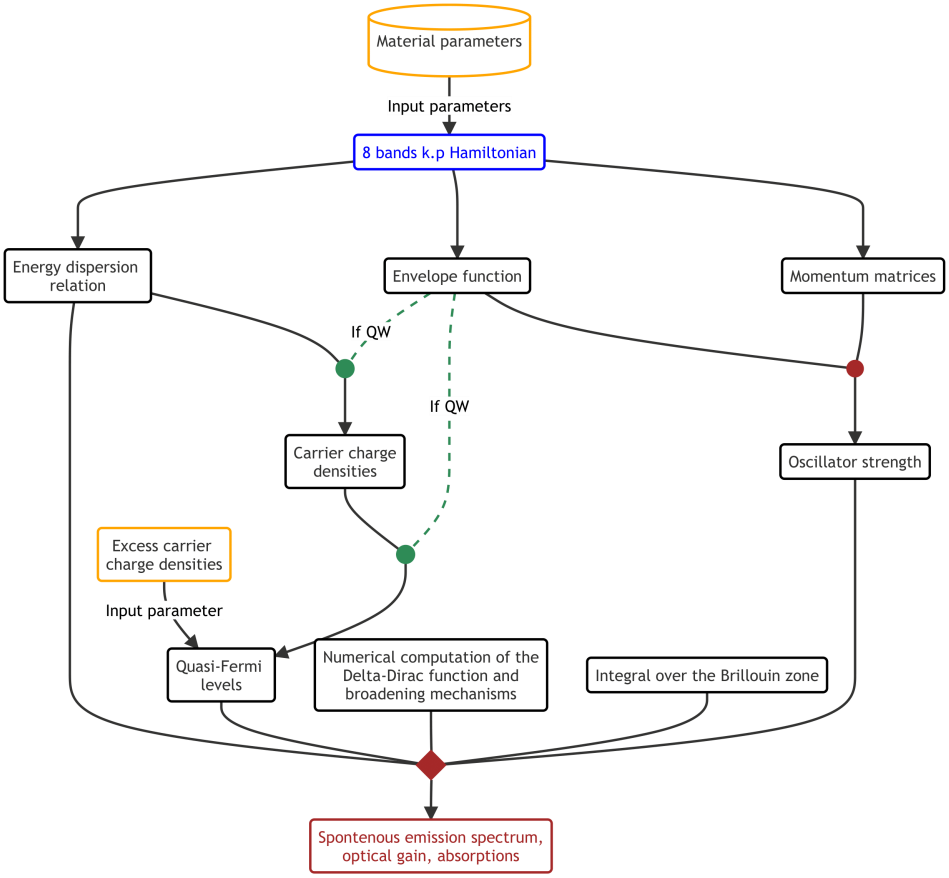

Figure 3.3 Different steps for the computation of the recombination rate and the optical gain

SBEMA is widely used for computing the material band structures with each band taken separately. However, when their interactions (or coupling) are explicitly taken into account, a very different picture that requires much more effort is obtained. Most of the methods used in that case rely on numerical simulations. We have, for example, the tight binding, the pseudo-potential, and the Green's function formalism, which have been discussed in detail in [103,104]. These methods can be accurate to describe the band-structure of a semiconductor material but, for direct band-gap semiconductors with the optical transitions relatively close to the Γ point, the multi-band ***k.p*** method [105] introduced by Bardeen [106] and Seitz [107] is more suitable.

3.3.1 Multi-band kp model and electronic band structure of (Si)GeSn alloys

In our team, we developed the six and eight bands ***k.p*** models for biaxially strained materials based on the formalism highlighted by Eißfeller [108], Bahder [109], and Winkler [110]

The multi-band ***k.p*** formalism together with the envelope function approximation (EFA) can be seen as a method used to solve the Schrödinger equation given by equation (3.13) in which $\mathbf{V}$ is the mean-field periodic potential including all the different interactions. The eigenfunctions $\psi_n(\vec{\mathbf{r}})$ are Bloch's functions defined in equation (3.14) with the periodic functions $u_{n,\hat{\boldsymbol{k}}}(\vec{\mathbf{r}})$.

$$\hat{\mathcal{H}}\psi_n(\vec{\mathbf{r}}) = \left[\frac{\mathbf{p}^2}{2m_0} + \mathbf{V}(\vec{\mathbf{r}})\right]\psi_n(\vec{\mathbf{r}}) = E_n\psi_n(\vec{\mathbf{r}}) \tag{3.13}$$

$$\psi_n(\vec{\mathbf{r}}) = \exp\left(i\vec{\boldsymbol{k}}\cdot\vec{\boldsymbol{r}}\right)u_{n,\vec{\boldsymbol{k}}}(\vec{\mathbf{r}}) \tag{3.14}$$

Using equation (3.14), the equation (3.13) becomes

$$\hat{\mathcal{H}}(\vec{\boldsymbol{k}})u_{n,\vec{\boldsymbol{k}}}(\vec{\mathbf{r}}) = \left[\frac{\mathbf{p}^2}{2m_0} + \mathbf{V}(\vec{\mathbf{r}}) + \frac{\hbar}{m_0}\vec{\mathbf{k}}\cdot\vec{\mathbf{p}} + \frac{\hbar^2\mathbf{k}^2}{2m_0}\right]u_{n,\vec{\boldsymbol{k}}}(\vec{\mathbf{r}}) = E_n(\vec{\mathbf{k}})u_{n,\vec{\boldsymbol{k}}}(\vec{\mathbf{r}}) \tag{3.15}$$

The ***k.p*** formalism relies on the fact that the carriers in the semiconductors would mainly be located in regions relatively close to the extrema of the conduction and valence bands to solve this equation and extract the functions $u_{n,\vec{\boldsymbol{k}}}$ as well as the energies $E_n(\vec{\mathbf{k}})$. In that situation, the description of the band structure in the remaining regions should be neglected. With the ***k.p*** method, the dispersion relation $E_n(\vec{\mathbf{k}})$ is expanded around a particular point $\vec{\mathbf{k}}_0$, where $E_n(\vec{\mathbf{k}}_0)$ and $u_{n,\vec{\boldsymbol{k}}_0}(\vec{\mathbf{r}})$ are assumed to be known for each value of n.

Since $u_{n,\vec{\boldsymbol{k}}_0}(\vec{\mathbf{r}})$ and $E_n(\vec{\mathbf{k}}_0)$ are solutions of equation (3.15) at $\vec{\mathbf{k}}_0$, the functions $u_{n,\vec{\boldsymbol{k}}_0}(\vec{\mathbf{r}})$ form an orthonormal basis in which the unknown functions $u_{n,\vec{\boldsymbol{k}}}$ can be expanded following the relation

$$u_{n,\vec{\boldsymbol{k}}}(\vec{\mathbf{r}}) = \sum_m \phi_{n,m}(\vec{\boldsymbol{k}})u_{m,\vec{\boldsymbol{k}}_0}(\vec{\mathbf{r}}) \tag{3.16}$$

By inserting this equation into equation (3.15), multiplying both sides of the equation by $u^*_{l,\vec{\boldsymbol{k}}_0}(\vec{\mathbf{r}})$, and integrating over the unit cell, we obtain

$$\sum_m \hat{\mathcal{H}}_{l,m}(\vec{\boldsymbol{k}})\phi_{n,m}(\vec{\boldsymbol{k}}) = E_n(\vec{\boldsymbol{k}})\phi_{n,l}(\vec{\boldsymbol{k}}) \tag{3.17}$$

with

$$\hat{\mathcal{H}}_{l,m}(\vec{\boldsymbol{k}}) = \left[E_m(\vec{\boldsymbol{k}}_0) + \frac{\hbar^2}{2m_0}\left(\vec{\boldsymbol{k}}^2 - \vec{\boldsymbol{k}}_0^2\right)\right]\delta_{l,m} + \frac{\hbar}{m_0}\left(\vec{\boldsymbol{k}} - \vec{\boldsymbol{k}}_0\right)\cdot\vec{\mathbf{p}}_{l,m} \tag{3.18}$$

and

$$\vec{\mathbf{p}}_{l,m} = \int\limits_{\text{unit cell}} \mathrm{d}^3\vec{\mathbf{r}}\, u^*_{l,\vec{\boldsymbol{k}}_0}(\vec{\mathbf{r}})\mathbf{p}u_{m,\vec{\boldsymbol{k}}_0}(\vec{\mathbf{r}}) \tag{3.19}$$

In equation (3.17), the summation is done over an infinite number of bands m. In that case, the Hamiltonian $\mathcal{H}$ should have an infinite-dimensional matrix. However, only a few bands are usually physically relevant to describe the carrier dynamics in the conduction and the valence bands. The number of bands is mainly reduced by using Löwdin's perturbation theory which allows us to restrict the study to the N relevant bands while considering the impact of the other bands as small perturbations with the off-diagonal terms $\frac{\hbar}{m_0}\left(\vec{\boldsymbol{k}} - \vec{\boldsymbol{k}}_0\right) \cdot \vec{\mathbf{p}}_{l,m}$ [111]. The resulting Hamiltonian is given by equation (3.20), where l and m are lesser than N and B is the set of remote bands.

$$\hat{\mathcal{H}}'_{l,m}(\vec{\boldsymbol{k}}) = \hat{\mathcal{H}}_{l,m}(\vec{\boldsymbol{k}}) + \sum_{j\in B} \frac{\hat{\mathcal{H}}_{l,j}(\vec{\boldsymbol{k}})\hat{\mathcal{H}}_{j,m}(\vec{\boldsymbol{k}})}{E_l(\vec{\boldsymbol{k}}_0) - E_j(\vec{\boldsymbol{k}}_0)} \tag{3.20}$$

The spin-orbit interaction can also be taken into account by adding $\hat{\mathcal{H}}_{SO}$ (equation (3.21)) in equation (3.13)

$$\hat{\mathcal{H}}_{SO} = \frac{\hbar}{4m_0^2c^2}(\boldsymbol{\nabla}V \times \mathbf{p}) \cdot \sigma \tag{3.21}$$

With this new term, $\hat{\mathcal{H}}_{l,m}$ from equation (3.17) becomes

$$\hat{\mathcal{H}}_{l,m}(\vec{\boldsymbol{k}}) = \left[E_m(\vec{\boldsymbol{k}}_0) + \frac{\hbar^2}{2m_0}\left(\vec{\boldsymbol{k}}^2 - \vec{\boldsymbol{k}}_0^2\right)\right]\delta_{l,m} + \frac{\hbar}{m_0}\left(\vec{\boldsymbol{k}} - \vec{\boldsymbol{k}}_0\right) \cdot \boldsymbol{\pi}_{l,m} \tag{3.22}$$

with

$$\boldsymbol{\pi}_{l,m} = \int\limits_{\text{unit cell}} \mathrm{d}^3\vec{\mathbf{r}}\, u^*_{l,\vec{\boldsymbol{k}}_0}(\vec{\mathbf{r}})\left[\mathbf{p} + \frac{\hbar}{4m_0c^2}(\boldsymbol{\nabla}V \times \mathbf{p})\right]u_{m,\vec{\boldsymbol{k}}_0}(\vec{\mathbf{r}}) \tag{3.23}$$

A semiconductor layer pseudomorphically grown on a lattice-mismatched substrate is subject to a uniform biaxial bi-isotropic strain in its plane. The in-plane lattice strain $\varepsilon_{\|}$ is then given by

$$\boldsymbol{\varepsilon}_{\|} = \frac{a_S - a_L}{a_L} \tag{3.24}$$

with a_S and a_L the bulk lattice constants of the substrate and the semiconductor layer, respectively. In our models, the lattice strain is accounted for through the Pikus-Bir Hamiltonian [112]. Within this formalism, the strain impact is incorporated into the band structure

as a perturbative term

$$\mathcal{H}_{\text{strain}} = \left(\sum_{\alpha,\beta \in \{x,y,z\}} \mathcal{D}_{ij}^{\alpha\beta} \boldsymbol{\varepsilon}_{\alpha\beta} \right)_{ij} \tag{3.25}$$

with $\boldsymbol{\varepsilon}_{\alpha\beta}$ the (α, β) element of the strain tensor $\boldsymbol{\varepsilon}$ and $\mathcal{D}_{ij}^{\alpha\beta}$ a deformation potential. We assume a homogeneous strain which results in $\boldsymbol{\varepsilon}_{\alpha\beta} = \boldsymbol{\varepsilon}_{\beta\alpha}$. In the cartesian basis $\{|S\uparrow\rangle, |S\downarrow\rangle, |X\uparrow\rangle, |Y\uparrow\rangle, |Z\uparrow\rangle, |X\downarrow\rangle, |Y\downarrow\rangle, |Z\downarrow\rangle\}$, the Hamiltonian $\mathcal{H}_{strain}$ is given by [113]

$$\mathcal{H}_{\text{strain}} = \left(\begin{array}{c|cc} \boldsymbol{\mathcal{H}}_{\text{cb}} & 0_{2\times 6} & \\ \hline 0_{6\times 2} & \boldsymbol{\mathcal{H}}_{\text{vb}} & 0_{3\times 3} \\ & 0_{3\times 3} & \boldsymbol{\mathcal{H}}_{\text{vb}} \end{array} \right) \tag{3.26}$$

with

$$\boldsymbol{\mathcal{H}}_{\text{cb}} = \begin{pmatrix} a_c^{\Gamma} \cdot \text{tr}(\boldsymbol{\varepsilon}) & 0 \\ 0 & a_c^{\Gamma} \cdot \text{tr}(\boldsymbol{\varepsilon}) \end{pmatrix}, \tag{3.27}$$

$$\boldsymbol{\mathcal{H}}_{\text{vb}} = \begin{pmatrix} l\boldsymbol{\varepsilon}_{xx} + m\left(\boldsymbol{\varepsilon}_{yy} + \boldsymbol{\varepsilon}_{zz}\right) & n\boldsymbol{\varepsilon}_{xy} & n\boldsymbol{\varepsilon}_{zx} \\ n\boldsymbol{\varepsilon}_{xy} & l\boldsymbol{\varepsilon}_{yy} + m\left(\boldsymbol{\varepsilon}_{xx} + \boldsymbol{\varepsilon}_{zz}\right) & n\boldsymbol{\varepsilon}_{yz} \\ n\boldsymbol{\varepsilon}_{zx} & n\boldsymbol{\varepsilon}_{yz} & l\boldsymbol{\varepsilon}_{zz} + m\left(\boldsymbol{\varepsilon}_{yy} + \boldsymbol{\varepsilon}_{xx}\right) \end{pmatrix} \tag{3.28}$$

The trace of $\boldsymbol{\varepsilon}$ defined by $\text{tr}(\boldsymbol{\varepsilon})$ in the matrices is given by $\boldsymbol{\varepsilon}_{xx} + \boldsymbol{\varepsilon}_{yy} + \boldsymbol{\varepsilon}_{zz}$. The coefficient a_c^{Γ} is the Γ-valley conduction band deformation potential. The quantities l, m, and n are related to the valence bands absolute deformation potential a_v and the shear deformation potentials b and d. They are defined in the equation (3.29)

$$\begin{aligned} a_v &= \frac{l + 2m}{3}, \\ b &= \frac{l - m}{3}, \\ d &= \frac{n}{\sqrt{3}}. \end{aligned} \tag{3.29}$$

The relation between the strain tensor $\boldsymbol{\varepsilon}$ and the in-plane strain $\boldsymbol{\varepsilon}_{\parallel}$ is dependent on the substrate crystallographic orientation. Indeed, Hinckley et al. developed the underlying theory for an arbitrary crystallographic orientation [113]. For the case of a (001)-oriented substrate,

the strain tensor components are given by

$$\begin{aligned} \boldsymbol{\varepsilon}_{xx} &= \boldsymbol{\varepsilon}_{yy} = \boldsymbol{\varepsilon}_{\parallel} \\ \boldsymbol{\varepsilon}_{zz} &= -\frac{2C_{12}}{C_{11}}\boldsymbol{\varepsilon}_{xx} \\ \boldsymbol{\varepsilon}_{xy} &= \boldsymbol{\varepsilon}_{yz} = \boldsymbol{\varepsilon}_{xz} = 0 \end{aligned} \tag{3.30}$$

with C_{11} and C_{12} the elastic stiffness constants.

Like the strain tensor, the $\vec{\boldsymbol{k}}$-dependence of the ***k.p*** Hamiltonian is also subject to the substrate crystallographic orientation since different rotation matrices have to be considered for a direction other than [001]. More information about the underlying theory for these rotation matrices can be found in Eißfeller's thesis [108].

Most of the physical parameters of GeSn alloy are obtained by linear interpolation among those of Si, Ge, and α-Sn, except for the unstrained energy and the Luttinger parameters. Indeed for GeSn, we use the quadratic polynomial interpolations

$$\begin{aligned} E_{g,\mu}^{\mathrm{Ge}_{1-y}\mathrm{Sn}_y}(T) &= (1-y)E_{g,\mu}^{\mathrm{Ge}}(T) + yE_{g,\mu}^{\mathrm{Sn}}(T) - y(1-y)b_{\mu} \\ \Delta_{SO}^{\mathrm{Ge}_{1-y}\mathrm{Sn}_y} &= (1-y)E_{SO}^{\mathrm{Ge}} + yE_{SO}^{\mathrm{Sn}} - y(1-y)b_{SO} \end{aligned} \tag{3.31}$$

where b_{μ}, b_{SO} are the bowing parameters for GeSn, and μ refers to the different conduction valleys; i.e., Γ, L and X. The Luttinger parameters are obtained after fitting the results from the work of Kain Lu et al. [2] and we have

$$\gamma_i^{\mathrm{Ge}_{1-y}\mathrm{Sn}_y} = \left(1 - \frac{y}{0.2}\right)\gamma_i^{\mathrm{Ge}} + 29.2108\left(\frac{y}{0.2}\right) - 20.3391\left(\frac{y}{0.2}\right)\left(1 - \frac{y}{0.2}\right) \tag{3.32}$$

where γ_i refers to the different Luttinger parameters; i.e, γ_1, γ_2, and,γ_3. The material physical parameters used for our models are listed in Table 3.1.

Table 3.1 – Physical parameters of Ge and α-Sn

Parameters	Ge	Sn	$Ge_{1-y}Sn_y$ bowing
Lattice constants(nm)			
a	0.565789 (at 298 K)[b*]	0.64892 (at 293 K)[d#]	-0.0083[f]
Effective masses(m_0)			
m_c	0.0383[a]	-0.058[g]	
m_t^L	0.0807[c]	0.075[c]	
m_l^L	1.57[c]	1.478[c]	

Continued on next page

Table 3.1 – Physical parameters of Ge and α-Sn (*Continued*)

Parameters	Ge	Sn	$Ge_{1-y}Sn_y$ bowing
Luttinger parameters			
γ_1	13.3667[a]	-25.19[e]	Equation (3.32)
γ_2	4.2333[a]	-15.10[e]	Equation (3.32)
γ_3	5.6833[a]	-13.53[e]	Equation (3.32)
κ	3.41[a]	-11.84[g]	
Average valence band energy			
$E_{V,avg}$ (meV)	0[**]	690[c]	
Bandgaps**(meV)**			
E_g^Γ	898.1 (at 1.5K)	-390 (at 0K)[e]	2.46×10^3[e]
E_g^L	785.0 (at 0 K)[a]	100[f]	1.23×10^3[e]
E_g^X	931.0[a]	735.2[f]	
Δ_{SO}	289[a]	600[f]	100[f]
Elastic constants**(GPa)**			
C_{11}	128.53[a]	69.00[c]	
C_{12}	48.28[a]	29.30[c]	
C_{44}	66.80[a]	36.20[c]	
Permittivities			
ε_r	16[a]	24[e]	
Optical energy			
E_p (eV)	26.3[a]	24[c]	
Deformation potentials			
a_c^Γ(eV)	-10.41[a]	-6.00[c]	
a_c^L(eV)	-1.54[a]	-2.14[c]	
a_c^X(eV)	2.55[a]	0[***]	
a_v(eV)	1.24[a]	1.58[c]	
b(eV)	-2.86[a]	-2.7[c]	
d(eV)	-5.28[a]	-4.1[d]	
Ξ_u^Γ	0[a]	0[a]	
Ξ_u^L	16.3[a]	0[***]	
Ξ_u^X	9.42[a]	0[***]	
Varshni parameters			
α_Γ (meV/K)	0.6842[a]	-0.7940[e]	
β_Γ (K)	398[a]	11[e]	
α_L (meV/K)	0.4561[a]	-	

Continued on next page

Table 3.1 – Physical parameters of Ge and α-Sn (*Continued*)

Parameters	Ge	Sn	$Ge_{1-y}Sn_y$ bowing
β_L (K)	210[a]	-	
α_X (meV/K)	0.4774[a]	-	
β_X (K)	235[a]	-	

[a] Reference [114], [b] Reference [115],[c] Reference [116], [d] Reference [117], [e] Reference [118], [f] Reference [119], [g] Reference [120]
[*] the lattice constant is computed through the analysis of Germanium thermal expansion;
[**] $E_{V,avg}$ of other materials are relative to that of Ge.
[#] $a(T) = 0.64892 + 3.1 \times 10^{-6}(T - 293)$
[***] These parameters are unknown so we consider them as zero.

3.3.2 The momentum matrices

The momentum matrices are representative of the strength of the different transitions that could happen between the carriers after the excitation of the material. In addition to the SBEMA, the computations highlighted in the previous sections rely on the assumption that the momentum matrix element is a constant of the wave vector $\vec{\boldsymbol{k}}$. Instead of relying on this assumption, we compute these matrices through the ***k.p*** Hamiltonian as discussed by Szmulowicz [121].

If we define by $|\Phi\rangle$ and $|\Psi\rangle$ the initial and final states, within the EFA, the strength of the transition is defined by [121]:

$$\left\langle \Phi \left| \frac{\hbar}{m_0} \hat{\mathbf{e}}.\vec{\boldsymbol{p}} \right| \Psi \right\rangle = \sum_{\mu\nu} \Phi_\mu^*(\vec{\boldsymbol{k}}, \vec{\boldsymbol{r}}) \left(\hat{\mathbf{e}} \cdot \frac{\partial \mathcal{H}_{\mu\nu}(\vec{\boldsymbol{k}}, \vec{\boldsymbol{r}})}{\partial \vec{\boldsymbol{k}}} \right) \Psi_\nu(\vec{\boldsymbol{k}}, \vec{\boldsymbol{r}}) \tag{3.33}$$

with

- Φ_μ and Ψ_ν the coefficients of the envelope function vector related to the states $|\Phi\rangle$ and $|\Psi\rangle$ respectively,
- For a single bulk material, Φ_μ and Ψ_ν are only functions of the wave vector $\vec{\boldsymbol{k}}$,
- $\hat{\mathbf{e}}$ gives the polarization of the incident light,
- $\frac{\partial \mathcal{H}_{\mu\nu}(\vec{\boldsymbol{k}}, \vec{\boldsymbol{r}})}{\partial \vec{\boldsymbol{k}}}$ is the derivative of the ***k.p*** Hamiltonian with respect to the wave vector $\vec{\boldsymbol{k}}$.

$$\hat{\mathbf{e}} \cdot \frac{\partial \mathcal{H}_{\mu\nu}}{\partial \vec{\boldsymbol{k}}} = \sum_{l \in (x,y,z)} \varepsilon_l \left(\frac{\partial \mathcal{H}_{\mu\nu}}{\partial k_l} \right) = \sum_{l \in (x,y,z)} \varepsilon_l M_l^{\mu\nu} \tag{3.34}$$

To simplify the expressions of the different momentum matrix elements, we introduce several notations. Among them, we have g and g_0 defined as the conduction-band effective g-factor and the electron-spin g-factor, respectively. We denote by δ a Boolean parameter set to 1

to account for these g-factors explicitly and 0 otherwise. The coefficient P indicates the conduction band-valence band coupling parameter, also known as the Kane parameter. This parameter is used to characterize the coupling between the lowest conduction band and the highest valence band in the eight bands $\boldsymbol{k.p}$ formalism [122]. Its impact on the conduction band Hamiltonian is highlighted by the parameter $A_c = \frac{\hbar^2}{2m_0}S$ with S, a dimensionless parameter defined by [122]

$$S = \frac{m_0}{m_e^*} - \frac{2m_0}{\hbar^2}\left(\frac{E_g + \frac{2}{3}\Delta_{so}}{E_g(E_g + \Delta_{so})}\right)P^2. \tag{3.35}$$

In this equation above, m_e^* is the experimentally determined conduction band effective mass at the Γ point. The parameter E_g is the unstrained bandgap energy between the lowest conduction band edge and the highest valence band edge energy. We denote by L', M', N'_+, N'_- the modified Dresselhaus-Kip-Kittel (DKK) parameters for the eight bands $\boldsymbol{k.p}$ model. We also consider the notations

$$\begin{aligned}
[a,b] &= a \cdot b - b^* \cdot a \\
[a,b]_+ &= a \cdot b + b^* \cdot a, \\
f(a) &= \frac{\hbar^2\delta}{2m_0}[g - g_0, k_a], \\
S_\pm(a,b) &= -if(b) \pm f(a), \\
A_\pm(a,b) &= [A, k_a]_+ \pm if(b), \\
N_1(a) &= k_a^* \cdot N'_- + N'_+ \cdot k_a, \\
N_2(a) &= k_a^* \cdot N'_+ + N'_- \cdot k_a
\end{aligned}$$

with "$\cdot$" here a non-commutative product, and b^* the complex conjugated of b. The non-commutative product is considered to take into account quantum wells, quantum wires and quantum dots in addition to the case of bulk materials.

For a (001) substrate, in the Cartesian basis presented in the previous section, we have the matrices

$$M_x = \begin{pmatrix} A_+(x,y) & -f(z) & P & 0 & 0 & 0 & 0 & 0 \\ f(z) & A_-(x,y) & 0 & 0 & 0 & P & 0 & 0 \\ P & 0 & [L',k_x]_+ & N_1(y) & N_1(z) & 0 & 0 & 0 \\ 0 & 0 & N_2(y) & [M',k_x]_+ & 0 & 0 & 0 & 0 \\ 0 & 0 & N_2(z) & 0 & [M',k_x]_+ & 0 & 0 & 0 \\ 0 & P & 0 & 0 & 0 & [L',k_x]_+ & N_1(y) & N_1(z) \\ 0 & 0 & 0 & 0 & 0 & N_2(y) & [M',k_x]_+ & 0 \\ 0 & 0 & 0 & 0 & 0 & N_2(z) & 0 & [M',k_x]_+ \end{pmatrix}$$

$$M_y = \begin{pmatrix} A_-(y,x) & if(z) & 0 & P & 0 & 0 & 0 & 0 \\ if(z) & A_+(y,x) & 0 & 0 & 0 & 0 & P & 0 \\ 0 & 0 & [M',k_y]_+ & N_2(x) & 0 & 0 & 0 & 0 \\ P & 0 & N_1(x) & [L',k_y]_+ & N_1(z) & 0 & 0 & 0 \\ 0 & 0 & 0 & N_2(z) & [M',k_y]_+ & 0 & 0 & 0 \\ 0 & 0 & 0 & 0 & 0 & [M',k_y]_+ & N_2(x) & 0 \\ 0 & P & 0 & 0 & 0 & N_1(x) & [L',k_y]_+ & N_1(z) \\ 0 & 0 & 0 & 0 & 0 & 0 & N_2(z) & [M',k_y]_+ \end{pmatrix}$$

$$M_z = \begin{pmatrix} [A,k_z]_+ & S_+(x,y) & 0 & 0 & P & 0 & 0 & 0 \\ S_-(x,y) & [A,k_z]_+ & 0 & 0 & 0 & 0 & 0 & P \\ 0 & 0 & [M',k_z]_+ & 0 & N_2(x) & 0 & 0 & 0 \\ 0 & 0 & 0 & [M',k_z]_+ & N_2(y) & 0 & 0 & 0 \\ P & 0 & N_1(x) & N_1(y) & [L',k_z]_+ & 0 & 0 & 0 \\ 0 & 0 & 0 & 0 & 0 & [M',k_z]_+ & 0 & N_2(x) \\ 0 & 0 & 0 & 0 & 0 & 0 & [M',k_z]_+ & N_2(y) \\ 0 & P & 0 & 0 & 0 & N_1(x) & N_1(y) & [L',k_z]_+ \end{pmatrix}$$

For the case of bulk material grown on a (001) oriented substrate, $\cdot$ becomes a regular product and (k_x, k_y, k_z) a real vector. In the angular momentum basis $\{|S\uparrow\rangle, |S\downarrow\rangle, |HH\uparrow\rangle, |LH\uparrow\rangle, |LH\downarrow\rangle, |HH\downarrow\rangle, |SO\uparrow\rangle, |SO\downarrow\rangle\}$ [108] which is more relevant

for our computations, the matrices above become :

$$M_x = \begin{pmatrix}
2A_ck_x & 0 & -\frac{P}{\sqrt{2}} & 0 & \frac{P}{\sqrt{6}} & 0 & 0 & -\frac{P}{\sqrt{3}} \\
0 & 2A_ck_x & 0 & -\frac{P}{\sqrt{6}} & 0 & \frac{P}{\sqrt{2}} & -\frac{P}{\sqrt{3}} & 0 \\
-\frac{P}{\sqrt{2}} & 0 & -\frac{\hbar^2 k_x \Gamma_+}{m_0} & \frac{\hbar^2\sqrt{3}\gamma_3' k_z}{m_0} & \frac{\hbar^2\sqrt{3}\eta_-(x,y)}{m_0} & 0 & -\frac{\hbar^2\sqrt{6}\gamma_3' k_z}{2m_0} & -\frac{\hbar^2\sqrt{6}\eta_-(x,y)}{m_0} \\
0 & -\frac{P}{\sqrt{6}} & \frac{\hbar^2\sqrt{3}\gamma_3' k_z}{m_0} & \frac{\hbar^2 k_x \Gamma_-}{m_0} & 0 & \frac{\hbar^2\sqrt{3}\eta_-(x,y)}{m_0} & -\frac{\hbar^2\sqrt{2}\gamma_2' k_x}{m_0} & \frac{3\hbar^2\sqrt{2}\gamma_3' k_z}{2m_0} \\
\frac{P}{\sqrt{6}} & 0 & \frac{\hbar^2\sqrt{3}\eta_+(x,y)}{m_0} & 0 & \frac{\hbar^2 k_x \Gamma_-}{m_0} & -\frac{\hbar^2\sqrt{3}\gamma_3' k_z}{m_0} & \frac{3\hbar^2\sqrt{2}\gamma_3' k_z}{2m_0} & \frac{\hbar^2\sqrt{2}\gamma_2' k_x}{m_0} \\
0 & \frac{P}{\sqrt{2}} & 0 & \frac{\hbar^2\sqrt{3}\eta_+(x,y)}{m_0} & -\frac{\hbar^2\sqrt{3}\gamma_3' k_z}{2m_0} & -\frac{\hbar^2 k_x \Gamma_+}{m_0} & \frac{\hbar^2\sqrt{6}\eta_+(x,y)}{m_0} & -\frac{\hbar^2\sqrt{6}\gamma_3' k_z}{2m_0} \\
0 & -\frac{P}{\sqrt{3}} & -\frac{\hbar^2\sqrt{6}\gamma_3' k_z}{2m_0} & -\frac{\hbar^2\sqrt{2}\gamma_2' k_x}{m_0} & \frac{3\hbar^2\sqrt{2}\gamma_3' k_z}{2m_0} & \frac{\hbar^2\sqrt{6}\eta_-(x,y)}{m_0} & -\frac{\hbar^2\gamma_1' k_x}{m_0} & 0 \\
-\frac{P}{\sqrt{3}} & 0 & -\frac{\hbar^2\sqrt{6}\eta_+(x,y)}{m_0} & \frac{3\hbar^2\sqrt{2}\gamma_3' k_z}{2m_0} & \frac{\hbar^2\sqrt{2}\gamma_2' k_x}{m_0} & -\frac{\hbar^2\sqrt{6}\gamma_3' k_z}{2m_0} & 0 & -\frac{\hbar^2\gamma_1' k_x}{m_0}
\end{pmatrix}$$

$$M_y = \begin{pmatrix}
2A_ck_y & 0 & -\frac{iP}{\sqrt{2}} & 0 & -\frac{iP}{\sqrt{6}} & 0 & 0 & \frac{iP}{\sqrt{3}} \\
0 & 2A_ck_y & 0 & -\frac{iP}{\sqrt{6}} & 0 & -\frac{iP}{\sqrt{2}} & -\frac{iP}{\sqrt{3}} & 0 \\
\frac{iP}{\sqrt{2}} & 0 & -\frac{\hbar^2 k_y \Gamma_+}{m_0} & -\frac{i\hbar^2\sqrt{3}\gamma_3' k_z}{m_0} & -\frac{\hbar^2\sqrt{3}\eta_+(y,x)}{m_0} & 0 & \frac{i\hbar^2\sqrt{6}\gamma_3' k_z}{2m_0} & \frac{\hbar^2\sqrt{6}\eta_+(y,x)}{m_0} \\
0 & \frac{iP}{\sqrt{6}} & \frac{i\hbar^2\sqrt{3}\gamma_3' k_z}{m_0} & \frac{\hbar^2 k_y \Gamma_-}{m_0} & 0 & -\frac{\hbar^2\sqrt{3}\eta_+(y,x)}{m_0} & -\frac{\hbar^2\sqrt{2}\gamma_2' k_y}{m_0} & -\frac{3i\hbar^2\sqrt{2}\gamma_3' k_z}{2m_0} \\
\frac{iP}{\sqrt{6}} & 0 & -\frac{\hbar^2\sqrt{3}\eta_-(y,x)}{m_0} & 0 & \frac{\hbar^2 k_y \Gamma_-}{m_0} & \frac{i\hbar^2\sqrt{3}\gamma_3' k_z}{m_0} & \frac{3i\hbar^2\sqrt{2}\gamma_3' k_z}{2m_0} & \frac{\hbar^2\sqrt{2}\gamma_2' k_y}{m_0} \\
0 & \frac{iP}{\sqrt{2}} & 0 & -\frac{\hbar^2\sqrt{3}\eta_-(y,x)}{m_0} & -\frac{i\hbar^2\sqrt{3}\gamma_3' k_z}{m_0} & -\frac{\hbar^2 k_y \Gamma_+}{m_0} & -\frac{\hbar^2\sqrt{6}\eta_-(y,x)}{m_0} & -\frac{i\hbar^2\sqrt{6}\gamma_3' k_z}{2m_0} \\
0 & \frac{iP}{\sqrt{3}} & -\frac{i\hbar^2\sqrt{6}\gamma_3' k_z}{2m_0} & -\frac{\hbar^2\sqrt{2}\gamma_2' k_y}{m_0} & -\frac{3i\hbar^2\sqrt{2}\gamma_3' k_z}{2m_0} & -\frac{\hbar^2\sqrt{6}\eta_+(y,x)}{m_0} & -\frac{\hbar^2\gamma_1' k_y}{m_0} & 0 \\
-\frac{iP}{\sqrt{3}} & 0 & \frac{\hbar^2\sqrt{6}\eta_-(y,x)}{m_0} & \frac{3i\hbar^2\sqrt{2}\gamma_3' k_z}{2m_0} & \frac{\hbar^2\sqrt{2}\gamma_2' k_y}{m_0} & \frac{i\hbar^2\sqrt{6}\gamma_3' k_z}{2m_0} & 0 & -\frac{\hbar^2\gamma_1' k_y}{m_0}
\end{pmatrix}$$

$$M_z = \begin{pmatrix}
2A_c k_z & 0 & 0 & \sqrt{\frac{2}{3}}P & 0 & 0 & -\frac{P}{\sqrt{3}} & 0 \\
0 & 2A_c k_z & 0 & 0 & \sqrt{\frac{2}{3}}P & 0 & 0 & \frac{P}{\sqrt{3}} \\
0 & 0 & -\frac{\hbar^2 k_z(\gamma_1'-2\gamma_2')}{m_0} & \frac{\hbar^2\sqrt{3}\gamma_3' k_-}{m_0} & 0 & 0 & -\frac{\hbar^2\sqrt{6}\gamma_3' k_-}{2m_0} & 0 \\
\sqrt{\frac{2}{3}}P & 0 & \frac{\hbar^2\sqrt{3}\gamma_3' k_+}{m_0} & -\frac{\hbar^2 k_z(\gamma_1'+2\gamma_2')}{m_0} & 0 & 0 & \frac{2\hbar^2\sqrt{2}\gamma_2' k_z}{m_0} & \frac{3\hbar^2\sqrt{2}\gamma_3' k_-}{2m_0} \\
0 & \sqrt{\frac{2}{3}}P & 0 & 0 & -\frac{\hbar^2 k_z(\gamma_1'+2\gamma_2')}{m_0} & -\frac{\hbar^2\sqrt{3}\gamma_3' k_-}{m_0} & \frac{3\hbar^2\sqrt{2}\gamma_3' k_+}{2m_0} & -\frac{2\hbar^2\sqrt{2}\gamma_2' k_z}{m_0} \\
0 & 0 & 0 & 0 & -\frac{\hbar^2\sqrt{3}\gamma_3' k_+}{m_0} & -\frac{\hbar^2 k_z(\gamma_1'-2\gamma_2')}{m_0} & 0 & -\frac{\hbar^2\sqrt{6}\gamma_3' k_+}{2m_0} \\
-\frac{P}{\sqrt{3}} & 0 & -\frac{\hbar^2\sqrt{6}\gamma_3' k_+}{2m_0} & \frac{2\hbar^2\sqrt{2}\gamma_2' k_z}{m_0} & \frac{3\hbar^2\sqrt{2}\gamma_3' k_-}{2m_0} & 0 & -\frac{\hbar^2\gamma_1' k_z}{m_0} & 0 \\
0 & \frac{P}{\sqrt{3}} & 0 & \frac{3\hbar^2\sqrt{2}\gamma_3' k_+}{2m_0} & -\frac{2\hbar^2\sqrt{2}\gamma_2' k_z}{m_0} & -\frac{\hbar^2\sqrt{6}\gamma_3' k_-}{2m_0} & 0 & -\frac{\hbar^2\gamma_1' k_z}{m_0}
\end{pmatrix}$$

with $\gamma_1', \gamma_2', \gamma_3'$ the modified Luttinger parameters. To simplify these matrices expressions, we have introduced the coefficients $\Gamma_\pm = \gamma_2' \pm \gamma_1'$, $k_\pm = k_x \pm ik_y$ and the function $\eta_\pm(a,b) = \gamma_2' k_a \pm i\gamma_3' k_b$.

The list of the prerequisites for the computation of the recombination spectrum is now shortened. Indeed, in addition to the band structure, the momentum matrices are now known. Our only missing parameters are the quasi-Fermi levels. The theory related to these parameters will be highlighted in section 3.3.3 below.

3.3.3 Carriers density and quasi-Fermi levels

For a quasi l-dimensional system, the carrier densities are computed through the multi-band ***k.p*** model. The electron and holes charge densities are given by [123]

$$\begin{aligned}
n(\vec{\boldsymbol{r}}) &= \sum_{i\in \mathrm{CB}} \frac{1}{(2\pi)^{3-l}} \int_{\mathrm{BZ}} d^{3-l}\vec{\boldsymbol{k}}_l \left|\Psi_i(\vec{\boldsymbol{r}}, \vec{\boldsymbol{k}}_l)\right|^2 f\Big(\epsilon_i(\vec{\boldsymbol{k}}_l), \mu_e(\vec{\boldsymbol{r}})\Big), \\
p(\vec{\boldsymbol{r}}) &= \sum_{j\in \mathrm{VB}} \frac{1}{(2\pi)^{3-l}} \int_{\mathrm{BZ}} d^{3-l}\vec{\boldsymbol{k}}_l \left|\Psi_j(\vec{\boldsymbol{r}}, \vec{\boldsymbol{k}}_l)\right|^2 \Big[1 - f\Big(\epsilon_j(\vec{\boldsymbol{k}}_l), \mu_h(\vec{\boldsymbol{r}})\Big)\Big]
\end{aligned} \tag{3.36}$$

Here, the summations are done over the eigenstates of the conduction and valence bands. $\vec{\boldsymbol{k}}_l$ corresponds to the wave vectors restricted to the $(3-l)$-BZ ($\vec{\boldsymbol{k}}_l = (k_1, ...k_{3-l})$). The function f represents the Fermi-Dirac distribution with the position-dependent electron and holes quasi-Fermi levels μ_e and μ_h. The spin degeneracies are explicitly taken into account in this formula. It is the reason why we do not have the prefactor 2 for each charge density. $\Psi(\vec{\boldsymbol{r}}, \vec{\boldsymbol{k}}_l)$ refers to the i^{th} envelope function of the conduction (valence) band linked to the eigenvalue

$E_i(\vec{\boldsymbol{k}}_l)$. $\left|\Psi_i(\vec{\boldsymbol{r}},\vec{\boldsymbol{k}}_l)\right|^2$ represents the probability density for a given subband i. In a N-bands $\boldsymbol{k.p}$ model, it is given by

$$\left|\Psi_i(\vec{\boldsymbol{r}},\vec{\boldsymbol{k}}_l)\right|^2 = \sum_{\mu=1}^{N}\left|\Psi_i^{(\mu)}(\vec{\boldsymbol{r}},\vec{\boldsymbol{k}}_l)\right|^2. \tag{3.37}$$

The position dependence here is presented to account for systems with confinement such as quantum wells (QW)s, quantum wires, and quantum dots. However, for single bulk materials, the $\vec{\boldsymbol{r}}$-dependence from equations (3.36) would be dropped, resulting in the probability density from equation (3.37) being unity.

The computation of the integral over the BZ is a relatively complex task to perform. It generally requires some time-consuming methods in addition to the mathematical complexity. The computation time can be reduced by relying on the symmetry of the crystal or the most symmetrical directions in the BZ. For the charge densities presented above, we could also rely on the convergence of the Fermi-Dirac distribution to restrict our integration domain to a relatively small part of the Brillouin zone.

In the case of the SBEMA, the integral over the BZ($l < 3$) are analytically computed by relying on the simple energy dispersion relation presented in the previous sections. In that case, the charge densities for bulk semiconductors ($l = 0$) are

$$\begin{aligned} n &= g_\nu N_\nu(T)\mathcal{F}_{1/2}\left(\frac{-\epsilon_\nu(\vec{\mathbf{0}})+\mu_e}{k_BT}\right), \\ p &= 2\sum_{i\in\mathrm{VB}} N_i(T)\mathcal{F}_{1/2}\left(\frac{\epsilon_i(\vec{\mathbf{0}})-\mu_h}{k_BT}\right), \end{aligned} \tag{3.38}$$

In the case of the holes carrier densities, the summation is done over the heavy, the light, and split-off holes bands' energy. The factor g_ν represents the spin and valley degeneracies of the different conduction bands represented by ν. For example, $g_\Gamma = 2$, $g_L = 8$, $g_X = 6$. The function $\mathcal{F}_{1/2}$ is the complete Fermi-Dirac integral for an index of 1/2 and is given by

$$\mathcal{F}_{1/2}(y) = \frac{2}{\sqrt{\pi}}\int_0^{+\infty}\frac{\sqrt{x}}{1+\exp(x-y)}\mathrm{d}x. \tag{3.39}$$

$N_i(T)$ is the effective density of states at a temperature T defined by

$$N_i(T) = \left(\frac{m_i^{\mathrm{DOS}}k_BT}{2\pi\hbar^2}\right)^{3/2} \tag{3.40}$$

with m_i^{DOS} the density of state mass of the given band i or a given valley in the case of the

conduction bands.

The L and X valleys are expected to contribute to the charge densities depending on the semiconductor material and the lattice strain. With our eight bands ***k.p*** model, we cannot describe the bands related to these valleys. It, therefore, means that we cannot use the equations (3.36) to compute their charge densities. In that case, the eight bands ***k.p*** model and the SBEMA are simultaneously used to have a complete (or at least a reasonable) description of the charge densities inside the material. For instance, the charge densities in the Γ valley will be described by equations (3.36) and that in the other valleys by equations (3.38).

The method highlighted here to determine the quasi-Fermi levels is most efficient to characterize a bulk material under optical injection of carriers to measure the PL. In thermal equilibrium, the single Fermi level E_f is determined by solving the electroneutrality condition given by

$$n\Big|_{\mu_e=E_f}^{(\Gamma)} + n\Big|_{\mu_e=E_f}^{(L)} + n\Big|_{\mu_e=E_f}^{(X)} + N_A^-\Big|_{\mu_h=E_f} = p\Big|_{\mu_h=E_f} + N_D^+\Big|_{\mu_e=E_f} \tag{3.41}$$

Without a loss of generality, we assume the dopants to be fully ionized. In that case, $N_A^- \approx N_A$ and $N_D^+ \approx N_D$.

When carriers are optically injected inside the material, a non-equilibrium state is reached for the whole system. However, a local equilibrium is considered for both the electrons and the holes. In that case, we have two different Fermi levels, μ_e, and μ_h, for the electrons and holes, respectively. If n_0 and p_0 denote the total electrons and holes charge densities at thermal equilibrium, μ_e and μ_h are determined by solving equations (3.42)

$$\begin{aligned} n_0 + \delta n &= n\Big|_{\mu_e}^{(\Gamma)} + n\Big|_{\mu_e}^{(L)} + n\Big|_{\mu_e}^{(X)} \\ p_0 + \delta p &= p\Big|_{\mu_h} \end{aligned} \tag{3.42}$$

where δn and δp are the excess electrons and holes densities respectively.

Here in our model, the density of traps is assumed to be small compared to the electrons and holes' charge densities. In that case, δn and δp should be equal. Moreover, the conduction band electrons are considered to be shared between the Γ and L valleys. This consideration is only used when the energy band offset between these valleys is close or below the thermal energy k_BT. In this situation, we expect the electrons to transition between those valleys. With equations (3.42), it becomes relatively easy to extract the quasi-Fermi levels if we know how to compute the integrals over the reciprocal space for the ***k.p*** model.

3.3.4 Computation of the integrals over the Brillouin zone

The calculation of the integrals over the BZ for bulk structures relies on various methods presented in the literature. The easiest one is the SBEMA. It guarantees more or less an analytical computation for most of the integrals in the model. Equation (3.38) is an example of the simplicity of this method. Besides, there are several other methods such as the special-points approximation [124, 125], the tetrahedron method and its variants [126–128], and also the special-lines approximation (SLA) [129]. The best techniques in our case should be compatible with our eight bands ***k.p*** formalism while requiring less computation time. With these conditions in mind, we can start by ignoring the tetrahedron methods known to be time-consuming procedures and even not suitable for the eight bands ***k.p*** formalism [128]. As mentioned by Enders, the special-points approximation is appropriate and accurate only when the global features of the band structure rather than the local details are required [129]. Therefore, it cannot be used in our case since we deal with the details relatively close to the Γ point. In our model, all the computations related to the bulk-like structures are done using the SLA technique.

Within the SLA, the three-dimensional BZ integrals are replaced by a sum of one-dimensional integrals over some directions (denoted as "special") of the crystal lattice. These directions could be, for example, the symmetry directions that we use in our ***k.p*** model. If we denote by $\mathcal{L}$ the set of the special directions, equation (3.36) will become

$$n = \frac{1}{2\pi^2} \sum_{\beta \in \mathcal{L}} w_\beta \left(\sum_{i \in \mathrm{CB}} \int_0^{k_{\mathrm{BZ}}} \frac{k_\beta^2 \mathrm{d}k_\beta}{1 + \exp\left[\left(\epsilon_i(k_\beta) - \mu_e \right) / kT \right]} \right) \tag{3.43}$$

with w_β the weight of the special direction β and $k_{\mathrm{BZ}} \approx 0.5$ (units of π/a_0, a_0 being the lattice constant of the material) for the eight bands ***k.p*** model to still be accurate. Depending on the computation, the exact value of the upper limit of integration k_{BZ} could be neglected since we expect the integrand to vanish rapidly while increasing the value of the k_β. Unlike the SBEMA, which leads to parabolic and isotropic-like band structure, this method accounts for the anisotropy and the non-parabolicity of the bands obtained with the ***k.p*** band structure. It is one of the reasons why we expect it to be more efficient than the SBEMA.

For group IV semiconductors, the characteristic directions can be considered as [100], [110], and [111] with all their degeneracies ([100] six-fold, [110] twelve-fold, and [111] eight-fold). In

that case, the set of special directions should be

$$\begin{aligned}\mathcal{L} = \big\{&[100], [001], [010], [\bar{1}00], [0\bar{1}0], [00\bar{1}], [110], [101], [1\bar{1}0],\\ &[10\bar{1}], [\bar{1}10], [\bar{1}01], [\bar{1}\bar{1}0], [\bar{1}0\bar{1}], [011], [0\bar{1}\bar{1}], [0\bar{1}1], [01\bar{1}],\\ &[111], [11\bar{1}], [1\bar{1}1], [1\bar{1}\bar{1}], [\bar{1}\bar{1}\bar{1}], [\bar{1}11], [\bar{1}\bar{1}1], [\bar{1}1\bar{1}]\ \}\end{aligned} \tag{3.44}$$

with $w_\beta = \frac{1}{26}$ for each direction. We expect some of the directions to be equivalent depending on the strain applied to the material. For example, for an unstrained material, $\mathcal{L}$ is reduced to

$$\mathcal{L} = \{[100], [110], [111]\} \tag{3.45}$$

since [100], [110] and, [111] are equivalent to their degeneracies.

The symmetric directions are usually assumed to carry all the relevant sets of information. This assumption is not always accurate since less symmetric lines can also convey relevant details about the material. Therefore, more directions have to be considered in addition to the ones from equation (3.44). We can take this case into account by considering Kane's Y stars [130]. The Y stars are the $\vec{\boldsymbol{k}}$-directions forming equal angles with adjacent symmetry directions. There are forty-eight directions as presented in table 1 and figure 1 of [131]. The set $\mathcal{L}$ from equation (3.44) should have seventy-four elements with these forty-eight new directions taken into account. With the determination of the thermal equilibrium Fermi level E_f and the quasi-Fermi levels, μ_e and μ_h from equations (3.41) and (3.42), the consideration of all these directions should increase the computation time depending on the algorithm used.

3.4 Spontaneous emission intensity and steady-state radiative carrier lifetime

We shall use the symbols $R_{sp}^{\hat{\mathbf{e}}}$ to denote the rate of polarization-dependent spontaneous emission per unit volume ($\mathrm{s}^{-1} \cdot \mathrm{cm}^{-3}$), where $\hat{\mathbf{e}}$ gives the polarization of the incident light as presented in section 3.3.2. This parameter is generally defined by [88]

$$R_{sp}^{\hat{\mathbf{e}}} = \int_0^{+\infty} r_{\hat{\mathbf{e}}}^{spon}(\hbar\omega)\, \mathrm{d}\hbar\omega \tag{3.46}$$

with $r_{\hat{\mathbf{e}}}^{spon}(\hbar\omega)$ the spontaneous emission spectrum as presented in sections 3.1 and 3.3. The total spontaneous emission rate per unit volume R_{sp} is defined as the average of the contributions from the three polarizations and, therefore, given by

$$R_{sp} = \frac{R_{sp}^{\hat{\mathbf{e}}_x} + R_{sp}^{\hat{\mathbf{e}}_y} + R_{sp}^{\hat{\mathbf{e}}_z}}{3} \tag{3.47}$$

In the previous equation, $\hat{\mathbf{e}}_x = (1, 0, 0)$ is the unit vector following the $\hat{\boldsymbol{x}}$-axis, $\hat{\mathbf{e}}_y$ is the unit vector following the $\hat{\boldsymbol{y}}$-axis, and $\hat{\mathbf{e}}_z$ is the one following the $\hat{\boldsymbol{z}}$-axis. With the assumption from equation (3.2), the momentum matrix elements are considered isotropic for bulk cubic semiconductors. In that case, $R_{sp}^{\hat{\mathbf{e}}_x}$, $R_{sp}^{\hat{\mathbf{e}}_y}$, and $R_{sp}^{\hat{\mathbf{e}}_z}$ should be the same and, therefore, the equations (3.47) and (3.46) should give the same result.

The net spontaneous recombination rate R_{sp}^{net} is defined as the amount by which the non-equilibrium spontaneous recombination rate R_{sp}^{neq} exceeds the thermal equilibrium generation rate G_0 [132]. At thermal equilibrium, the generation rate G_0 should be the same as the spontaneous emission rate R_{sp}^{eq}. In that case, R_{sp}^{net} may be written in the form

$$R_{sp}^{\text{net}} = R_{sp}^{\text{neq}} - R_{sp}^{\text{eq}} \tag{3.48}$$

The steady-state radiative carrier lifetime τ_{rad} is determined by the net spontaneous emission rate and the excess carrier concentration Δn, which gives equation (3.49) [132]

$$\tau_{\text{rad}} = \frac{\Delta n}{R_{sp}^{\text{net}}} \tag{3.49}$$

R_{sp} is usually estimated using equation (3.50) in which B is a material-dependent parameter, n, and p the electrons and holes charge densities, respectively.

$$R_{sp} = Bnp \tag{3.50}$$

In that case, the steady-state radiative carrier lifetime should be

$$\tau_{\text{rad}} = \frac{\Delta n}{B(n_0 + \Delta n)(p_0 + \Delta n) - Bn_0p_0} = \frac{1}{B(\Delta n + n_0 + p_0)} \tag{3.51}$$

There is a possibility for analytical computation of the coefficient B for a non-degenerate semiconductor in a low injection regime. Indeed, by assuming parabolic bands, we can derive the coefficient B as presented in equation (3.52) (see appendix B for the derivation).

$$B = \left[\sum_v \left(\frac{2m_{c,v}k_BT}{m_c}\right)^{3/2} \frac{E_{c,v}}{K_v(T)} \frac{\sqrt{\pi}}{2} \left(1 + \frac{3k_BT}{2E_{c,v}}\right)\right] \tag{3.52}$$

The bimolecular recombination coefficient is presented in equation (3.52) as independent of the excess carrier concentration (and therefore the quasi-Fermi levels), but this is not always true. In fact, B is known [133, 134] to depend on the carrier density Δn and is often

approximated by [135]

$$B = B_0 - B_1 \Delta n \tag{3.53}$$

with B_0 and B_1 which are material-dependent constants.
Given all that has been said about coefficient B, it seems wise to rely on equations (3.46), (3.47), and (3.49) which state the general case without any specific approximations.

3.5 The non-radiative recombination processes in single bulk semiconductor materials

3.5.1 Auger recombination process

The Auger recombination is a three-particle process where the energy released by the recombination event between two of the particles (electron-hole) is used to excite the third one. This energy is eventually lost to lattice phonons after the relaxation of this third carrier. Unlike the Shockley-Read-Hall (SRH) process described in the next section, the Auger recombination process is considered intrinsic to the material [136]. Although discovered in 1925, it was not until 1959 that this process was theoretically studied in semiconductors with the pioneering works of Beattie and Landsberg [137]. For an unstrained semiconductor, Beattie highlighted the existence of ten phonon-less band-to-band Auger processes [138] later on grouped in three main classes as presented in figure 3.4.

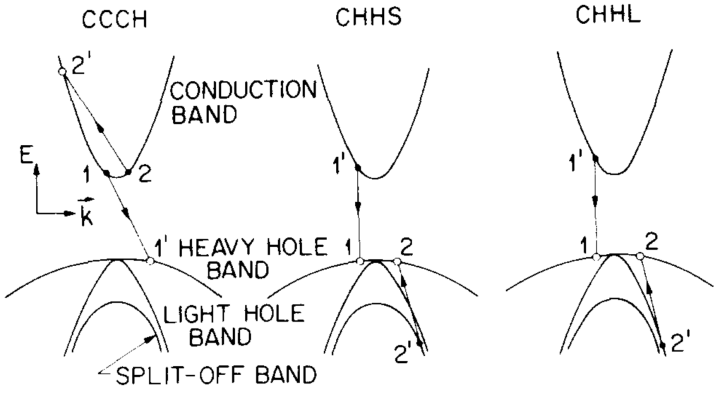

Figure 3.4 Band-to-band Auger processes. The electrons are represented by closed circles and holes by open circles. Reprinted from N. K. Dutta and R. J. Nelson, "The case for Auger recombination in $In_{1-x}Ga_xAs_yP_{1-y}$", Journal of Applied Physics 53, 74-92 (1982) https://doi.org/10.1063/1.329942 , with the permission of AIP Publishing [4].

In the CCCH process, the Coulomb interaction between the electrons 1 and 2 in the conduction band (C) results in the recombination of electron 1 with the hole 1' in the heavy-holes valence

band (H). The energy emitted after this recombination is captured by electron 2, which is excited to the higher energy state 2'. For the CHHS process, electron 1 recombines with hole 1', and the emitted energy is captured by the nearby heavy hole 2 (H), which is later excited to a spin-orbit split-off (S) hole band. The CHHL process is similar to the CHHS except for the heavy hole 2, which is excited to the light hole 2'. With these definitions, the CCCH process is expected to be significant when the electron concentration is high. The CHHS and CHHL would be notable for a material with a high density of holes. The CHHS process is said to dominate the CHHL when the bandgap energy E_g is greater than the split-off energy Δ and *vice versa*. For strained materials, it could be possible to see Auger recombination processes such as CCCL or CHLS since the heavy and light holes bands are split.

Auger recombination rate R_A is usually estimated using equation (3.54),

$$R_A = C_n n^2 p + C_p n p^2 \tag{3.54}$$

where n and p are the electron and hole charge carrier densities, respectively. C_n and C_p are the Auger coefficients linked to the CCCH and the CHHS/CHHL processes, respectively. They are material-dependent parameters usually determined experimentally.

There are two issues with this formula that need to be addressed. The first one is related to the lack of optimized parameters for relatively new semiconductors such as GeSn. This lack of parameters forces us to rely on approximations that are not always accurate. For example, Zhang et al. [139] used the values of the Auger coefficients from a tensile-strained n-type Ge to estimate R_A in a strained GeSn sample with 3% Sn. This approach could be relevant as a first approximation but, the impact of the doping concentration, the temperature, the strain, and the Sn content, even small, should not be neglected. The second issue, which is more general, is related to the derivation of the formula itself. Indeed, as mentioned by Larry Coldren et al. , this widespread definition of R_A is strictly valid only for non-degenerate semiconductors, where the Boltzmann approximation still holds [140]. In this situation, the SBEMA is sufficient to describe the band structure.

One of the main difficulties with the Auger recombination is to accurately evaluate the band structure more than a bandgap away from the band-edges. It is required to describe the charge carriers' behavior, especially the charge carrier 2' in figure 3.4. The computation of R_A also requires prior knowledge of the overlap integrals of the Bloch functions [137]. In addition to the pioneering work from 1959, more refined theoretical models were developed to evaluate the Auger recombination rate [4, 141–144]. However, the scarcity of experimental data on the band structure and the overlap integrals made these models relatively simplistic. To account for these effects, Haug developed a theoretical model in which the calculations are

performed with arbitrary band structures (meaning that the dependence on the wave vector $\vec{\boldsymbol{k}}$ is not as explicit as it could be with the SBEMA) [145]. Degenerate semiconductors are also taken into account with the use of the Fermi-Dirac distribution. It seems appropriate to use the multi-bands $\boldsymbol{k.p}$ to describe the band structure in this approach. In that case, the fourteen bands $\boldsymbol{k.p}$ model would at least be required to estimate the band structure more than a bandgap away from the band-edges.

It is relevant to mention that only the CCCH process can be accurately described by Haug's approach. The CHHL and CHHS processes are more complicated and, therefore, require more attention. Moreover, Haug presents the representation of the overlap integrals by the $\boldsymbol{k.p}$ perturbation theory as questionable since the $\vec{\boldsymbol{k}}$-differences in the Auger processes are not always small. Given the information provided above, it is pretty clear that the Auger recombination processes could not be accurately estimated within our theoretical framework.

3.5.2 Shockley-Read-Hall recombination process

SRH recombination mechanism is usually defined as a process involving the capture of minority carriers by quantum states lying in the semiconductor bandgap given the defects and imperfections in the material [146–148]. These defects include impurities, dislocations, lattice imperfections, unwanted foreign atoms, and even native defects such as interstitials and vacancies [3]. For a recombination center or a trap level of energy E_t in the bandgap, the total rate of electron capture U_{cn} is estimated by Shockley and Read in [147] and given by equation (3.55).

$$U_{cn} = C_n(f_{pt}n - f_t n_1) \tag{3.55}$$

In this equation, $f_{pt} = 1 - f(E_t) = 1 - f_t$ is the probability that a trap is empty, and f represents the Fermi-Dirac distribution. $n_1 = N_c \exp\left[(E_t - E_c)/k_B T\right]$, is the electrons charge concentration in the conduction band for the case in which the Fermi level falls at E_t. C_n is the probability per unit time that an electron in the conduction band will be captured by the traps when they are all empty.

The total rate of hole capture U_{cp} is estimated using the same approach and given by

$$U_{cp} = C_p(f_t p - f_{p,t} p_1) \tag{3.56}$$

It is worth mentioning that these equations were obtained for non-degenerate semiconductors. However, they can still be valid for degenerate semiconductors if we consider the definition of the mean capture coefficient $\langle c_n \rangle$ in equation (D.3) to provide an unambiguous meaning to the capture cross-sections [149].

For steady-state conditions, the quantities U_{cn} and U_{cp} must be equal, and the SRH recombination rate R_{SRH} is defined by equation (3.57) derived in several textbooks [95, 150, 151].

$$R_{SRH} = \frac{\sigma_n \sigma_p v_{th,n} v_{th,p} N_t (pn - p_1 n_1)}{\sigma_n v_{th,n} (n + n_1) + \sigma_p v_{th,p} (p + p_1)} \tag{3.57}$$

Here, N_t is the density of trapping centers per unit volume; σ_n and σ_p are the electron and hole capture cross-sections, respectively. $v_{th,i} = \sqrt{3k_B T/m_i^*}$ is the thermal velocity of the respective carrier. These parameters are linked to the probabilities C_n and C_p by equation (3.58).

$$C_n = \sigma_n N_t v_{th,n}, \quad C_p = \sigma_p N_t v_{th,p} \tag{3.58}$$

For non-degenerate semiconductors, N_c (N_v for the holes) is independent of the quasi-Fermi level μ_e (see equation (D.6)), and therefore, n_1 and p_1 are only functions of n_i the electron or hole concentration, and E_i the Fermi level both for an intrinsic semiconductor. In that case, equation (3.57) becomes

$$R_{SRH} = \frac{\sigma_n \sigma_p v_{th,n} v_{th,p} N_t [pn - n_i^2]}{\sigma_n v_{th,n} \left[n + n_i \exp\left(\frac{E_t - E_i}{k_B T}\right)\right] + \sigma_p v_{th,p} \left[p + n_i \exp\left(\frac{E_i - E_t}{k_B T}\right)\right]} \tag{3.59}$$

When the trap density N_t is negligible relative to the majority carrier densities under equilibrium conditions, the carrier charge densities n and p are supposed to be relatively insensitive to changing concentrations in the traps. In that case, the injected carrier concentrations Δn and Δp should be equal, and the SRH carrier lifetime τ_{SRH} is given by equation (3.60), where we have introduced the lifetimes $\tau_{p0} = (\sigma_p N_t v_{th,p})^{-1}$ and $\tau_{n0} = (\sigma_n N_t v_{th,n})^{-1}$.

$$\tau_{SRH} = \frac{\Delta n}{R_{SRH}} = \tau_{p0} \left(\frac{n_0 + \Delta n + n_1}{n_0 + p_0 + \Delta n} \right) + \tau_{n0} \left(\frac{p_0 + \Delta n + p_1}{n_0 + p_0 + \Delta n} \right) \tag{3.60}$$

For the general case, when the density of traps N_t is not small compared to the carrier charge densities, it becomes irrelevant to define an SRH carrier lifetime since $\Delta n \neq \Delta p$. In that case, there are two lifetimes τ_n and τ_p well described in appendix A of [147] for small values of Δn and Δp.

The SRH model presented here was extended by Macdonald and Cuevas [152] to account for arbitrary values of the density of traps N_t and the excess carrier densities Δn and Δp. The complexities in these SRH models are hidden behind the computation of the parameters C_n, C_p, N_c, N_t, and E_t. Indeed, as inferred from the previous equations, explicit knowledge of

these parameters is required. In many practical cases, the values of N_t and E_t are unknown. The problem with the energy level E_t is sometimes circumvented by considering deep-level states or mid-gap states for which $E_t = E_i$, the intrinsic Fermi level. The prior knowledge of the capture cross-sections is required to estimate the probabilities C_n and C_p. These cross-sections can be thermally activated, and their temperature dependence shall be included to find C_n and C_p [153].

In this chapter, the different steps required for the computation of the spontaneous emission spectrum were presented. While presenting the SBEMA, the chapter highlighted its weaknesses and the differences with the multi-band ***k.p*** formalism used in our framework. The framework presented here can also be used to describe both the inter-bands (CB-VB) and intra-valence bands absorption mechanisms. Besides the radiative processes, there was an emphasis on the non-radiative recombinations mechanisms such as Auger and SRH recombinations.

CHAPTER 4 EXPERIMENTAL DETAILS

This chapter provides an overview of different methods and techniques used throughout this project. It is divided into three sections, covering the growth process of GeSn, the microfabrication of devices, the characterization techniques used to investigate these materials and devices.

4.1 Heteroepitaxial growth of GeSn layers

Epitaxy is the oriented growth of one crystalline material on a substrate wafer. During this process, the substrate serves as a seed crystal since the grown layer duplicates its crystal structure as well as its orientation. According to Ivan Markov, epitaxial growth can only occur when the chemical potentials of the grown crystal and the substrate differ [154]. In that case, homoepitaxy takes place when this difference is mainly the result of the lattice mismatch rather than the difference in their chemistry. On the same line, heteroepitaxial growth occurs when the difference in the strength of the chemical bonds is the principal cause of the difference in the chemical potentials regardless of the lattice mismatch. During epitaxial growth, the difference in the lattice constants results in lattice strain in the grown layers. This lattice distortion yields different in-plane ($a_{L,\parallel}$) and out-of-plane lattice ($a_{L,\perp}$) parameters. For pseudomorphic growth, the value of $a_{L.\parallel}$ matches the in-plane lattice constant of the substrate (see figure 4.1). It results in a change in $a_{L,\perp}$ according to Poisson's ratio.

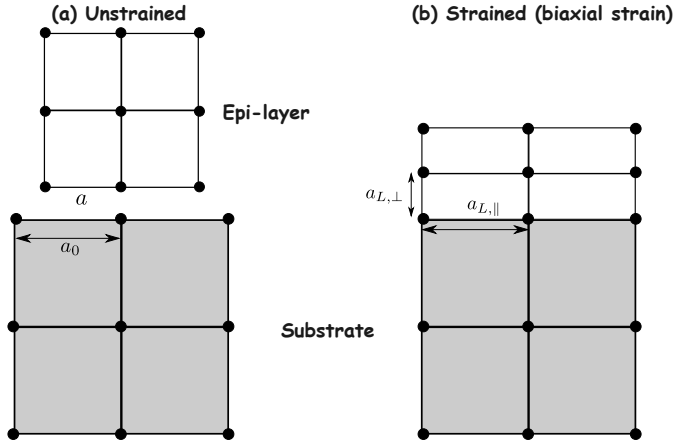

Figure 4.1 Example of a crystalline material to be grown epitaxially on a substrate wafer. (a) Unstrained (b) Strained: pseudomorphic growth.

CVD is one of the principal techniques used for the growth of semiconductor thin films and heterostructures. It consists of the deposition of solid thin layers on the surface of a heated

substrate by chemical reactions of gas-phase or vapor-phase precursor. The typical CVD process can be divided into several key steps [155]. First, the precursor chemicals and any required diluent gas must be fed into the CVD reactor. Once in the reactor, they decompose to form the film precursors and some volatile by-products. These film precursors are later transported to the substrate before adsorbing onto its surface. Once at the sample surface, the adatoms diffuse to the appropriate lattice sites and react with the surface atoms to be incorporated into the layer and form a continuous film. In the end, the reaction by-products, in addition to the excess precursors, desorb from the surface. They are transported to the reactor exhaust and pumped out of the system. Figure 4.2a presents a summary of the overall process.

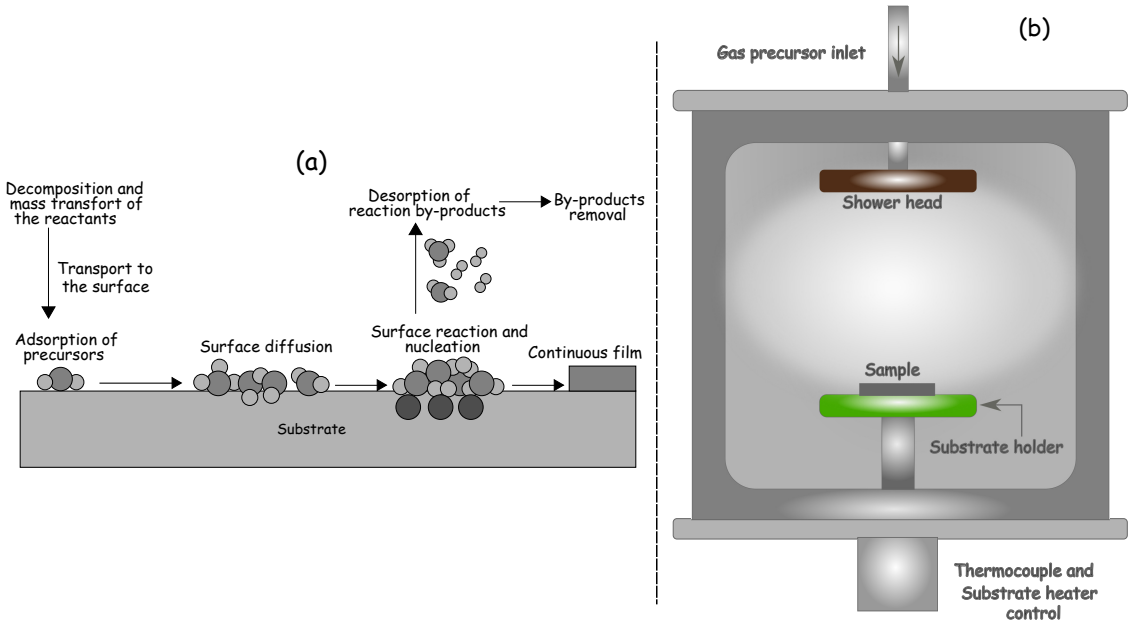

Figure 4.2 Thin films deposition. (a) Schematic representation of the typical CVD process. (b) Schematic illustration of the reduced pressure CVD reactor.

The GeSn samples used in this work were grown on 4-in. (100) Si wafers in a custom-made vertical RP-CVD system, from which a simplified schematic illustration is shown in panel (b) of figure 4.2. The Si wafers were first cleaned in a 2% hydrofluoric acid (HF) solution and put on the substrate holder in the chamber. The temperature of the substrate was kept constant by a feedback loop between the thermocouple and the heater. This heater also favors a good temperature uniformity during the film deposition. Before the growth of a GeSn layer, a $600 - 700\,\text{nm}$ thick Ge-VS was grown using ultrapure H_2 carrier gas and 10% monogermane (GeH_4) as a precursor. Subsequently, a thermal cycling annealing ($800\,^{\circ}\text{C}$) was performed, followed by the growth of additional Ge layers. The precursors used for GeSn film growth are GeH_4 and $SnCl_4$ for Ge and Sn, respectively. The liquid $SnCl_4$ was delivered to

the chamber using an H_2 bubbler which enabled the control of the $SnCl_4$ mass flow. Diborane (B_2H_6) and arsine (AsH_3) were used as precursors for *p*- and *n*-type doping, respectively. Further details on the growth process of Ge-VS and metastable GeSn are found in [156–158] and [5, 61, 68, 69, 159, 160], respectively.

4.2 Microfabrication of devices

4.2.1 Lithography

Lithography is a printing process used to transfer a pattern on a surface. Photolithography is the most widely used form of lithography in microfabrication [155]. With this process, a micro or nanoscale pattern is transferred to thin films material using UV light, a photomask (transparent plate of glass or quartz with opaque absorber pattern metals), and a photoactive organic material called photoresist. As the first step, the photoresist is deposited on the surface of the material by spin coating. By varying the time and speed of the spin process, the thickness of the resist can be controlled. After the photoresist deposition, the sample is baked, exposed to UV light, and later immersed in a developer solution to highlight the desired pattern. There are two types of resists used in photolithography, i.e., *positive* and *negative* photoresists. The exposed regions of a positive resist become more soluble due to the break of the polymer chains after reaction with light. For that reason, they dissolve faster in the developing solutions compared to the unexposed regions. In the case of negative photoresists, the exposed regions are rather strengthened, and therefore, they become less soluble than the other regions. For that reason, the unexposed areas are the ones being dissolved in the developing solution.

In addition to UV light, the pattern can also be transferred using either X-rays (X-ray lithography) or a focused beam of electrons (electron beam lithography (EBL)). X-rays have shorter wavelengths than UV light ($\sim 4 - 10\,\text{Å}$ compared to $\sim 2000 - 4000\,\text{Å}$). This difference allows for more energy to be conveyed to the material and, therefore, higher patterning resolution when using X-ray lithography [155]. Unlike photolithography and X-ray lithography, the EBL is maskless, and therefore, a more versatile process. It also yields higher patterning resolution (down to $< 10\,\text{nm}$) thanks to the high-energy electrons employed ($10 - 100\,\text{keV}$). However, the slow exposure speed and the need for vacuum make the EBL more complex and time-consuming than photolithography [155]. The EBL is, for example, used in the literature to fabricate GeSn-based microdisk optical cavities [79, 161–163]. On the other hand, GeSn-based LEDs in the literature have been patterned using photolithography [83]. Similarly, our LED in this work is also patterned using photolithography (see chapter 5).

4.2.2 Etching

In nano- and microfabrication, etching consists of the selective removal of regions of deposited layers or wafers. It is commonly used after a lithography process to transfer patterns from the resist to the layers of interest. Etching procedures are often divided into two classes mainly, *wet* and *dry* etching. Wet etching processes involve the immersion of the sample in chemical solutions, whereas dry etching employs ion bombardment, reactive chemical species, or combined physical and chemical mechanisms.

Reactive ion etching (RIE) is a chemical and physical dry etching technique. During this process, the organic material on top of the wafer surface reacts with high-energy ions from the chemically reactive plasma generated using a radio-frequency (RF) electromagnetic field in a low-pressure environment, i.e., in a vacuum chamber. In this environment, the wafer lies on one of the electrodes of the RF generator. After the plasma generation, this electrode acquires a negative charge, enhancing the negative bias on the wafer. This charge accumulation results in positive ion acceleration towards the wafer and energetic bombardment of its surface. Following the ion bombardment, the reactive species from the plasma diffuse to chemically attack the surface of the wafer. The directionality of the ions combined with the high reaction rate leads to highly anisotropic etching [155].

Inductively coupled plasma (ICP) RIE is a type of RIE used when higher etch uniformity and rates are required throughout the process. An ICP source is used to create and modulate the density of the plasma by electromagnetic induction whereas, a separate RF generator applies a bias to the wafer to control the energy of the ion [164]. Generally, high-density plasmas with low-energy ions and lower pressures are used to increase the etch rates in addition to the etch uniformity.

GeSn layers are etched using wet etching as well as dry etching techniques. Indeed, Cheng et al. investigated a wet etching process using ammonia peroxide mixture (H_2O_2:NH_4OH:H_2O) to fabricate full-relaxed GeSn patterns on Ge [165]. This process was later studied for $Ge_{1-x}Sn_x$ alloys with $4.2\% < x < 16.0\%$ [166]. Gupta et al. demonstrated in 2013 a new CF_4-based dry etching recipe to selectively remove the Germanium layer over GeSn [167]. However, as presented by Elbaz et al. , this etching recipe is unable to etch the defective area at the bottom interface between GeSn and Ge [168]. For that reason, they employed a dry etching recipe with SF_6 gas considered to be less selective compared to CF_4. Moreover, a Cl_2-based ($Cl_2/N_2/O_2$ gases) ICP RIE recipe was developed for more directional or vertical etching of GeSn [161, 169].

For the present work, the fabrication of the light-emitting devices relied on the directional

etching obtained using $Cl_2/N_2/O_2$ based ICP RIE technique.

4.3 Materials characterization

4.3.1 X-ray diffraction (XRD) and Reciprocal space mapping (RSM)

X-ray diffraction (XRD) is a well-established non-destructive method used for the structural characterization of crystals, especially epitaxial layers. It is widely used in the literature to estimate the strain, the chemical composition, and the degree of crystallinity of group IV semiconductors [31, 68, 69, 170–176]. This method relies on the elastic scattering of the incident X-rays by the atoms of a crystal, as presented in figure 4.3(a). Indeed, there are constructive and destructive interferences of scattered waves to form a diffraction pattern. The constructive interferences occur at specific angles θ estimated using Bragg's law:

$$m\lambda_{\mathrm{XRD}} = 2d_{hkl}\sin(\theta) \tag{4.1}$$

Here, λ_{XRD} is the wavelength of the incident X-ray beam, d_{hkl} is the distance between the (hkl) planes, and m is the diffraction order. The XRD measurements presented in this project were performed using a Bruker D8 Discovery, with the Kα_1 line ($\lambda = 0.15406\,\mathrm{nm}$) of a copper source as incident X-ray beams. Figure 4.3(b) presents a very simplified measurement setup.

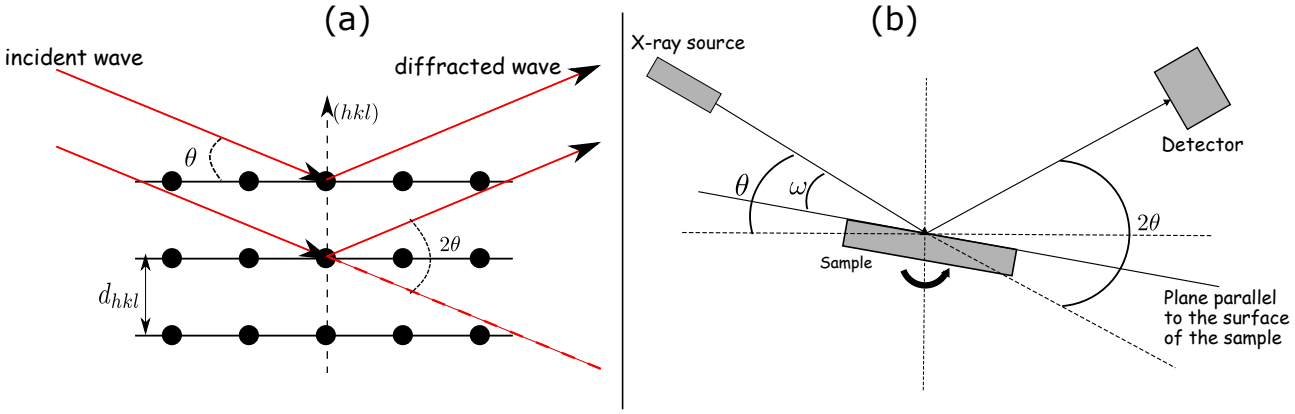

Figure 4.3 X-ray diffraction. (a) Schematic illustration of the Bragg's law. (b) Schematic illustration of the XRD setup

In this illustration, ω denotes the angle between the incident beam and the sample's surface, and 2θ is the angle between the incident and the diffracted beams. Three different scan modes are usually performed with this setup. The first is the ω scan (or rocking curve) performed by rotating the sample around the diffractometer axis while holding the detector at a specific position ($\theta \approx \theta_B$, the Bragg angle). This method enables the estimation of the mosaic spread,

and therefore, the crystal quality of the layers [177]. In addition to that mode, there is the standard $\omega - 2\theta$ scan around the (004) direction of Silicon. In this configuration, the detector is also rotated but twice as fast as the sample. For that reason, symmetry is maintained between the incident and the diffracted beams with respect to the sample's surface throughout the entire scanning range, and only the symmetrical Bragg reflections are captured in the diffraction pattern. This scan mode can give quick information about the crystal quality and the differences in the out-of-plane lattice parameters.

For a multi-layer heterostructure, the gradients of strain and chemical composition broaden the diffraction intensity distribution following different directions in the reciprocal space [177]. The XRD-reciprocal space mapping (RSM), which combined the scan modes above, is employed in this work to decouple the contributions of strain and Sn composition [178, 179]. The method also allows the evaluation of the epitaxial strain in the grown layers. It is noteworthy to mention that the lattice mismatches are the only parameters directly estimated with the XRD techniques. However, with basic elastic theory (Hooke's law), one can also evaluate the strain values. It is also possible to determine the chemical composition of a semiconductor alloy if the dependence of the lattice constants on the chemical composition is known [177]. For GeSn layers, the deviation of the lattice constant from Vegard's law is taken into account using a bowing parameter of 0.041 Å [66].

4.3.2 Photoluminescence spectroscopy

PL is the process of light emission by a material following the absorption of photons. After absorbing the photons, the system is excited to a higher energy level, and subsequent emission of photons occurs due to spontaneous decay to lower energy levels. According to Stokes's law, the wavelength of the emitted photons should be greater than the one of the excitation light [180]. The eventual excess of energy is lost through non-radiative transitions. A luminescence that does not follow this law is referred to as anti-Stokes luminescence. They usually occur when the excited electron receives additional energy following its interaction with the crystal lattice or when a two-photon absorption process takes place [181]. Photoluminescence spectroscopy is a helpful tool for investigating the band structure and the optical properties of semiconductors usually conveyed by the optical transitions inside the materials.

While PL spectroscopy in the visible part of the electromagnetic spectrum is an easy technique [182], it is not necessarily the case in the infrared. Indeed, the atmospheric absorption lines and the thermal background radiation, in addition to the reduced sensitivity of detectors in the infrared, are some of the challenges facing near-infrared (NIR) and MWIR PL.

For the measurements presented in chapter 5, Fourier Transform InfraRed (FTIR) spectroscopy, which relies on the Michelson interferometer [183], is our preferred technology. This technology has various advantages over the earlier conventional dispersive systems (e.g., grating or prism). In the FTIR spectrometer, there is a simultaneous observation of all the wavenumbers of light at all times, instead of a sequential observation as in the case of dispersive spectrometers. This difference is known as the multiplex (Fellgett's) advantage and results in higher signal-to-noise ratios in the spectra recorded with FTIR spectrometers [184]. The improved signal-to-noise ratio is also the consequence of the higher optical throughput (known as throughput or Jacquinot's advantage) due to the absence of slits in FTIR instruments [184]. In FTIR spectrometers, a laser output, usually He-Ne laser, is used as a reference to estimate the frequencies in the output spectrum. With the accurate and stable estimation of the wavenumber of the He-Ne laser, the calibration of FTIR interferometers is much more precise and reliable in comparison to the dispersive systems [184]. This stability of calibration is the laser reference or Connes' advantage.

A schematic representation of our PL setup is presented in figure 4.4. The excitation consists

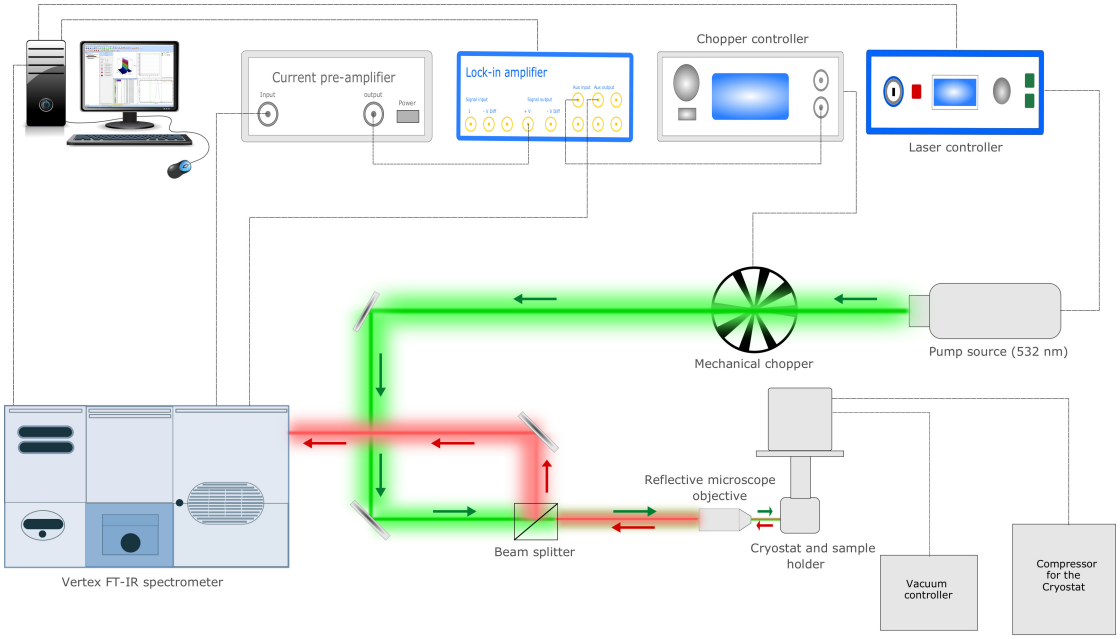

Figure 4.4 Schematic representation of the FTIR based photoluminescence setup.

of a continuous-wave 532 nm laser from Laser Quantum. The laser is focused onto the sample after following the green path. The 25× reflective microscope objective and the beam splitter are used to collect the PL signal and couple it into the VERTEX 80 FTIR spectrometer from Bruker. The PL signal goes through the interferometer compartment equipped with a Calcium fluoride (CaF_2) beamsplitter and later focused onto the liquid nitrogen (N_2) cooled

Indium Antimonide (InSb) detector (spectral range of $1 - 5.4\,\mu m$). The laser signal is filtered out from the PL signal using a germanium window as a longwave-pass filter, which cuts on at 1850 nm.

The PL measurements were performed at a resolution of $32\,cm^{-1}$ ($\approx 4\,meV$) or $128\,cm^{-1}$ ($\approx 16\,meV$). The Fourier transform process uses the three-term Blackman-Harris apodization function and the power spectrum as phase correction mode [185, 186].

In order to remove the thermal background radiation from the PL signal, the excitation laser is modulated using a mechanical chopper wheel at a specific frequency. It results in a modulation of the PL signal with the same frequency and its amplification via a lock-in amplifier [187, 188]. The FTIR spectrometer was then operated in its step-scan function to account for this laser modulation [189].

The experimental methods presented in this chapter are of primary importance to assess the accuracy of the theoretical framework developed in chapter 3. While the epitaxial growth and the microfabrication techniques ensure the availability of the materials and devices, the different characterization techniques are commonly used to evaluate the material properties of semiconductors. The Sn composition and the lattice strain are some of the parameters estimated using XRD. These parameters are crucial to elaborate the band structure of $Ge_{1-x}Sn_x$ alloys. Photoluminescence spectroscopy also provides a set of experimental data relevant for the benchmarking of the framework.

CHAPTER 5 CHARACTERIZATION OF GeSn LIGHT-EMITTERS: COMPARISON BETWEEN THEORY AND EXPERIMENT

This chapter presents the results of the numerical studies performed on a $Ge_{0.83}Sn_{0.17}$ material [5] using the theoretical framework developed in chapter 3. Additionally, GeSn double heterostructure (DH) based LEDs are demonstrated and discussed. The experimental results are analyzed and interpreted with a focus on the optical properties of the materials.

5.1 Mid-infrared emission from strained and relaxed direct bandgap $Ge_{0.83}Sn_{0.17}$ semiconductor

The epitaxial growth of the $Ge_{0.83}Sn_{0.17}$ layers was carried out using low-pressure chemical vapor deposition (LP-CVD) starting from a 600 - 700 nm Ge virtual substrate on a 4-in. silicon wafer. To ensure the growth of a $Ge_{0.83}Sn_{0.17}$ layer with a uniform Sn composition, a multilayer heterostructure top layer (TL)/middle layer (ML)/bottom layer (BL) was grown. The incorporation of Sn in the different layers was controlled using the growth temperature and later estimated from an RSM analysis around the (224) asymmetrical XRD peak. Figure 5.1 shows the results of the scanning transmission electron microscope (STEM) and XRD-RSM analyses. The thicknesses of the TL/ML/BL stacking were estimated to be 160/155/65 nm. Besides, the TL is compressively strained with a lattice strain around -1.3%, as presented in figure 5.1-b. The grown layers were also patterned into microdisks to relax the epitaxial lattice strain and decouple the impact of both the lattice strain and the Sn composition on the optical emission of the $Ge_{0.83}Sn_{0.17}$ layer (see figure 5.1c).

Figure 5.2 shows the band lineup diagrams of the $Ge_{0.92}Sn_{0.08}/Ge_{0.88}Sn_{0.12}/Ge_{0.83}Sn_{0.17}$ obtained within the eight bands ***k.p*** formalism. In both the as-grown and relaxed samples, the electrons and holes are expected to diffuse to the TL, where they should recombine. In that case, the PL spectrum should be mainly the result of the recombination from this layer. Therefore, from a theoretical standpoint, it would be judicious to analyze the PL results as if they were coming from a single bulk GeSn material with a 17 at. % Sn composition.

5.1.1 $Ge_{0.83}Sn_{0.17}$ band structure : single-band effective mass approximation and eight bands *k.p* formalism

The SBEMA requires prior knowledge of the effective masses for electrons and holes, as presented in equation (3.3). Different research groups investigated the variation of the

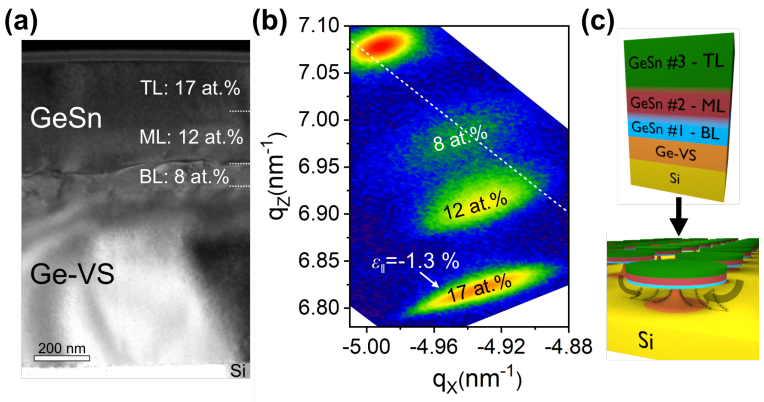

Figure 5.1 Cross-sectional TEM image along the [110] zone axis of the $Ge_{1-x}Sn_x$ 17/12/8 at. % (TL/ML/BL) multilayer heterostructure grown on the Ge-VS/Si substrate. (b) XRD RSM around the asymmetrical (224) reflection for the as-grown $Ge_{0.83}Sn_{0.17}$ sample. (c) Schematics of the microdisk fabrication process. Reprinted figure with permission from [5]. Copyright 2021 by the American Physical Society.

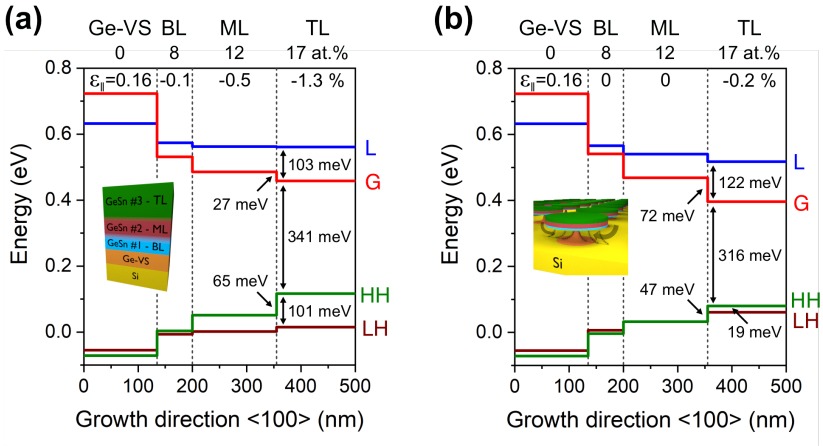

Figure 5.2 (a),(b) Calculated 8×8 *k.p* band lineup at 300 K for the $Ge_{0.83}Sn_{0.17}$ with an in-plane biaxial strain $\varepsilon_{\parallel} = -1.3\%$ (as grown) (a) and $\varepsilon_{\parallel} = -0.2\%$ (microdisks). Reprinted figure with permission from [5]. Copyright 2021 by the American Physical Society.

effective masses as a function of the Sn composition for unstrained GeSn materials [2, 190]. A quadratic evolution was demonstrated depending on the wave vector direction studied. For biaxially strained GeSn, the strain tensor is expected to modify the band structure and, therefore, the effective masses. In that case, these different masses can be extracted from the eight bands ***k.p*** bandstructure as presented in equation (5.1) with β representing the specific $\hat{\boldsymbol{k}}$-vector direction ([100], [110], or [111]). The [100] effective masses could be used to satisfy the isotropy assumption of the SBEMA. Another idea is to average the masses following the different directions to obtain a new set of masses that could be used as an input parameter

for the SBEMA.

$$\frac{1}{m^*_{c,v}|_\beta} = \left(\frac{1}{\hbar^2}\left|\frac{\partial^2 E_\beta}{\partial k^2}\right|\right)\Big|_{k=0} \tag{5.1}$$

Figures 5.3 and 5.4 present the band structures at 4 K and 300 K resulting from the different formalisms mentioned before. The SBEMA band structure seems to be different depending on the set of masses used. As expected, there is almost a perfect match between the SBEMA and the eight bands ***k.p*** for a specific range of wave vectors very close to the Γ point. This range is somehow dependent on the strain and the temperature in the material. For example, we identify the ranges $-0.118\,\mathrm{nm}^{-1} \leq k \leq 0.161\,\mathrm{nm}^{-1}$ and $-0.076\,\mathrm{nm}^{-1} \leq k \leq 0.099\,\mathrm{nm}^{-1}$ at 4 K for the as-grown and the relaxed TL, respectively. At 300 K, these ranges become $-0.197\,\mathrm{nm}^{-1} \leq k \leq 0.145\,\mathrm{nm}^{-1}$ and $-0.084\,\mathrm{nm}^{-1} \leq k \leq 0.104\,\mathrm{nm}^{-1}$ for the as-grown and the relaxed TL, respectively. However, some differences are observed when the $\vec{\boldsymbol{k}}$ vector moves away from the Γ point. These differences are more significant for the valence bands, with, for example, the bands crossing resulting from the SBEMA for both unstrained and biaxially strained materials. From these results, some differences should be expected in the evaluation of the emission characteristics with the SBEMA and the eight bands ***k.p*** formalism.

5.1.2 Determination of the quasi-Fermi levels for $\mathbf{Ge_{0.83}Sn_{0.17}}$

Equation (3.10) is sometimes convenient to evaluate the edge-to-edge bandgap energy E_g of semiconductors from PL measurements. This formula contains only two free parameters, i.e., the bandgap E_g and the full width at half maximum (FWHM) of the broadening function. The accuracy of this method is based on the somehow restricting assumption of a non-degenerately doped semiconductor and the fact that the optical carrier injection would be small enough to maintain the quasi-Fermi levels within the bandgap and away from the different band edges by several k_BT [3]. This assumption is in some way problematic since power-dependent PL analysis cannot be performed for fear of finding an evolution of the edge-to-edge bandgap energy E_g as a function of the injected excess carriers density. This evolution should not be confused with the Burstein-Moss effect [191], which mainly deals with the variation of the optical energy gap $E_0(\neq E_g)$ as a function of the carrier's density. For an n-type semiconductor at thermal equilibrium, E_0 is defined as the energy difference between the valence band maximum and the Fermi level position in the conduction band. Its variation results from the shift of the Fermi level relative to the band edges as more charge carriers are injected inside the material. Equation (3.6) and its underlying formalism can therefore be used as a solution since they rely on the SBEMA while ignoring the different assumptions mentioned before. An even more accurate alternative would be to rely on the framework developed in chapter 3 based on the eight bands ***k.p*** formalism.

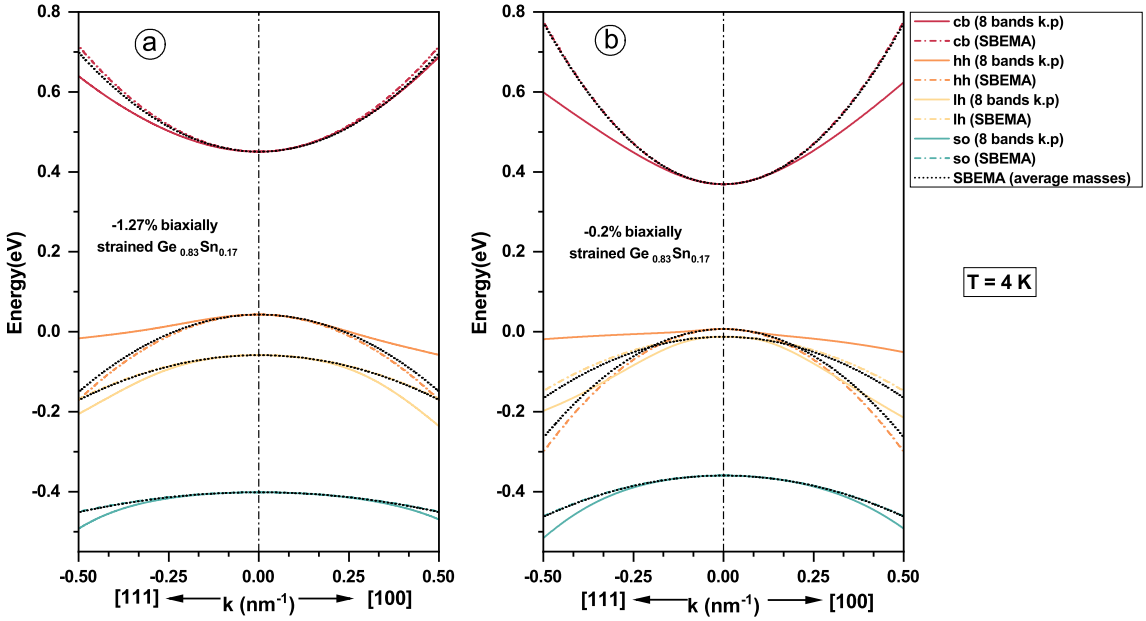

Figure 5.3 Comparison of the single-band effective mass approximation and the eight bands ***k.p*** bandstructures for $Ge_{0.83}Sn_{0.17}$ at 4 K.

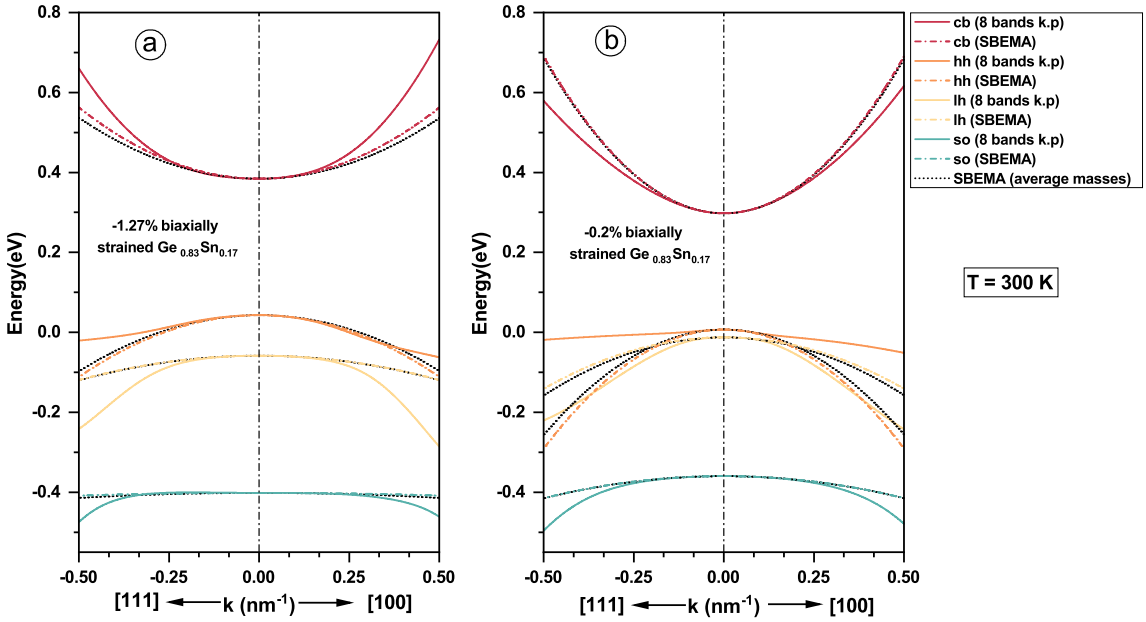

Figure 5.4 Comparison of the single-band effective mass approximation and the eight bands ***k.p*** bandstructures for $Ge_{0.83}Sn_{0.17}$ at 300 K.

The quasi-Fermi levels require accurate computations of the carrier charge densities, as presented previously in chapter 3. With the differences in the band structure highlighted in the previous section, the carrier densities would be dependent on the formalism used. The calculations using the eight bands ***k.p*** formalism require defining the set of "special" directions to consider for the integrals over the BZ. The computation times would depend on the number of directions considered. Note, however, that for both as-grown and relaxed $Ge_{0.83}Sn_{0.17}$, the number of directions is much reduced. Indeed, the seventy-four lines previously mentioned are grouped into eight classes, as shown in figure 5.5, highlighting the band structure of the as-grown material following different directions of the wave vector $\vec{\boldsymbol{k}}$. Panel (a) in figure 5.5

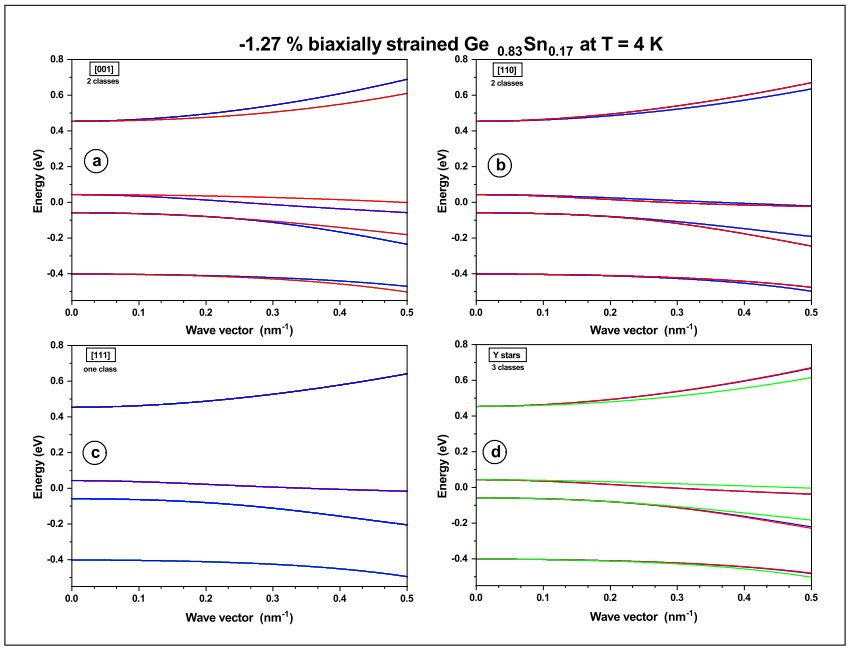

Figure 5.5 Determination of the "special" directions considered within the special-lines approximation for the computation of the integrals over the Brillouin zone for a -1.27 % biaxially strained $Ge_{0.83}Sn_{0.17}$.

presents the gathering of the [100] six degeneracies into two main classes. The [100] direction becomes four-fold degenerated and [001] two-fold. It is also the case for [110] that is now four-fold degenerated while [101] is eight-fold. The [111] direction leads to only one class as presented on panel (c). Regarding the Y stars, panel (d) highlights only three lines, each of them sixteen-fold degenerated. The set $\mathcal{L}$ to be considered within the SLA is, therefore, given by

$$\begin{aligned}\mathcal{L} = \Big\{&[100], [001], [110], [101], [111], [1, \sqrt{2}-1, \sqrt{3}-\sqrt{2}],\\ &[1, \sqrt{3}-\sqrt{2}, \sqrt{2}-1], [\sqrt{3}-\sqrt{2}, \sqrt{2}-1, 1]\ \}\end{aligned} \tag{5.2}$$

Figure 5.6 presents the results for the computations of electron and hole densities at 4 K using both the eight bands $\boldsymbol{k.p}$ formalism (equation (3.36)) and the SBEMA (equation (3.38)). In this figure, "SLA (26 lines)" corresponds to the computation with the set $\mathcal{L}$ from equation (3.44) while "SLA (74 lines)" highlights the impact of the extra forty-eight Y stars on the charge carrier's density. Regarding the "SLA (8 lines)", it is the set from equation (5.2) that is considered. For "SLA (5 lines)", the impact of the three additional Y stars classes in equation (5.2) is ignored. The observations from figure 5.5 are pretty much confirmed here since the contribution from the supplementary directions within the set $\mathcal{L}$ is negligible. Panels (a) and (b) show the slight impact of the Y stars on the electrons' charge densities in both the as-grown and the relaxed $Ge_{0.83}Sn_{0.17}$. The picture is somehow different for the holes since there is one region where the impact of these stars is negligible along with the other one where it is visible even though reduced for the -0.2 % biaxially strained $Ge_{0.83}Sn_{0.17}$ material.

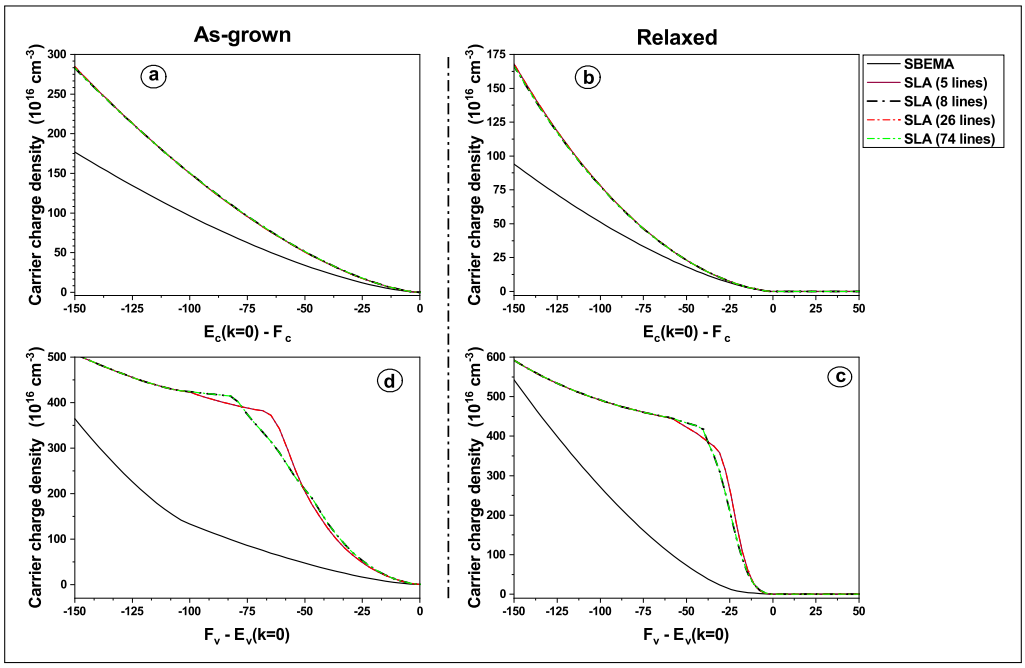

Figure 5.6 Computation of the charge carrier densities for both as-grown and relaxed $Ge_{0.83}Sn_{0.17}$ at T = 4 K.

An almost perfect match between the $\boldsymbol{k.p}$ and the SBEMA results is observed when the electrons (holes) quasi-Fermi level is between the bandgap energy and the conduction (valence) band edge. This result is explained by the accumulation of carriers very close to the Γ point, where a perfect match between the $\boldsymbol{k.p}$ and the SBEMA band structures is observed (see figures 5.3 and 5.4). When the quasi-Fermi levels shift into the bands, the differences in the band structure start to be significant. In that case, the equations (3.36) and (3.38) give completely different results for the electrons and the holes. Therefore, the values of the

quasi-Fermi levels are expected to change depending on the doping densities, the excess carrier's concentration, and the formalism used. The spontaneous emission intensities would also be different since they are exponentially dependent on the quasi-Fermi levels.

5.1.3 Momentum matrix elements for $Ge_{0.83}Sn_{0.17}$

The optical momentum matrix element in a bulk semiconductor is usually considered independent of the polarization of the electromagnetic field. This isotropy is expressed by replacing the momentum matrix elements $M_{cv}^2(\vec{\boldsymbol{k}})$ in equation (3.1) with their average over the solid angle $d\Omega$ (see section 9.5 and appendix 9A of [88] for more information about the process). In this process, the band-edge wave functions are the main contributors to the optical transitions. In that case, the envelope functions are independent of the wave vector $\vec{\boldsymbol{k}}$ since they are defined, as in equation (5.3) with, δ being the Kronecker delta function.

$$\begin{aligned}
\left|\Phi_{CB}(\vec{\boldsymbol{k}})\right\rangle &\approx |S\uparrow\rangle = (\delta_{i,1})_{1\leq i\leq 8} & \left|\Phi_{CB}(\vec{\boldsymbol{k}})\right\rangle &\approx |S\downarrow\rangle = (\delta_{i,2})_{1\leq i\leq 8} \\
\left|\Psi_{HH}(\vec{\boldsymbol{k}})\right\rangle &\approx |HH\uparrow\rangle = (\delta_{i,3})_{1\leq i\leq 8} \quad \text{or} & \left|\Psi_{HH}(\vec{\boldsymbol{k}})\right\rangle &\approx |HH\downarrow\rangle = (\delta_{i,6})_{1\leq i\leq 8} \\
\left|\Psi_{LH}(\vec{\boldsymbol{k}})\right\rangle &\approx |LH\uparrow\rangle = (\delta_{i,4})_{1\leq i\leq 8} & \left|\Psi_{LH}(\vec{\boldsymbol{k}})\right\rangle &\approx |LH\downarrow\rangle = (\delta_{i,5})_{1\leq i\leq 8} \\
\left|\Psi_{SO}(\vec{\boldsymbol{k}})\right\rangle &\approx |SO\uparrow\rangle = (\delta_{i,7})_{1\leq i\leq 8} & \left|\Psi_{SO}(\vec{\boldsymbol{k}})\right\rangle &\approx |SO\downarrow\rangle = (\delta_{i,8})_{1\leq i\leq 8}
\end{aligned} \tag{5.3}$$

For the $Ge_{0.83}Sn_{0.17}$ grown following the [100] direction, the wave vector directions relevant for the calculations are more or less known. For that reason, there is no need for an average since $M_{cv}^2(\vec{\boldsymbol{k}})$ can be explicitly computed, following the process described in section 3.3.2. In addition, the envelope functions don't fully respect the approximations given in equation (5.3). As presented in tables 5.1 and 5.2, they depend on the wave vector $\vec{\boldsymbol{k}}$ and, their unpredictable variations deserve to be taken into account regardless of their amplitude.

Table 5.1 – Envelope wave functions at $\vec{\boldsymbol{k}} = (0,0,0)$ and T = 4 K for the -1.27% biaxially strained $Ge_{0.83}Sn_{0.17}$

	$\lvert\Phi_{S\uparrow}\rangle$	$\lvert\Phi_{S\downarrow}\rangle$	$\lvert\Phi_{HH\downarrow}\rangle$	$\lvert\Phi_{HH\uparrow}\rangle$	$\lvert\Phi_{LH\downarrow}\rangle$	$\lvert\Phi_{LH\uparrow}\rangle$	$\lvert\Phi_{SO\downarrow}\rangle$	$\lvert\Phi_{SO\uparrow}\rangle$
$\lvert S\uparrow\rangle$	1	0	0	0	0	0	0	0
$\lvert S\downarrow\rangle$	0	1	0	0	0	0	0	0
$\lvert HH\uparrow\rangle$	0	0	0	1	0	0	0	0
$\lvert LH\uparrow\rangle$	0	0	0	0	-3.0533×10^{-16}	-0.9625	0	-0.2713
$\lvert LH\downarrow\rangle$	0	0	0	0	-0.9625	2.7756×10^{-16}	0.2713	1.1102×10^{-16}
$\lvert HH\downarrow\rangle$	0	0	-1	0	0	0	0	0
$\lvert SO\uparrow\rangle$	0	0	0	0	0	-0.2713	0	0.9625
$\lvert SO\downarrow\rangle$	0	0	0	0	0.2713	-7.9724×10^{-17}	0.9625	-2.2471×10^{-17}

Table 5.2 – Envelope wave functions at $\vec{k} = (0.01, 0, 0)$ and T = 4 K for the -1.27% biaxially strained $Ge_{0.83}Sn_{0.17}$

	$\|\Phi_{S\uparrow}\rangle$	$\|\Phi_{S\downarrow}\rangle$	$\|\Phi_{HH\downarrow}\rangle$	$\|\Phi_{HH\uparrow}\rangle$	$\|\Phi_{LH\downarrow}\rangle$	$\|\Phi_{LH\uparrow}\rangle$	$\|\Phi_{SO\downarrow}\rangle$	$\|\Phi_{SO\uparrow}\rangle$
$\|S\uparrow\rangle$	0.0022	0.9998	$2.5350{\cdot}10^{-4}$	-0.0172	-0.0107	$-4.9208{\cdot}10^{-4}$	$7.9498{\cdot}10^{-18}$	0.0052
$\|S\downarrow\rangle$	0.9998	-0.0022	0.0172	$2.535{\cdot}10^{-4}$	$-4.9208{\cdot}10^{-4}$	0.0107	-0.0052	$4.6562{\cdot}10^{-19}$
$\|HH\uparrow\rangle$	$-3.8643{\cdot}10^{-5}$	-0.0172	0.0147	-0.9997	$-3.3451{\cdot}10^{-4}$	$-1.5354{\cdot}10^{-5}$	$2.2086{\cdot}10^{-17}$	$6.5896{\cdot}10^{-6}$
$\|LH\uparrow\rangle$	-0.0089	$1.9991{\cdot}10^{-5}$	$-4.7418{\cdot}10^{-4}$	$-6.9775{\cdot}10^{-6}$	-0.0441	0.9614	0.2713	$-1.7791{\cdot}10^{-17}$
$\|LH\downarrow\rangle$	$1.9991{\cdot}10^{-5}$	0.0089	$6.9775{\cdot}10^{-6}$	$-4.7418{\cdot}10^{-4}$	0.9614	0.0441	$-2.0847{\cdot}10^{-16}$	0.2713
$\|HH\downarrow\rangle$	0.0172	$-3.8643{\cdot}10^{-5}$	-0.9997	-0.0147	$1.5354{\cdot}10^{-5}$	$-3.3451{\cdot}10^{-4}$	$6.5896{\cdot}10^{-6}$	0
$\|SO\uparrow\rangle$	-0.0079	$1.7719{\cdot}10^{-5}$	$-2.3336{\cdot}10^{-4}$	$-3.4338{\cdot}10^{-6}$	-0.0124	0.2709	-0.9625	$1.1102{\cdot}10^{-16}$
$\|SO\downarrow\rangle$	$-1.7719{\cdot}10^{-5}$	-0.0079	$-3.4338{\cdot}10^{-6}$	$2.3336{\cdot}10^{-4}$	-0.2709	-0.0124	$1.1407{\cdot}10^{-16}$	0.9625

Figure 5.7 presents the polarization dependence of the strength of the different optical transitions between the conduction and the valence bands for the as-grown $Ge_{0.83}Sn_{0.17}$ layer. The wave vector $\vec{k}$ varies following the [100] direction. Panels (a) and (b) present the contributions from the transverse electric (TE) polarization which is obtained by using $\hat{\mathbf{e}} = (1, 0, 0)$ in equation (3.33) and the the transverse magnetic (TM) polarization for which $\hat{\mathbf{e}} = (0, 0, 1)$. In figure 5.8, the impact of the special directions on the strengths of the transitions is presented. Indeed, this figure shows the behavior of the momentum matrix elements following the $[100], [110]$, and $[111]$ directions. Rather than comparing the transverse electric (TE) and the transverse magnetic (TM) separately, the average of the three polarizations $(2 \times TE + TM)/3$ is studied.

5.1.4 Spontaneous emission spectrum : single-band effective mass approximation and eight bands *k.p* formalism

This section gathers all the previous pieces of information presented to analyze the impact of the formalism on the final parameter which, is the spontaneous emission spectrum r^{spon}. The results of the comparison between the SBEMA, using equation (3.6) and the eight-bands ***k.p*** formalism using equation (3.1) are highlighted. As presented in section 3.3.3, the determination of the quasi-Fermi levels involves the excess carrier concentration Δn as an input or fitting parameter. Here, different values of Δn were used to study the differences between these two formalisms. Figures 5.9 and 5.10 summarize the results of these computations. The insets in the different panels are used to present the impact of the formalism on the emission peak position.

For the as-grown sample with an unintentional residual p-doping of 10^{17}cm^{-3}, the thermal equilibrium electron charge density n_0 is far more negligible relative to the hole charge density $p_0 \approx 10^{17}\text{cm}^{-3}$. In that case, at $\Delta n = 10^{14}\text{cm}^{-3}$, only a slight difference in the values of μ_e,

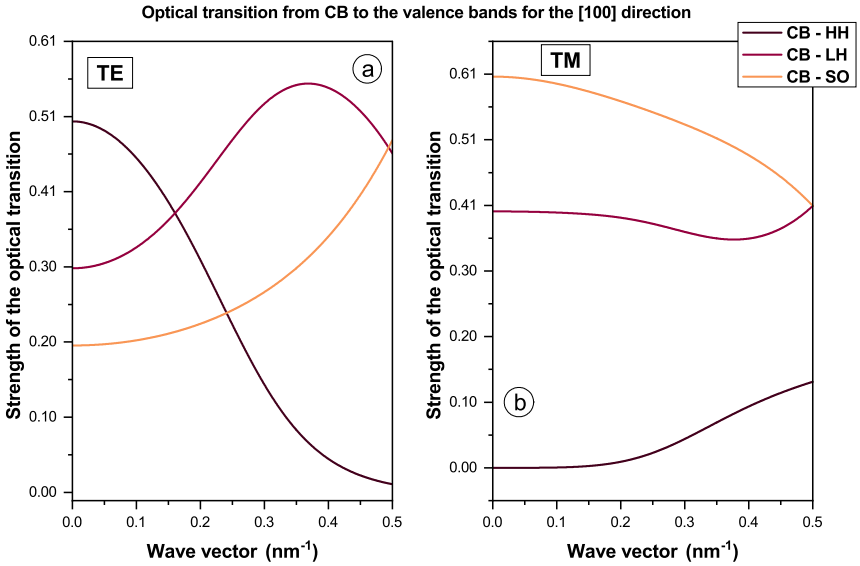

Figure 5.7 Optical strength of the transitions between the conduction and valence bands for the as-grown $Ge_{0.83}Sn_{0.17}$ at T = 4 K. Here, the wave vector $\vec{\boldsymbol{k}}$ is along the [1 0 0] direction. The contribution from the transverse electric (TE) polarization is found using $\hat{\mathbf{e}} = (1, 0, 0)$ in equation (3.33). For the transverse magnetic (TM), $\hat{\mathbf{e}} = (0, 0, 1)$. The $\hat{\boldsymbol{y}}$-axis is divided by P^2 with P the Kane parameter.

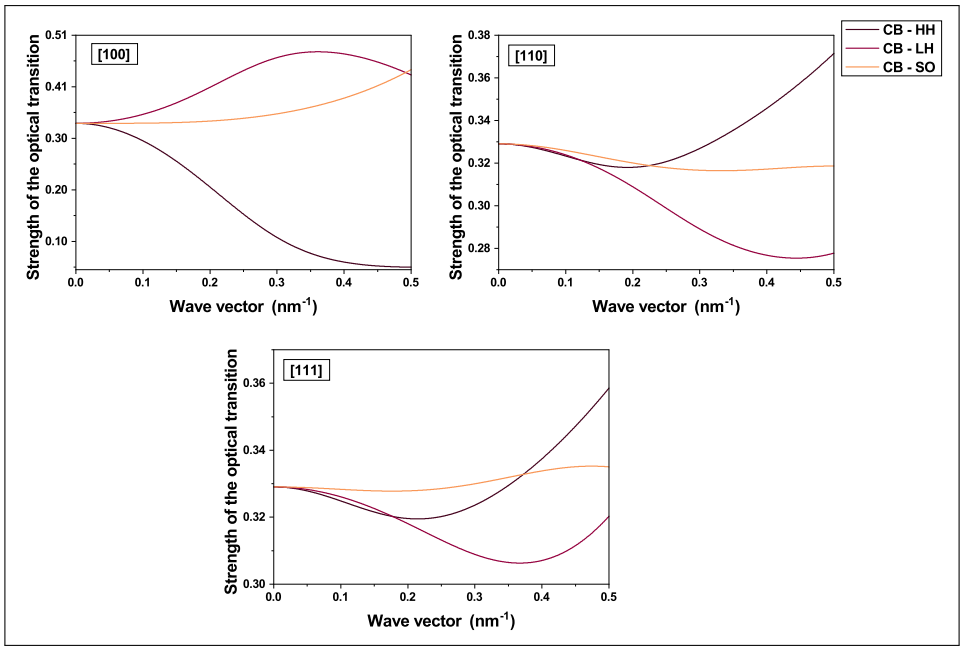

Figure 5.8 Comparison of the unpolarized optical strengths of the transitions between the conduction and valence bands for the as-grown $Ge_{0.83}Sn_{0.17}$ at T = 4 K. The unpolarized strengths are defined following the formula $(2M^2_{cv,TE} + M^2_{cv,TM})/3$

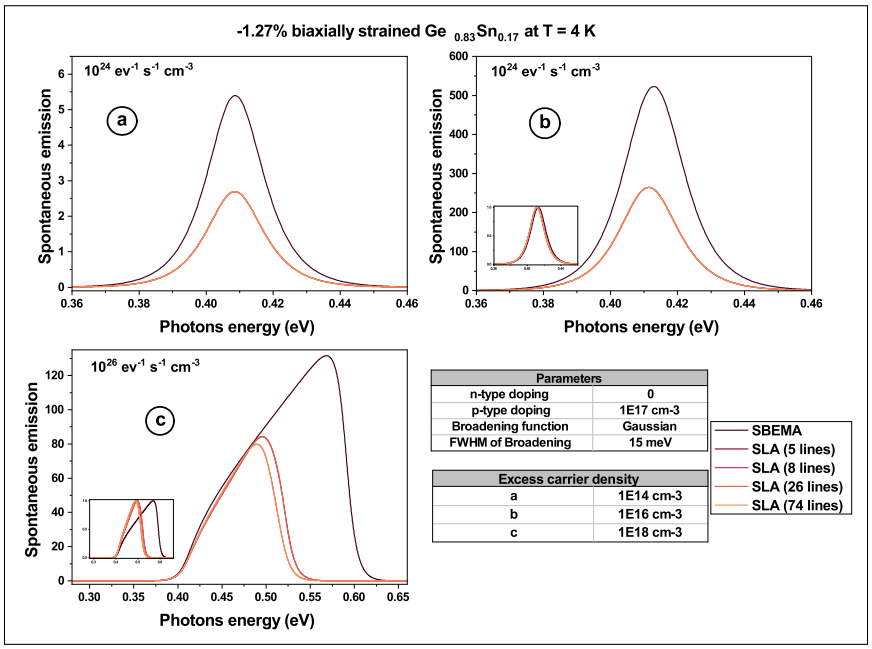

Figure 5.9 Comparison of the spontaneous emission spectra for the as-grown $Ge_{0.83}Sn_{0.17}$ at T = 4 K. Some of the parameters used during the computations are presented in the tables on the right

the electron quasi-Fermi level, is expected since $n \approx \Delta n$ (see panel (a) of figure 5.6). For the holes, the value of the excess carrier concentration is negligible compared to p_0. Therefore, the energy difference between the hole quasi-Fermi level μ_h and the valence band edge should be between $-25\,\text{meV}$ and $0\,\text{meV}$. In this region, the value of the carrier charge density estimated using the eight-bands $\boldsymbol{k.p}$ is not that far from the one obtained using the SBEMA (see panel (d) of figure 5.6). The results from panel (a) of figure 5.9 are therefore not surprising. However, as soon as Δn is increased, the two formalisms lead to different results. It is, for example, the case for the injected carrier density around 10^{16}cm^{-3}, where a very slight shift of the emission peak position is observed. These differences are more significant for Δn above p_0, as shown in panel (c) for the value of 10^{18}cm^{-3}. Indeed, the peak position completely moves from around $0.575\,\text{eV}$ (SBEMA) to $0.475\,\text{eV}$ (eight-bands $\boldsymbol{k.p}$). Regarding the differences observed between the emission intensities, they could be explained by the exponential dependence in μ_e and μ_h of the spontaneous emission spectrum. Indeed, no matter how small they are, the differences in the values of $\mu_{e,h}$ obtained from SBEMA and the ones from the eight-bands $\boldsymbol{k.p}$ contribute to the increase or decrease of the emission intensity. The variation of M_{cv}^2 as a function of the wave vector $\vec{\boldsymbol{k}}$ in the $\boldsymbol{k.p}$ formalism also impacts the emission intensity and leads to the differences previously mentioned. The different values of μ_e and μ_h, as well as the emission intensities R_{sp}, can be seen in table 5.3. All the different explanations presented above are also valid for the relaxed $Ge_{0.83}Sn_{0.17}$.

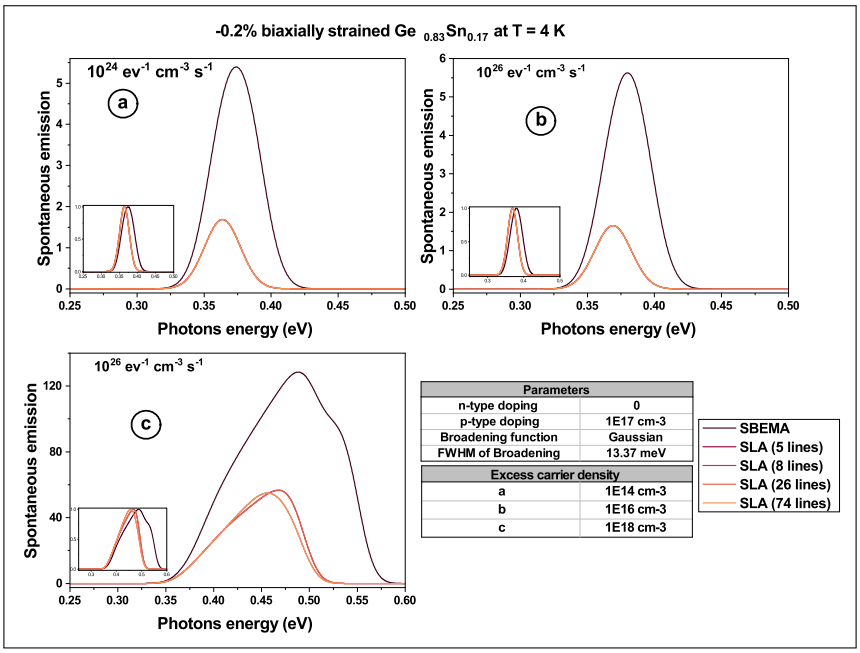

Figure 5.10 Comparison of the spontaneous emission spectra for the relaxed $Ge_{0.83}Sn_{0.17}$ at T = 4 K. Some of the parameters used during the computations are presented in the tables on the right

For both the as-grown and the relaxed $Ge_{0.83}Sn_{0.17}$ samples, the band offset $\Delta E_{\Gamma,L}$ between the Γ and the L valleys is large enough for the contribution of the L valley in the carrier dynamics to be neglected (-96.19 meV for the as-grown and -134.02 meV for the relaxed material at 4 K). Under optical injection, the increasing carrier concentration enables the electron quasi-Fermi level μ_e to move towards the Γ valley conduction band edge. From a specific value of the excess carrier concentration Δn, the energy difference between μ_e and the L valley conduction band edge would be small enough to allow the electrons to populate this valley (see equation (3.38)). The carrier dynamics in the L valley must therefore be considered when this value of Δn is reached. For $Ge_{0.83}Sn_{0.17}$, the impact of the L valley is

Table 5.3 – Values of the quasi-Fermi levels and the emission intensities at T = 4 K for the -1.27% biaxially strained $Ge_{0.83}Sn_{0.17}$. The values in the light cyan cells are the results from the eight-bands ***k.p*** formalism while the ones in white cells are from the single-band effective mass approximation

Δn (cm^{-3})	μ_e (meV)	μ_h (meV)	$R_{sp}(s^{-1} \cdot cm^{-3})$
10^{14}	450.0203	33.23982	6.37254×10^{22}
	450.1623	25.28013	1.2783×10^{23}
10^{16}	454.089	32.6444	6.4034×10^{24}
	455.127	24.1339	1.29151×10^{25}
10^{18}	527.2328	4.889568	6.69744×10^{26}
	551.6674	-44.36463	1.61928×10^{27}

perceptible when Δn is around $2 \times 10^{18}\text{cm}^{-3}$. At this value, the equations (3.41) and (3.42) are not solvable unless $n\Big|_{\mu_e}^{(L)}$ is explicitly computed through equation (3.38) instead of being set to zero.

5.1.5 Comparison between theoretical and experimental photoluminescence results

The luminescence properties of the samples were investigated using an FTIR-based PL setup with lock-in technique [61]. Power- and temperature-dependent PL were both performed. For accurate temperature control, the samples were mounted in a vertically oriented helium flow cryostat. The optical path of the PL emission was purged with nitrogen gas (N_2) to avoid water absorption lines being detected in the measured spectra. A germanium window was also used as a long-pass filter to remove the laser from the PL signal.

The power-dependent PL measurements were performed at 4 K for the as-grown sample, with the power density P_{exc} varying from 6.9 W/cm^2 to 5.4 kW/cm^2. Band to band emission was reported only for P_{exc} greater than 67.95 W/cm^2. Below this value, the PL emissions were considered to most likely come from free- and bound-exciton recombination [192–194]. For this reason, the fit of the experimental results starts from the 67.9545 W/cm^2 data. They are fitted with equation (3.1) using the eight bands ***k.p*** formalism and the unpolarized optical momentum matrix elements $(2M_{cv,TE}^2 + M_{cv,TM}^2)/3$. The fitting parameters in this process are the excess carrier concentration Δn and γ the FWHM of the broadening function $\mathcal{B}$. $\mathcal{B}$ is not fixed from the beginning of the process. Instead, it is chosen based on the resulting R-squared (R^2) factor of the fitting process. In fact, for a fixed value of P_{exc}, among the three functions mentioned in section 3.2, only the one resulting in the highest R^2 value is selected. It is, therefore, possible to have a different broadening function from one excitation power to another.

Figure 5.11 presents the results of the fitting process mentioned before. For each value of P_{exc}, an R^2 factor of around 99.5% is observed, expressing the goodness of the fit. The broadening function is found to be a Lorentzian for all the excitation power densities below 990.9 W/cm^2. Beyond this value, only the hyperbolic secant broadening function is observed. The broadening mechanisms are, therefore, homogeneous throughout the whole range of excitation power. Besides, for an excitation power density of 5.413 kW/cm^2, the emission tail between 0.43 eV and 0.45 eV is underestimated by the eight bands ***k.p*** spontaneous emission spectrum. This behavior is also observed with a Lorentzian broadening function (not shown). This tail could not be attributed to the ML layer because of its bandgap energy of ~ 0.53 eV at 4 K. It is most likely the result of some additional mechanisms uncaptured by our framework.

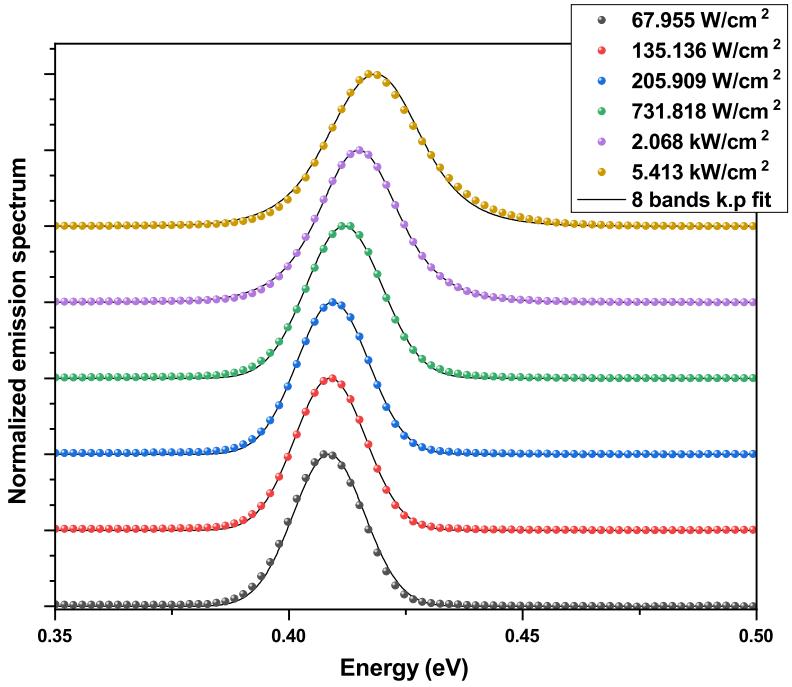

Figure 5.11 Power-dependent photoluminescence at T = 4 K for the -1.27% biaxially strained $Ge_{0.83}Sn_{0.17}$. The scatter points are from the measurements while the black lines are the results from the simulations

One strength of our theoretical framework is the ability to extract more physical parameters in addition to the bandgap energy. Figure 5.12 presents the variation of some of the extracted parameters as functions of the excitation power density. For a p-type background doping around 10^{17}cm^{-3}, the thermal equilibrium Fermi level E_F is about 33.25 meV. As shown in panel (a), the non-degenerate semiconductor approximation is not appropriate here since E_F is less than the valence band edge energy which, is around 42.93 meV. Starting from 67.9545 W/cm^2, both the electrons and holes quasi-Fermi levels start to deviate from E_F. Regarding the electrons quasi-Fermi level μ_e, a slightly progressive increase from 450.02 meV to 461 meV is observed. μ_e quickly goes above the conduction band edge energy (450.45 meV), causing the electron concentration to increase. On the other end, the holes quasi-Fermi level μ_h decreases while remaining very close to the thermal equilibrium level with a maximum offset of 2.76 meV at 5.4 kW/cm^2. While these variations may be perceived as small, they are not insignificant. Indeed, with the thermal energy of about 0.34 meV at 4 K, one should expect a noticeable increase in the spontaneous emission intensity R_{sp}.

Using equation (3.49) from section 3.4, the steady-state radiative carrier lifetime τ_{rad} is extracted as a function of P_{exc}. Panel (b) of figure 5.12 presents the extracted results. The observed behavior of τ_{rad} is the result of the evolution of both Δn and the net spontaneous

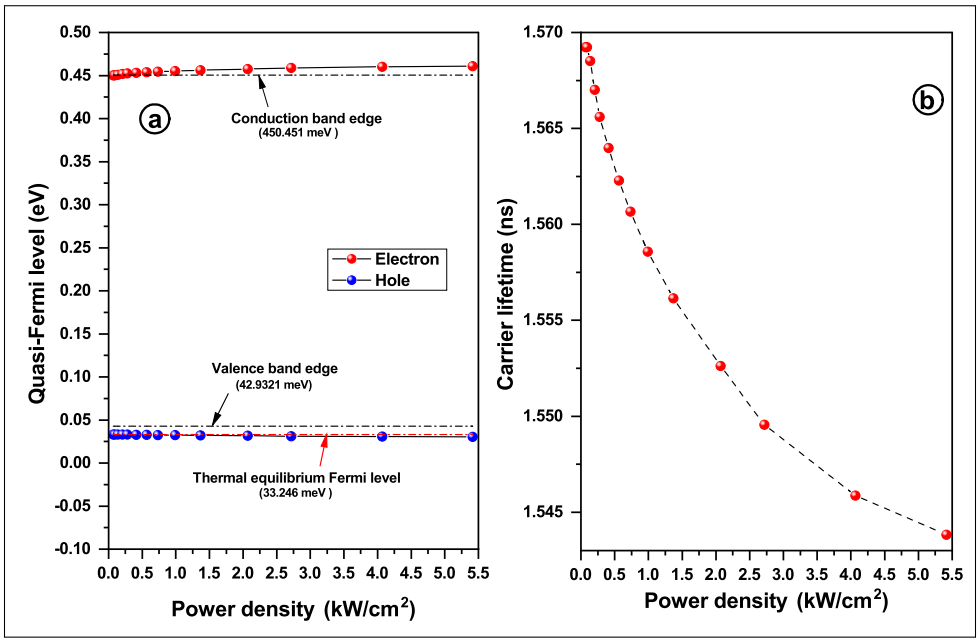

Figure 5.12 Extracted parameters from the fitting process of the 4 K power-dependent photoluminescence for the -1.27% biaxially strained $Ge_{0.83}Sn_{0.17}$.

emission intensity R_{sp}^{net} as functions of P_{exc}. Even though they are both increasing with P_{exc}, R_{sp}^{net} varies more significantly than Δn. Since the radiative carrier lifetime is inversely related to R_{sp}^{net}, its value decreases with a gradually raised excitation power density. An average value of 1.56 ns is extracted from these data. This value is within the same order of magnitude as that reported in cubic Ge [195].

Besides, equation (3.50) is also verified using the different parameters extracted from the fitting process. Indeed, the bimolecular recombination coefficient B is computed from the extracted values of R_{sp} and Δn and presented in figure 5.13. Rather than being constant, coefficient B decreases with Δn, as suggested in [133, 134]. However, the variation of the coefficient B in the as-grown $Ge_{0.83}Sn_{0.17}$ is not as linear as presented by Olshansky et al. for InGaAsP and AlGaAs light sources [135]. Using a polynomial fit, equation (5.4) is extracted with $B_0 = (6.366 \pm 0.003) \times 10^{-9}\,\text{cm}^3/\text{s}$, $B_1 = (-5.71 \pm 0.04) \times 10^{-26}\,\text{cm}^6/\text{s}$ and $B_2 = (3.27 \pm 0.09) \times 10^{-43}\,\text{cm}^9/\text{s}$. On top of that, the values extracted are two orders of magnitude lower than the value of $7.1972 \times 10^{-7}\,\text{cm}^3/\text{s}$ computed using equation (3.52) which assumes parabolic band dispersion and non-degenerate semiconductor.

$$B = B_0 + B_1\Delta n + B_2\Delta n^2 \tag{5.4}$$

Furthermore, a theoretical analysis is performed for the temperature-dependent PL. Using the bandgap energy extracted in [5], the behavior of the steady-state radiative carrier lifetime τ_{rad}

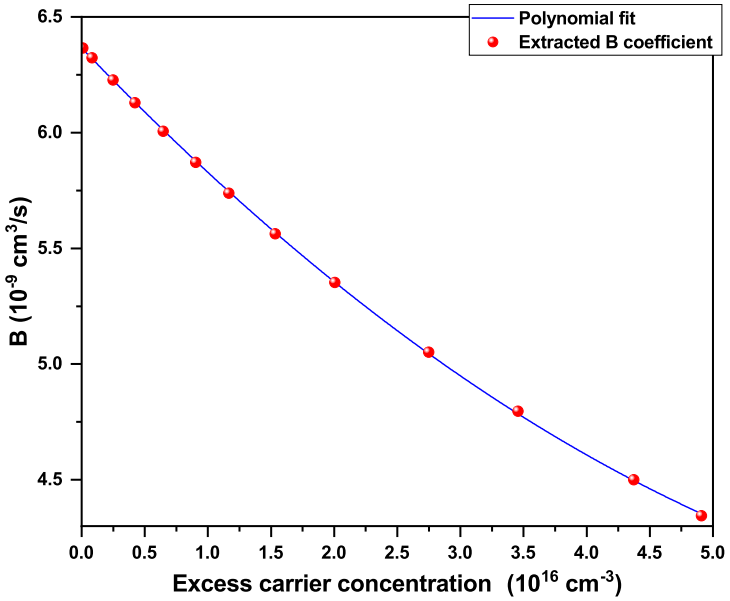

Figure 5.13 Extracted B coefficient from the fitting process of the 4 K power-dependent photoluminescence for the -1.27% biaxially strained $Ge_{0.83}Sn_{0.17}$.

is extracted for both the as-grown and the relaxed $Ge_{0.83}Sn_{0.17}$ samples and displayed in figure 5.14. In this figure, panel (a) highlights the results for the as-grown $Ge_{0.83}Sn_{0.17}$ material with a minimum R^2 factor of about 97% observed throughout the range 4-255 K. The results are somehow different for the relaxed $Ge_{0.83}Sn_{0.17}$. Indeed, as presented in panel (b), the fit accuracy decreases with the temperature. The differences between the experimental and theoretical data are more visible starting from T = 80 K. There are, even more pronounced above 220 K (not shown). They could be attributed to the noises observed in the experimental data but also to the uncertainties in material parameters. Indeed, with the sample patterned into microdisks, one would expect the material parameters to be different from those of thin films.

Figure 5.15 presents the evolution of the steady-state radiative carrier lifetime τ_{rad} with the temperature. Given the previous observations, the results in the principal figure are limited to the range 4-80 K while the inset plot goes up to 220 K. τ_{rad} evolves with the temperature following the power-law $a + bT^c$ for both the as-grown and the strain-relaxed materials. However, the evolution is much more pronounced for the strain-relaxed case with $c \approx 2.27$ (1.97 for the as-grown). This observation is somehow different from the $T^{3/2}$ power evolution observed in the low-injection regime.

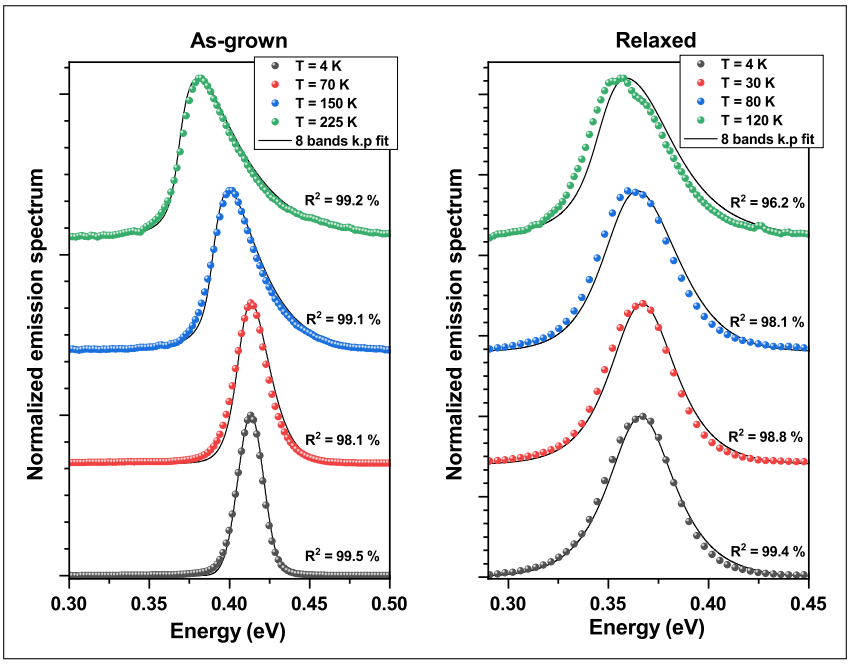

Figure 5.14 Some results of the fitting process of the temperature-dependent photoluminescence for both the as-grown and the relaxed $Ge_{0.83}Sn_{0.17}$.

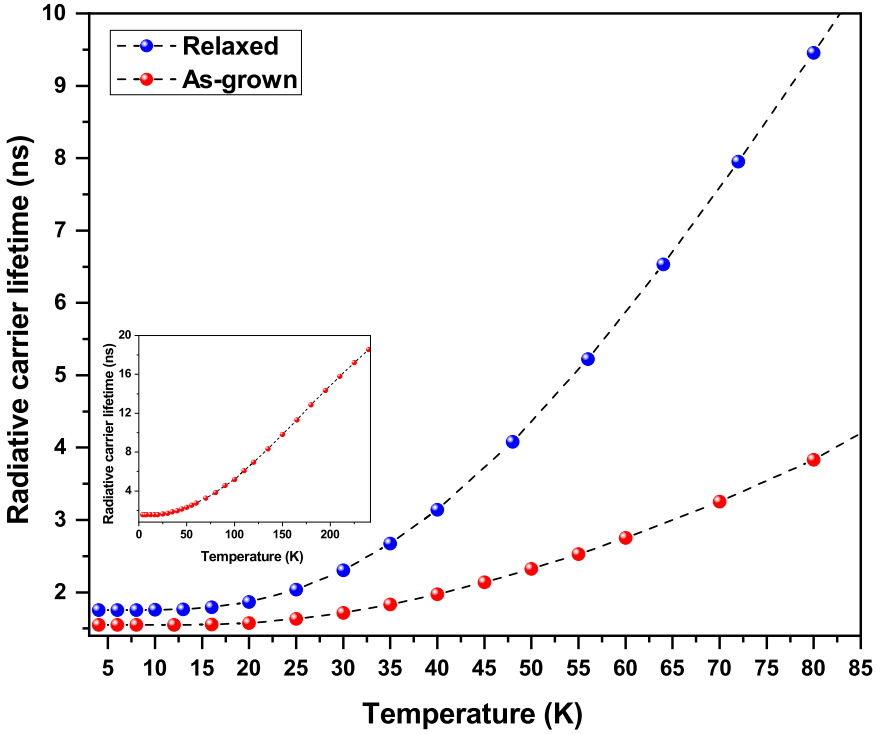

Figure 5.15 Extracted radiative carrier lifetime as function of temperature for both the as-grown and the relaxed $Ge_{0.83}Sn_{0.17}$.

Regarding the evolution of τ_{rad} with the lattice strain, a counterintuitive behavior is observed.

Indeed, with the decrease of the bandgap resulting from the relaxation of the material, one would expect the carriers to recombine more rapidly, and therefore τ_{rad} to decrease. However, the radiative lifetime is shown to be higher for the relaxed $Ge_{0.83}Sn_{0.17}$. The most obvious explanation would be the emission degradation by the surface roughness and the etching steps, but all these concepts are not explicitly included in our framework. It is therefore very unlikely to be able to perceive their impact with this model. Besides this explanation, one could also look for the impact of the effective masses on the radiative carrier lifetime. The effective masses of the as-grown material are estimated to be greater than those of the strain-relaxed $Ge_{0.83}Sn_{0.17}$. This behavior is observed throughout the 4-300 K temperature range. In that case, the carrier mobility should be higher in the strain-relaxed material. The carriers should therefore drift faster and slowly recombine radiatively in the strain-relaxed material. This explanation is only speculation, and more investigation should be done to understand better the evolution of τ_{rad} with the lattice strain in this GeSn material.

5.2 Fabrication and characterization of GeSn DH based LEDs

GeSn-based light emitters have been attracting a great deal of interest in recent years because of their relevance for biomedical and gas sensing applications [196, 197]. LEDs with $Ge_{1-x}Sn_x$ alloys as active materials have been investigated in the literature based predominantly on theoretical studies. Approaches using GeSn *p-n* and GeSn/Ge *p-i-n* heterostructures with Sn composition up to 12 at.% resulted in increased emissions compared to Ge diodes. EL from GeSn/SiGeSn MQWs based LEDs were also demonstrated [82, 83]. These MQW-based devices were reported to have a better efficiency compared to homojunction devices. However, their efficiency at room temperature is still low compared to that of bulk GeSn LEDs with higher Sn content. In this section, the fabrication and characterization of GeSn DH based LEDs are discussed.

5.2.1 Growth and characterization of *p-i-n* GeSn sample

The GeSn multilayer heterostructures (panel (a) of figure 5.16) used for the LED processing were grown on a 4-in. Si (100) wafer in an LP-CVD reactor [61, 69, 159, 198]. Ultrapure H_2 was used as a carrier gas, while 10% monogermane diluted in H_2 (GeH_4) and tin-tetrachloride ($SnCl_4$) were employed as gas precursors. First, a 600–700 nm-thick Ge-VS was grown at 450°C, followed by thermal cyclic annealing (> 800°C) and additional Ge deposition. To ensure uniform composition and avoid Sn segregation in the utmost *p-i-n* stacking, the composition of each $Ge_{1-x}Sn_x$ layer was controlled by the growth temperature [198]. The temperature was decreased from 335°C to 305°C to increase the Sn content from ~ 4 at.% (#1)

to 8.3 at.% (i-layer). Diborane (B_2H_6) and arsine (AsH_3) were used as precursors for doping the 4.3 at. % p (335°C) and 5.0 at. % n (345°C) layers, respectively. Two thin, heavily doped n-layers were grown on top of the p-i-n stacking to further decrease the contact resistance of the final device and enhance the performance [199]. The thicknesses of different layers are listed in table 5.4. The composition and strain in each layer were extracted from RSM around the (224) asymmetrical XRD peak in figure 5.16b. A small compressive strain lower than -0.3% was estimated for all layers, except for the n-layer, where a small tensile strain (0.3%) was observed. This result originates from the lower Sn content in the n layer as compared to the fully-relaxed i-layer.

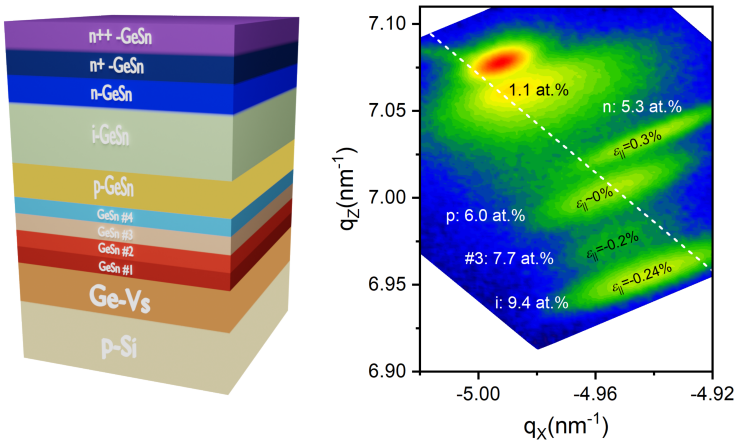

Figure 5.16 (a) Schematic illustration of the p-i-n heterostructure with $Ge_{0.906}Sn_{0.094}$ as i-layer. (b) XRD-RSM around the asymmetrical (224) reflection of the same sample. The materials growth in addition to the XRD-RSM data acquisition were performed by Simone Assali.

Table 5.4 – Thicknesses of the $Ge_{1-x}Sn_x$ p-i-n layers and the heavily-doped n-type doped layers

Material	Thickness (nm)
p-layer	291
i-layer	795
n-layer	327
n^+ layer	6
n^{++} layer	30

5.2.2 Fabrication of GeSn-based light emitting diodes

The light-emitting devices were fabricated following a Corbino geometry. For the sake of simplification, the four GeSn layers underneath the p-doped layer are grouped into one layer in the illustration presented in figure 5.17a. The sample was firstly cleaned with solvents

and later patterned by photolithography with a spin-coated positive photoresist. The mesa structure was etched from the top n layers down to the Ge-VS in an ICP-RIE system with a gas combination of $Cl_2/Ar/O_2$. Subsequently, the photoresist was stripped using acetone and isopropyl alcohol (IPA). Then, another photolithography step was performed, followed by an etching process in an ICP RIE system down to the p-GeSn, which serves as the bottom contact layer. Following these steps, a SiO_2 passivation layer was deposited, by plasma-enhanced chemical vapor deposition (PECVD), for electrical isolation of the sample. Thereafter, the passivation layer was patterned using photolithography and later etched in a Buffered Oxide Etch (BOE) solution to define the electrical contact windows. An E-beam metal deposition process was later performed as the last step with 10nm/100nm/100nm/800nm of Ti/Au/Ti/Au to form the p and n contacts. Figure 5.17 presents a summary of the overall process, and a top view image of the fabricated device is depicted in figure 5.18. The devices have varying diameters in the 20-160 µm range.

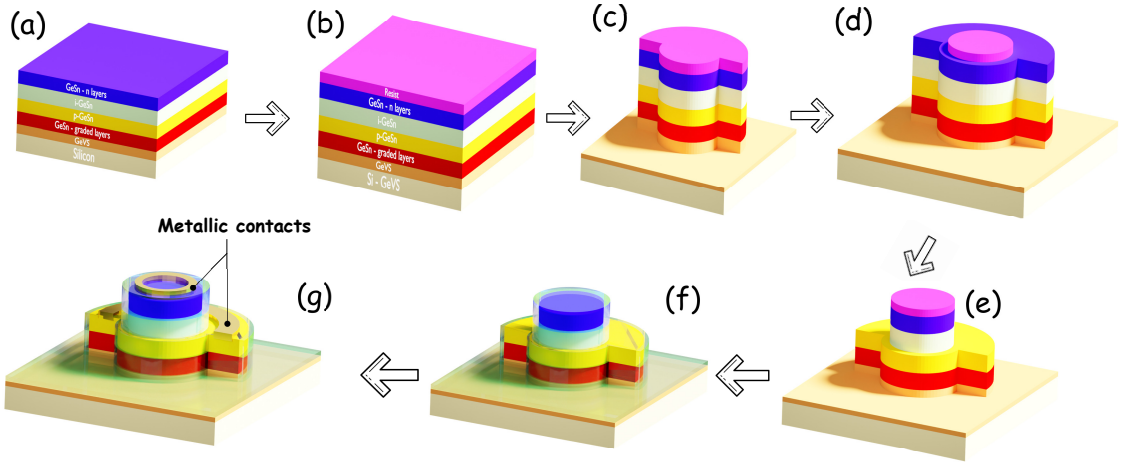

Figure 5.17 Process flow for the microfabrication of the GeSn-based light-emitting device. (a) Initial sample from figure 5.16a modified to reduce the number of layers. (b)&(c) Mesa patterning and etching after application of resist. (d)&(e) p-layer patterning and etching of the mesa until the p-layer is reached. (f) SiO_2 deposition and etching. (g) Metal deposition. The devices were fabricated by Mahmoud Attala.

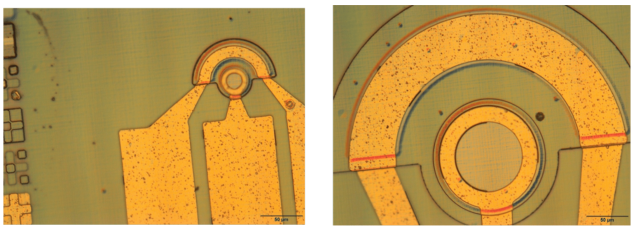

Figure 5.18 Top view image of the device seen through a microscope.

5.2.3 Characterization of GeSn-based light emitting diodes

The device performance was investigated by examining first the current-voltage (I-V) characteristics of the devices under dark conditions at 300 K. These measurements were performed using a Keithley 4200a parameter analyzer connected to a probe station, and the results are presented in panel (a) of figure 5.19. In reverse bias, an increase of the current with the diameter is observed. This behavior is expected since the growth defects become more significant for larger devices. The results also suggest a breakdown to be reached at just 11 V for the 40 µm diameter device.

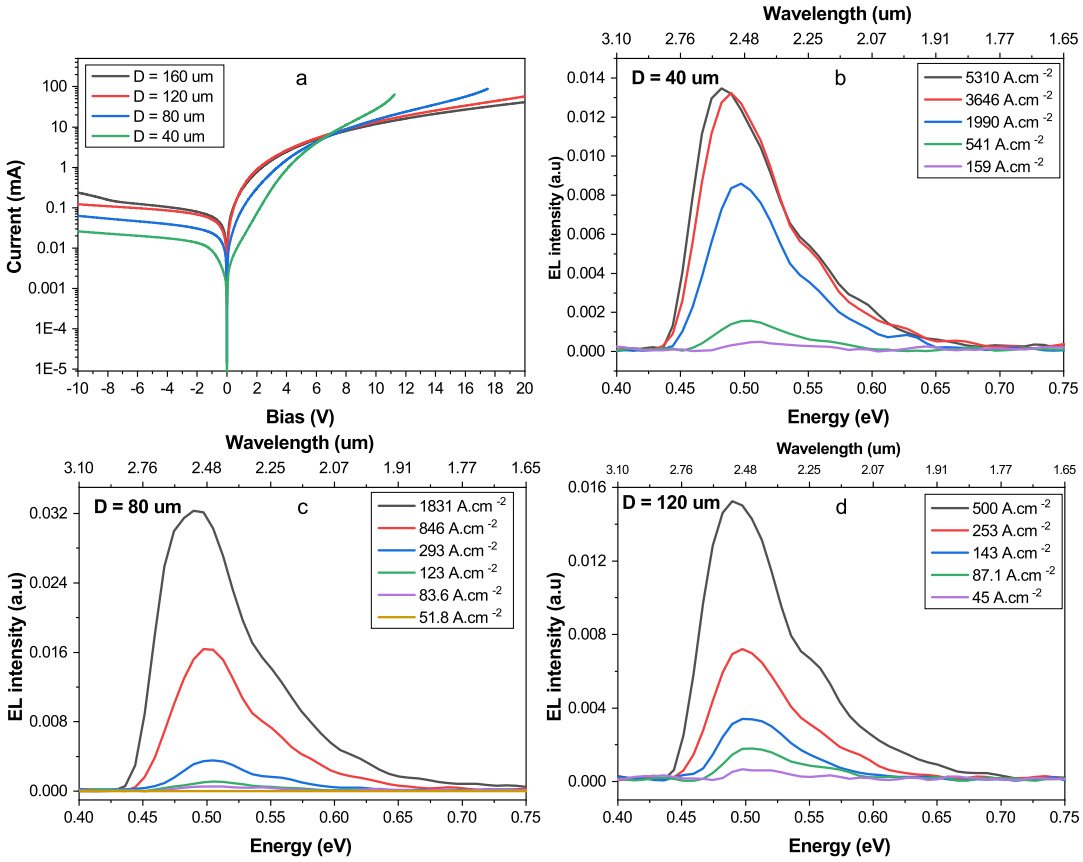

Figure 5.19 GeSn *p-i-n* LED. (a) I-V for dark current for various devices diameters. (b-d) Power dependent EL spectra for 40 µm(b), 80 µm (c), and 120 µm (d) device diameter. These data were acquired by Mahmoud Attala.

The panels (b), (c), and (d) of figure 5.19 show the power dependence of the light emission collected at 300 K for the 40 µm, 80 µm, and 120 µm diameter devices, respectively. These data were recorded using an FTIR-based EL setup with a lock-in technique. A clear emission peak is observed close to 2.48 µm at a current density as low as 45 A/cm^2. This observation is quite similar to PL emission reported for $Ge_{0.895}Sn_{0.105}$ materials, with an in-plane compressive

strain of $-0.4\,\%$ [86]. It should most likely come from the direct-band gap $Ge_{0.906}Sn_{0.094}$ *i*-layer. Moreover, a shoulder is observed around 0.54 eV over the entire range of current densities. Its origin will be investigated later in the document using PL measurements.

Besides, as expected, the EL intensities increase with the current densities. The emission peaks also shift to slightly longer wavelengths as the current density increases. For instance, at the current density of $500\,A/cm^2$, the EL peak red-shift and reaches $\sim 2.53\,\mu m$ in the $120\,\mu m$ LED. These red-shifts of the emission peaks could be the results of Joule heating of the devices, but more studies would be needed to confirm this hypothesis.

To further study the band-to-band transitions in the GeSn DH, temperature-dependent PL measurements were carried out. The results are summarized in figure 5.20.

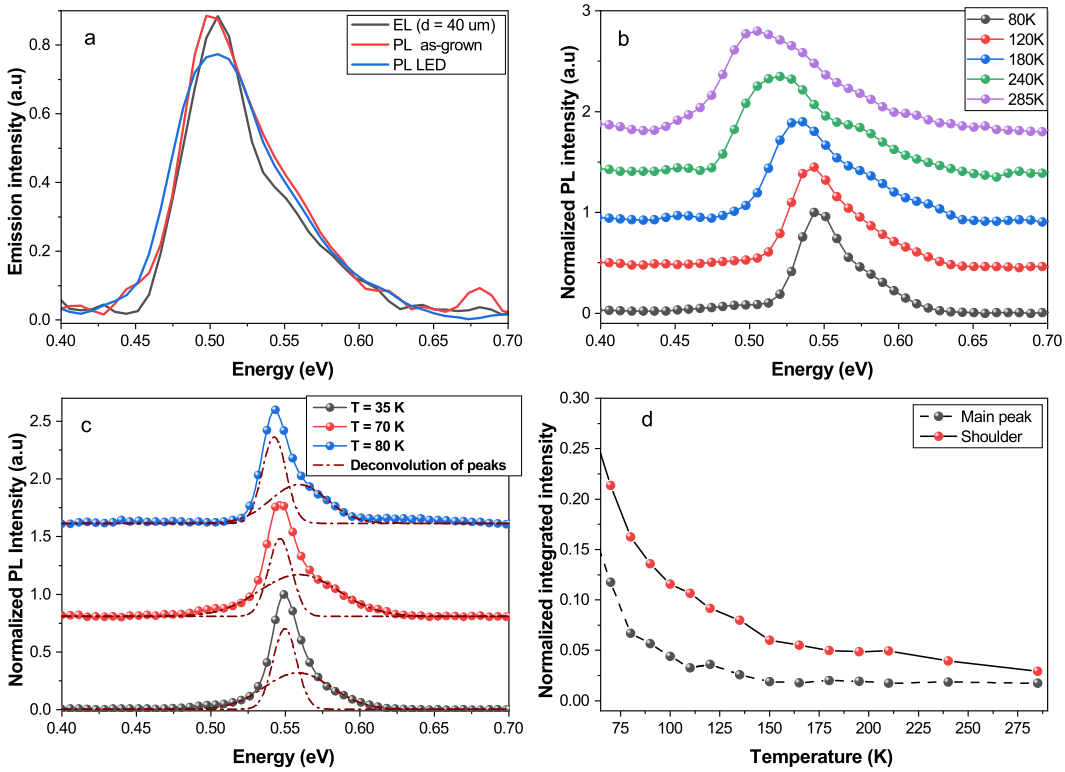

Figure 5.20 Photoluminescence measurements of GeSn *p-i-n* DH. (a) Comparison of the EL spectrum ($d = 40\,\mu m$, $846\,A/cm^2$) with the PL spectra from both the as-grown sample and the LED. (b) Temperature-dependent PL spectra for the as-grown sample. (c) Deconvolution of the emission peaks at different temperatures. (d) Integrated intensity as a function of the temperature.
The data from panel (a) were acquired by Mahmoud Attala.

Panel (a) shows the PL spectra at 300 K of both the as-grown sample and the LED. These spectra are superimposed to the EL spectrum of the $40\,\mu m$ diameter device. The peaks of

the PL and EL spectra coincide with each other. This observation confirms that the EL peak is intrinsic to material properties and not affected by the device fabrication process. The shoulder is also observed in the PL spectra, even though less pronounced. At this point, different ideas could be proposed to explain its origin. For instance, the slight difference between the position of the peaks may suggest the shoulder to be the result of the transitions from the Γ valley conduction band to the light holes valence band. The L valley conduction band could also be part of the equation. Additionally, the contributions from the other layers should not be excluded since the carriers could leak to them in case of smaller band-offsets.

Panel (b) displays the PL spectra for various temperatures ranging from 80 K to 285 K. In this figure, the dominant emission peak and the shoulder can be observed. Both peaks blue-shift as the temperature decreases even though the evolution of the shoulder position is not so visible. This variation is further highlighted in panel (c). Indeed, this figure displays the results of the peak deconvolution process at different temperatures. At each temperature, the spectrum was decomposed into two Gaussian spectra related to the 2.5um emission and the shoulder, respectively. This qualitative analysis was performed to mainly analyze the evolution of the integrated PL intensities as a function of the temperature. As depicted in panel (d) of figure 5.20, the integrated intensity related to the 2.5 µm emission spectrum decrease with increasing temperature. This observation is an indication that the emission is coming from the direct-band gap $Ge_{0.906}Sn_{0.094}$ i-layer [200]. The same behavior is also observed for the shoulder. Nonetheless, it is still not enough to establish its origin. Indeed, if the contribution from the $Ge_{0.906}Sn_{0.094}$ L valley is excluded, the possible involvement of the other layers remains to be elucidated.

With the eight-bands ***k.p*** formalism and the material parameters from table 3.1, the $Ge_{0.906}Sn_{0.094}$ i-layer is expected to have a direct bandgap of 530.82 meV at 300 K. This value is higher than the peak positions observed in both the PL and EL spectra. It is the opposite of what is expected from band-to-band spontaneous emission recombination. Therefore, the bandgap energy is overestimated. This overestimation is not surprising since the bandgap bowing parameter b_G has been reported to depend on the lattice strain, the Sn composition in addition to temperature [36, 201–203]. Regarding the eight-bands ***k.p*** fitting process presented in the previous chapters, it is tricky to add E_G as a fitting parameter besides the excess carrier concentration Δn and γ the FWHM of the broadening function. Indeed, E_G is implicitly linked to the injected carrier concentration Δn and, therefore, to the quasi-Fermi levels μ_e and μ_h. Given this link, a value of E_G close to the emission peak position would minimize the value of Δn ($10^{14}\,cm^{-3}$, for example) and force the non-degenerate semiconductor approximation regardless of the value of the background doping. On the other hand, when E_G is relatively far from the peak position, Δn is adjusted to compensate for the

energy difference through the values of the quasi-Fermi levels. One could use equation (3.11) in chapter 3 to fit the emission spectrum and extract E_G. However, if this method can be used as a first approximation, the background doping in the i-layer might be a problem since it could invalidate the non-degenerate semiconductor approximation required in the equation (3.10).

To evaluate the accuracy of the eventual non-degenerate semiconductor approximation, let us assume the background doping to be $10^{16}\,\mathrm{cm}^{-3}$, which is in line with what has been measured and reported for similar materials (mid-$10^{16}\,\mathrm{cm}^{-3}$ to mid-$10^{17}\,\mathrm{cm}^{-3}$) [86]. With this value, the energy difference between the band edge (CB or VB) and the Fermi levels (μ_e, μ_h) is estimated for different values of Δn by varying the bandgap E_G from 0.45 eV to 0.5 eV. Figure 5.21 presents the results of this analysis. At thermal equilibrium ($\Delta n = 0$), both $(E_c - \mu_e)/k_BT$ and $(\mu_h - E_v)/k_BT$ are above 4. In that case, the $Ge_{0.906}Sn_{0.094}$ i-layer is a non-degenerately doped semiconductor, based on the comparison presented in figure 3.1. This layer remains non-degenerate until the excess carrier density becomes comparable to the doping density N_A. In fact, for $\Delta n \geq 10^{16}\,\mathrm{cm}^{-3}$, at least one of the energy differences is below 4. In this case, the Boltzmann distribution cannot replace the Fermi-Dirac distribution, and the non-degenerate semiconductor approximation is not valid anymore. If the excess carrier concentration is assumed to be small enough for the non-degenerate semiconductor approximation to be fulfilled, the bandgap of the i-layer should be around 479.21 meV.

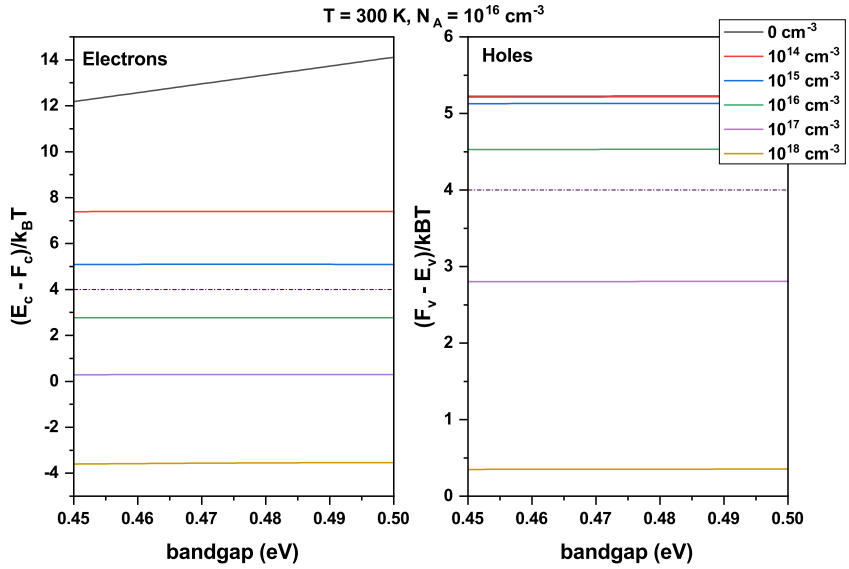

Figure 5.21 Evaluation of the accuracy of the non-degenerate semiconductor approximation for different values of the excess carrier concentration Δn. F_c and F_v are nothing more than the quasi-Fermi levels μ_e and μ_h, respectively. E_c is the bottom edge of the conduction band, and E_v the top edge of the valence band.

This chapter presented the different parameters extracted from the PL analysis of the TL/ML/BL heterostructure using the theoretical framework developed in chapter 3. From the quasi-Fermi levels to the steady-state radiative carrier lifetime, the framework was proved to be accurate to fit the experimental results and explain some physical behaviors of the carriers inside the GeSn material. Besides, its accuracy was also assessed by going through different comparisons with the SBEMA and the JDOS model at each step of the computations. The multi-bands $\boldsymbol{k.p}$ formalism was proved to be essential for more general study with a restrictive number of approximations. Furthermore, the evolutions of both the envelope functions and the momentum matrices with $\vec{\boldsymbol{k}}$ are relevant for a more accurate estimation of the absorption and emission spectrum.

In addition to the $Ge_{0.83}Sn_{0.17}$ material, GeSn DH based LEDs were demonstrated and discussed. The analyses presented in section 5.2 were performed to explain the different features observed in the luminescence spectra of both the planar *p-i-n* sample and the fabricated LED. At room temperature, a clear EL emission peak at around 2.5 µm was observed. This emission was also noticeable for current density as low as 45 A/cm^2 for the 120 µm diameter device. The power-dependence analysis of the light emission highlighted a possible Joule heating of the devices. Besides, the appearance of the shoulder at ~ 0.54 eV in the spectra was investigated using temperature-dependent PL. However, no concrete explanation was found. In the end, more investigations should be done to understand the origin of this shoulder along with the device's performance and efficiency.

CHAPTER 6 CONCLUSION AND PERSPECTIVES

In the scope of this thesis, $Ge_{1-x}Sn_x$ alloys were investigated for the development of Si-integrated mid-infrared emitters. The fabrication of these devices requires the availability of high-quality materials in addition to accurate estimations of their optical and electrical properties. To that end, rigorous theoretical models and simulations must be established. The first task of the thesis has been the implementation of a theoretical framework to study the fundamental physics underlying the GeSn absorption and luminescence properties. This task involved the evaluation of the spontaneous emission, absorption, and optical gain spectra. In chapter 3, we detailed each step of the methodology used for our framework while establishing a comparison with the SBEMA usually used in literature. In this vein, we presented an explicit evaluation of the momentum matrix elements for a (001) oriented material. This approach should offer more flexibility in the computation of the intravalence band absorption in addition to the spontaneous emission intensity. It could also be easily generalized to different crystallographic orientations with some additional mathematical tips. We also found that the strain value impacts the computation of the integrals over the BZ, and therefore, the evaluation of the quasi-Fermi levels as well as the emission and absorption spectrum. In that case, a trade-off is made between computation time and accuracy.

The accuracy of our framework was assessed in chapter 5 by analyzing the PL emission spectra of a $Ge_{0.83}Sn_{0.17}$ material. For this purpose, the band structures resulting from the SBEMA and the eight bands $\boldsymbol{k.p}$ formalism were compared. As expected, there was a relatively small region of the first BZ where a perfect match was observed. Regarding the differences, we found them to be more pronounced for the valence bands and dependent on the strain value in addition to the temperature. Furthermore, their impacts have been directly observed in the calculation of the charge carrier densities. They were even more visible when the quasi-Fermi levels were located inside the bands. The number of "special" directions needed for computing the integrals over the BZ was found to go from seventy-four to eight for this specific material. Indeed, multiple directions were found to be degenerate for the values of strain used in this study. The impact of Kane's Y stars on the whole computation process has also been shown to be negligible for this material. Besides, the optical strengths of the transitions have been shown to vary with the wave vector $\vec{\boldsymbol{k}}$. These variations result from the evolution of momentum matrix elements $M_l^{\mu\nu}$ and the envelope functions, both with $\vec{\boldsymbol{k}}$. We also found them to depend on the polarization of the incident electromagnetic field and the direction of the wave vector $\vec{\boldsymbol{k}}$. This result is different from the isotropy usually claimed for these quantities in bulk semiconductors. We, therefore, think that the variation

of the envelope functions should be considered to study the luminescence and the absorption properties of $Ge_{1-x}Sn_x$ alloys.

By bringing all these observations together, we succeeded in accurately fitting both the power- and temperature-dependent PL data for the as-grown $Ge_{0.83}Sn_{0.17}$ sample. From these analyses, a steady-state radiative carrier lifetime τ_{rad} in the ns range was extracted. This quantity was shown to decrease with the excitation power, and an average value of ~ 1.56 ns was extracted at 4 K. Moreover, the increase of τ_{rad} with temperature was reported. In fact, from a value of ~ 1.5 ns at 4 K, τ_{rad} was estimated at ~ 3.5 ns at 80 K in the as-grown $Ge_{0.83}Sn_{0.17}$. As for the relaxed sample, higher values were reported over the range 4-80 K with a value of ~ 9.5 ns at 80 K. An accurate interpretation of this behavior would require more investigations.

After studying the PL from the $Ge_{0.83}Sn_{0.17}$ samples, LEDs were fabricated from GeSn *p-i-n* DH with an *i*-layer of 9.4 at.% Sn. EL emission at ~ 2.5 µm at 300 K was demonstrated. This emission was shown to be the result of the carrier recombination inside the $Ge_{0.906}Sn_{0.094}$ direct bandgap *i*-layer. Additionally, a shoulder has been observed around 0.54 eV in both the EL and the PL spectra. By analyzing its evolution with the temperature, we succeeded in excluding the transitions involving the L valley as a possible origin of this feature. However, more investigation would be required for an effective description of this shoulder.

As summarized above, compared to the SBEMA/JDOS formalism, our theoretical framework allows for a more accurate description of the optical properties of single bulk GeSn materials. However, there are still some limitations that need to be addressed. The theoretical framework was initially supposed to describe both QW and bulk systems, with the key objective of finding the optimal Sn and Si compositions required to enhance the efficiencies of (Si)GeSn-based light emitters. For that purpose, in a study not detailed in this thesis, we investigated the thresholdless coaxial nanolaser structure presented in [204] by replacing the InGaAsP QW with (Si)GeSn QW. Our goal was to highlight the impact of Si/Sn compositions and the strain on the efficiency of the nanolaser by computing the absorption and spontaneous emission spectra for different values of Sn and Si compositions. This task was found to be inaccurate with the (Si)GeSn material parameters currently available. Indeed, due to the lack of compelling and systematic experimental studies, one has to rely on the non-optimized material parameters presented in the literature. The bandgap bowing parameter b_G^{GeSn} is, for example, an important parameter for the estimation of the bandgap energy. Usually assumed to be constant, this parameter has been shown to vary with the Sn content, the temperature, and the strain in the material [36, 201–203]. Given this information, we found it wise to investigate the impact of the lattice strain and Sn composition on the optical properties of

$Ge_{1-x}Sn_x$ materials with more or less optimized parameters. It should be noted that the constraint imposed by the material parameters limited our framework to the description of single bulk materials, for instance, the top layer of a sample in an experiment or a wide enough intrinsic layer of a DH as suggested in theory studies by Sun et al. and also Chuang [88, 205]. That being said, the investigation of $Ge_{0.83}Sn_{0.17}$ homojunction should be possible even though some additional parameters would be required (diffusion coefficient and mobility, for instance).

The effective carrier lifetime τ is the quantity usually reported in the literature. It is defined by equation (6.1), with τ_{Auger} and τ_{SRH} being the lifetimes associated with Auger and SRH recombination, respectively.

$$\tau = \left(\frac{1}{\tau_{\text{rad}}} + \frac{1}{\tau_{\text{Auger}}} + \frac{1}{\tau_{\text{SRH}}} \right)^{-1} \tag{6.1}$$

As mentioned in section 3.5, we were not able to include the description of the non-radiative recombination mechanisms in our framework. The reasons for that were the limitations of the eight-bands ***k.p*** and the lack of compelling experimental data. Future research directions should focus, for example, on the description of the Auger recombination mechanism using Green's function theory [206–208]. A similar approach was reported in the literature for unstrained $Ge_{0.91}Sn_{0.09}$ and $Ge_{0.82}Sn_{0.18}$ materials [209]. In that study, the $Ge_{1-x}Sn_x$ full electronic bandstructure was determined through an empirical pseudopotential method. In our case, we could rely on the thirty bands ***k.p*** formalism already developed in the group. This formalism could also be used to improve the accuracy of the theoretical framework developed throughout this work. As for the SRH recombination mechanism, an accurate theoretical description would require prior knowledge of the density of trapping centers and the capture cross-sections of the $Ge_{1-x}Sn_x$ material system.

Regarding the LEDs, the next obvious step would be to perform thorough optical and electrical characterization. The main goal of these analyses would be to assess their efficiency and clarify the different observations made in chapter 5. For instance, the devices could be operated using a modulated rectangular voltage rather than a DC voltage to investigate the impact of Joule heating [83, 210]. As for the shoulder in the emission spectra, PL measurements could be performed using different excitation lasers to study the possible contribution from the different layers of the samples. Compared to the 532 nm laser, a laser with a wavelength of either 976 or 1550 nm should have reasonable penetration depths for that purpose.

REFERENCES

[1] P. Moontragoon, Z. Ikonić, and P. Harrison, "Band structure calculations of Si–Ge–Sn alloys: Achieving direct band gap materials," *Semiconductor Science and Technology*, vol. 22, no. 7, pp. 742–748, 2007.

[2] K. Lu Low *et al.*, "Electronic band structure and effective mass parameters of $Ge_{1-x}Sn_x$ alloys," *Journal of Applied Physics*, vol. 112, no. 10, p. 103715, 2012.

[3] E. F. Schubert, *Light-Emitting Diodes*, 2nd ed. Cambridge University Press, 2006.

[4] N. K. Dutta and R. J. Nelson, "The case for Auger recombination in In1-xGaxAs yP1-y," *Journal of Applied Physics*, vol. 53, no. 1, pp. 74–92, 1982.

[5] S. Assali *et al.*, "Midinfrared Emission and Absorption in Strained and Relaxed Direct-Band-Gap Ge 1 - x Sn x Semiconductors," *Physical Review Applied*, vol. 15, no. 2, p. 024031, 2021.

[6] David Reinsel, John Gantz, John Rydning, "Data age 2025 : The digitization of the world from edge to core," https://www.seagate.com/files/www-content/our-story/trends/files/idc-seagate-dataage-whitepaper.pdf, 2018, [Online].

[7] R. Hintemann, "Data centers 2018. Efficiency gains are not enough: Data center energy consumption continues to rise significantly - Cloud computing boosts growth," 2020.

[8] E. Masanet *et al.*, "Recalibrating global data center energy-use estimates," *Science*, vol. 367, no. 6481, pp. 984–986, 2020.

[9] G. P. Agrawal, "Optical Communication: Its History and Recent Progress," in *Optics in Our Time*, M. D. Al-Amri, M. El-Gomati, and M. S. Zubairy, Eds. Cham: Springer International Publishing, 2016, pp. 177–199.

[10] D. Miller, "Rationale and challenges for optical interconnects to electronic chips," *Proceedings of the IEEE*, vol. 88, no. 6, pp. 728–749, 2000.

[11] D. Thomson *et al.*, "Roadmap on silicon photonics," *Journal of Optics*, vol. 18, no. 7, p. 073003, 2016.

[12] N. Dupuis *et al.*, "30-Gb/s Optical Link Combining Heterogeneously Integrated III–V/Si Photonics With 32-nm CMOS Circuits," *Journal of Lightwave Technology*, vol. 33, no. 3, pp. 657–662, 2015.

[13] M. J. R. Heck *et al.*, "Hybrid Silicon Photonic Integrated Circuit Technology," *IEEE Journal of Selected Topics in Quantum Electronics*, vol. 19, no. 4, pp. 6 100 117–6 100 117, 2013.

[14] N. Izhaky *et al.*, "Development of CMOS-Compatible Integrated Silicon Photonics Devices," *IEEE Journal of Selected Topics in Quantum Electronics*, vol. 12, no. 6, pp. 1688–1698, 2006.

[15] S. Keyvaninia *et al.*, "Heterogeneously integrated III-V/silicon distributed feedback lasers," *Optics Letters*, vol. 38, no. 24, p. 5434, 2013.

[16] D. Liang and J. E. Bowers, "Recent progress in lasers on silicon," *Nature Photonics*, vol. 4, no. 8, pp. 511–517, 2010.

[17] D. Tsiokos and G. Kanellos, "Optical interconnects," in *Optical Interconnects for Data Centers*. Elsevier, 2017, pp. 43–73.

[18] R. Soref, D. Buca, and S.-Q. Yu, "Group IV Photonics: Driving Integrated Optoelectronics," *Optics and Photonics News*, vol. 27, no. 1, p. 32, 2016.

[19] J. Liu, L. C. Kimerling, and J. Michel, "Monolithic Ge-on-Si lasers for large-scale electronic–photonic integration," *Semiconductor Science and Technology*, vol. 27, no. 9, p. 094006, 2012.

[20] M. El Kurdi *et al.*, "Band structure and optical gain of tensile-strained germanium based on a 30 band k.p formalism," *Journal of Applied Physics*, vol. 107, no. 1, p. 013710, 2021.

[21] R. E. Camacho-Aguilera *et al.*, "An electrically pumped germanium laser," *Optics Express*, vol. 20, no. 10, p. 11316, 2012.

[22] J. Liu *et al.*, "Ge-on-Si laser operating at room temperature," *Optics Letters*, vol. 35, no. 5, p. 679, 2010.

[23] ——, "Tensile-strained, n-type Ge as a gain medium for monolithic laser integration on Si," *Optics Express*, vol. 15, no. 18, p. 11272, 2007.

[24] X. Sun *et al.*, "Room-temperature direct bandgap electroluminesence from Ge-on-Si light-emitting diodes," *Optics Letters*, vol. 34, no. 8, p. 1198, 2009.

[25] R. Koerner *et al.*, "Electrically pumped lasing from Ge Fabry-Perot resonators on Si," *Optics Express*, vol. 23, no. 11, p. 14815, 2015.

[26] Y. Lin *et al.*, "Germanium Photodetector with Enhanced Photo-Response at the L-Band and Beyond for Integrated Photonic Applications," in *2018 IEEE 15th International Conference on Group IV Photonics (GFP)*. Cancun: IEEE, Aug. 2018, pp. 1–2.

[27] R. A. Soref, F. De Leonardis, and V. M. N. Passaro, "On-Chip Detection of Trace Gases Using Photonic Matched Filters," *Journal of Lightwave Technology*, vol. 37, no. 4, pp. 1388–1395, 2019.

[28] C. Goodman, "Direct-gap group IV semiconductors based on tin," *IEE Proceedings I Solid State and Electron Devices*, vol. 129, no. 5, p. 189, 1982.

[29] R. W. Olesinski and G. J. Abbaschian, "The Ge-Sn (Germanium-Tin) system," *Bulletin of Alloy Phase Diagrams*, vol. 5, no. 3, pp. 265–271, 1984.

[30] J. Doherty *et al.*, "Progress on Germanium–Tin Nanoscale Alloys," *Chemistry of Materials*, vol. 32, no. 11, pp. 4383–4408, 2020.

[31] S. Wirths *et al.*, "Lasing in direct-bandgap GeSn alloy grown on Si," *Nature Photonics*, vol. 9, no. 2, pp. 88–92, 2015.

[32] D. Stange *et al.*, "Study of GeSn based heterostructures: Towards optimized group IV MQW LEDs," *Optics Express*, vol. 24, no. 2, p. 1358, 2016.

[33] D. W. Jenkins and J. D. Dow, "Electronic properties of metastable $Ge_{1-x}Sn_x$ alloys," *Physical Review B*, vol. 36, no. 15, pp. 7994–8000, 1987.

[34] K. Mäder, A. Baldereschi, and H. von Känel, "Band structure and instability of $Ge_{1-x}Sn_x$ alloys," *Solid State Communications*, vol. 69, no. 12, pp. 1123–1126, 1989.

[35] S. Gupta *et al.*, "Achieving direct band gap in germanium through integration of Sn alloying and external strain," *Journal of Applied Physics*, vol. 113, no. 7, p. 073707, 2013.

[36] W.-J. Yin, X.-G. Gong, and S.-H. Wei, "Origin of the unusually large band-gap bowing and the breakdown of the band-edge distribution rule in the Sn_xGe_{1-x} alloys," *Physical Review B*, vol. 78, no. 16, p. 161203, 2008.

[37] C. Eckhardt, K. Hummer, and G. Kresse, "Indirect-to-direct gap transition in strained and unstrained Sn_xGe_{1-x} alloys," *Physical Review B*, vol. 89, no. 16, p. 165201, 2014.

[38] H. P. Ladrón de Guevara *et al.*, "Determination of the optical energy gap of $Ge_{1-x}Sn_x$ alloys with $0 < x < 0.14$," *Applied Physics Letters*, vol. 84, no. 22, pp. 4532–4534, 2004.

[39] P. R. Pukite, A. Harwit, and S. S. Iyer, "Molecular beam epitaxy of metastable, diamond structure SnxGe1-x alloys," *Applied Physics Letters*, vol. 54, no. 21, pp. 2142–2144, 1989.

[40] W. Wegscheider *et al.*, "Fabrication and properties of epitaxially stabilized Ge / α-Sn heterostructures on Ge(001)," *Journal of Crystal Growth*, vol. 123, no. 1, pp. 75–94, 1992.

[41] S. Oguz *et al.*, "Synthesis of metastable, semiconducting Ge-Sn alloys by pulsed UV laser crystallization," *Applied Physics Letters*, vol. 43, no. 9, pp. 848–850, 1983.

[42] S. Shah *et al.*, "Growth of single-crystal metastable $Ge_{1-x}Sn_x$ alloys on Ge(100) and GaAs(100) substrates," *Journal of Crystal Growth*, vol. 83, no. 1, pp. 3–10, 1987.

[43] S. M. Lee, "Microstructural stability of metastable amorphous and crystalline $Ge_{1-x}Sn_x$ alloys," *Journal of Applied Physics*, vol. 75, no. 4, pp. 1987–1992, 1994.

[44] R. R. Lieten *et al.*, "Tensile strained GeSn on Si by solid phase epitaxy," *Applied Physics Letters*, vol. 102, no. 5, p. 052106, 2013.

[45] M. E. Taylor *et al.*, "Solid phase epitaxy of diamond cubic Sn_xGe_{1-x} alloys," *Journal of Applied Physics*, vol. 80, no. 8, pp. 4384–4388, 1996.

[46] M. Taylor *et al.*, "Inhibited SN Surface Segregation in epitaxial Sn_xGe_{1-x} Alloy Films Grown by Pulsed Laser Deposition," *MRS Proceedings*, vol. 388, p. 97, 1995.

[47] T. Maruyama and H. Akagi, "Thin Films of Amorphous Germanium-Tin Alloys Prepared by Radio-Frequency Magnetron Sputtering," *Journal of The Electrochemical Society*, vol. 145, no. 4, pp. 1303–1305, 1998.

[48] K. A. Bratland *et al.*, "Sn-mediated Ge/Ge(001) growth by low-temperature molecular-beam epitaxy: Surface smoothening and enhanced epitaxial thickness," *Journal of Applied Physics*, vol. 97, no. 4, p. 044904, 2005.

[49] E. Kasper *et al.*, "Growth of silicon based germanium tin alloys," *Thin Solid Films*, vol. 520, no. 8, pp. 3195–3200, 2012.

[50] M. Rojas-López *et al.*, "Raman scattering from fully strained $Ge_{1-x}Sn_x$ ($x \leqslant 0.22$) alloys grown on Ge(001)2×1 by low-temperature molecular beam epitaxy," *Journal of Applied Physics*, vol. 84, no. 4, pp. 2219–2223, 1998.

[51] J. Piao, "Molecular-beam epitaxial growth of metastable $Ge_{1-x}Sn_x$ alloys," *Journal of Vacuum Science & Technology B: Microelectronics and Nanometer Structures*, vol. 8, no. 2, p. 221, 1990.

[52] M. Oehme *et al.*, "Epitaxial growth of highly compressively strained GeSn alloys up to 12.5% Sn," *Journal of Crystal Growth*, vol. 384, pp. 71–76, 2013.

[53] H. Höchst, M. A. Engelhardt, and I. Hernández-Calderón, "Angle-resolved photoemission study of thin molecular-beam-epitaxy-grown α - Sn_xGe_{1-x} films with $x \sim 0.5$," *Physical Review B*, vol. 40, no. 14, pp. 9703–9708, 1989.

[54] E. A. Fitzgerald *et al.*, "Epitaxially stabilized $Ge_{1-x}Sn_x$ diamond cubic alloys," *Journal of Electronic Materials*, vol. 20, no. 6, pp. 489–501, 1991.

[55] M. T. Asom *et al.*, "Epitaxial growth of metastable SnGe alloys," *Applied Physics Letters*, vol. 55, no. 6, pp. 578–579, 1989.

[56] G. He and H. A. Atwater, "Synthesis of epitaxial Sn_xGe_{1-x} alloy films by ion-assisted molecular beam epitaxy," *Applied Physics Letters*, vol. 68, no. 5, pp. 664–666, 1996.

[57] M. Bauer *et al.*, "Ge–Sn semiconductors for band-gap and lattice engineering," *Applied Physics Letters*, vol. 81, no. 16, pp. 2992–2994, 2002.

[58] C. L. Senaratne *et al.*, "Advances in Light Emission from Group-IV Alloys via Lattice Engineering and n-Type Doping Based on Custom-Designed Chemistries," *Chemistry of Materials*, vol. 26, no. 20, pp. 6033–6041, 2014.

[59] S. Wirths *et al.*, "Band engineering and growth of tensile strained Ge/(Si)GeSn heterostructures for tunnel field effect transistors," *Applied Physics Letters*, vol. 102, no. 19, p. 192103, 2013.

[60] ——, "Reduced Pressure CVD Growth of Ge and $Ge_{1-x}Sn_x$ Alloys," *ECS Journal of Solid State Science and Technology*, vol. 2, no. 5, pp. N99–N102, 2013.

[61] S. Assali *et al.*, "Atomically uniform sn-rich gesn semiconductors with 3.0–3.5 um room-temperature optical emission," *Applied Physics Letters*, vol. 112, no. 25, p. 251903, 2018.

[62] O. Gurdal *et al.*, "Low-temperature growth and critical epitaxial thicknesses of fully strained metastable $Ge_{1-x}Sn_x$ ($x \lesssim 0.26$) alloys on Ge(001)2×1," *Journal of Applied Physics*, vol. 83, no. 1, pp. 162–170, 1998.

[63] S. Wirths, D. Buca, and S. Mantl, "Si–Ge–Sn alloys: From growth to applications," *Progress in Crystal Growth and Characterization of Materials*, vol. 62, no. 1, pp. 1–39, 2016.

[64] J. Taraci *et al.*, "Simple chemical routes to diamond-cubic germanium–tin alloys," *Applied Physics Letters*, vol. 78, no. 23, pp. 3607–3609, 2001.

[65] B. Vincent *et al.*, "Undoped and *in-situ* B doped GeSn epitaxial growth on Ge by atmospheric pressure-chemical vapor deposition," *Applied Physics Letters*, vol. 99, no. 15, p. 152103, 2011.

[66] F. Gencarelli *et al.*, "Crystalline Properties and Strain Relaxation Mechanism of CVD Grown GeSn," *ECS Journal of Solid State Science and Technology*, vol. 2, no. 4, pp. P134–P137, 2013.

[67] ——, "Low-temperature Ge and GeSn Chemical Vapor Deposition using Ge_2H_6," *Thin Solid Films*, vol. 520, no. 8, pp. 3211–3215, 2012.

[68] J. Margetis *et al.*, "Fundamentals of $Ge_{1-x}Sn_x$ and $Si_yGe_{1-x-y}Sn_x$ RPCVD epitaxy," *Materials Science in Semiconductor Processing*, vol. 70, pp. 38–43, 2017.

[69] S. Assali, J. Nicolas, and O. Moutanabbir, "Enhanced sn incorporation in gesn epitaxial semiconductors via strain relaxation," *Journal of Applied Physics*, vol. 125, no. 2, p. 025304, 2019.

[70] J. Margetis *et al.*, "Growth and Characterization of epitaxial $Ge_{1-x}Sn_x$ alloys and Heterostructures Using a Commercial CVD System," *ECS Transactions*, vol. 64, no. 6, pp. 711–720, 2014.

[71] A. Mosleh *et al.*, "Material Characterization of $Ge_{1-x}Sn_x$ Alloys Grown by a Commercial CVD System for Optoelectronic Device Applications," *Journal of Electronic Materials*, vol. 43, no. 4, pp. 938–946, 2014.

[72] R. Chen *et al.*, "Material characterization of high Sn-content, compressively-strained GeSn epitaxial films after rapid thermal processing," *Journal of Crystal Growth*, vol. 365, pp. 29–34, 2013.

[73] J. Margetis *et al.*, "Strain engineering in epitaxial $Ge_{1-x}Sn_x$: A path towards low-defect and high Sn-content layers," *Semiconductor Science and Technology*, vol. 32, no. 12, p. 124006, 2017.

[74] J. Aubin *et al.*, "Growth and structural properties of step-graded, high Sn content GeSn layers on Ge," *Semiconductor Science and Technology*, vol. 32, no. 9, p. 094006, 2017.

[75] K. P. Homewood and M. A. Lourenço, "The rise of the GeSn laser," *Nature Photonics*, vol. 9, no. 2, pp. 78–79, 2015.

[76] Y. Zhou *et al.*, "Optically Pumped GeSn Lasers Operating at 270 K with Broad Waveguide Structures on Si," *ACS Photonics*, vol. 6, no. 6, pp. 1434–1441, Jun. 2019.

[77] J. Chrétien *et al.*, "GeSn Lasers Covering a Wide Wavelength Range Thanks to Uniaxial Tensile Strain," *ACS Photonics*, vol. 6, no. 10, pp. 2462–2469, 2019.

[78] D. Stange *et al.*, "GeSn/SiGeSn Heterostructure and Multi Quantum Well Lasers," *ACS Photonics*, vol. 5, no. 11, pp. 4628–4636, 2018.

[79] ——, "Optically Pumped GeSn Microdisk Lasers on Si," *ACS Photonics*, vol. 3, no. 7, pp. 1279–1285, 2016.

[80] A. Elbaz *et al.*, "Ultra-low-threshold continuous-wave and pulsed lasing in tensile-strained GeSn alloys," *Nature Photonics*, vol. 14, no. 6, pp. 375–382, 2020.

[81] L. Casiez *et al.*, "GeSn heterostructures LEDs for gas detection," in *2020 IEEE Photonics Conference (IPC)*. Vancouver, BC, Canada: IEEE, 2020, pp. 1–2.

[82] L. Peng *et al.*, "Room-temperature direct-bandgap electroluminescence from type-I GeSn/SiGeSn multiple quantum wells for 2 Mm LEDs," *Journal of Luminescence*, vol. 228, p. 117539, 2020.

[83] D. Stange *et al.*, "Short-wave infrared LEDs from GeSn/SiGeSn multiple quantum wells," *Optica*, vol. 4, no. 2, p. 185, 2017.

[84] S. Xu *et al.*, "High-speed photo detection at two-micron-wavelength: Technology enablement by GeSn/Ge multiple-quantum-well photodiode on 300 mm Si substrate," *Optics Express*, vol. 27, no. 4, p. 5798, 2019.

[85] Y. Dong *et al.*, "Germanium-tin multiple quantum well on silicon avalanche photodiode for photodetection at two micron wavelength," *Semiconductor Science and Technology*, vol. 31, no. 9, p. 095001, 2016.

[86] M. R. M. Atalla *et al.*, "All-Group IV Transferable Membrane Mid-Infrared Photodetectors," *Advanced Functional Materials*, vol. 31, no. 3, p. 2006329, 2021.

[87] B. E. A. Saleh, *Fundamentals of Photonics*, ser. Wiley Series in Pure and Applied Optics. Wiley, 2019.

[88] S. L. Chuang, *Physics of Photonic Devices*, 2nd ed., ser. Wiley Series in Pure and Applied Optics. Wiley, 2009.

[89] P. T. Landsberg, *Recombination in Semiconductors*, 1st ed. Cambridge University Press, 1992.

[90] D.-L. Zhang *et al.*, "Theoretical study of the optical gain characteristics of a $Ge_{1-x}Sn_x$ alloy for a short-wave infrared laser," *Chinese Physics B*, vol. 24, no. 2, p. 024211, 2015.

[91] H. Hong *et al.*, "Limitation of bulk GeSn alloy in the application of a high-performance laser due to the high threshold," *Optics Express*, vol. 29, no. 1, p. 441, 2021.

[92] G. Sun, R. A. Soref, and H. H. Cheng, "Design of a Si-based lattice-matched room-temperature GeSn/GeSiSn multi-quantum-well mid-infrared laser diode," *Optics Express*, vol. 18, no. 19, p. 19957, 2010.

[93] M. Prost *et al.*, "Analysis of optical gain threshold in n-doped and tensile-strained germanium heterostructure diodes," *Journal of Applied Physics*, vol. 118, no. 12, p. 125704, 2015.

[94] M. Osiński, M. Polish, and M. Adams, "Gain spectra of quaternary semiconductors," *IEE Proceedings I Solid State and Electron Devices*, vol. 129, no. 6, p. 229, 1982.

[95] K. K. N. S.M. Sze, *Physics of Semiconductor Devices*. John Wiley & Sons, Ltd, 2006, ch. 1, pp. 5–75.

[96] E. F. Schubert *et al.*, "Alloy broadening in photoluminescence spectra of Al x Ga 1 - x As," *Physical Review B*, vol. 30, no. 2, pp. 813–820, 1984.

[97] D. Ouadjaout and Y. Marfaing, "Localized excitons in II-VI semiconductor alloys: Density-of-states model and photoluminescence line-shape analysis," *Physical Review B*, vol. 41, no. 17, pp. 12 096–12 105, 1990.

[98] M. Asada, "Intraband relaxation time in quantum-well lasers," *IEEE Journal of Quantum Electronics*, vol. 25, no. 9, pp. 2019–2026, 1989.

[99] W. W. Chow, S. W. Koch, and M. Sargent, *Semiconductor-Laser Physics*. Berlin ; New York: Springer-Verlag, 1997, pp. 94–95.

[100] J. K. Katahara and H. W. Hillhouse, "Quasi-Fermi level splitting and sub-bandgap absorptivity from semiconductor photoluminescence," *Journal of Applied Physics*, vol. 116, no. 17, p. 173504, 2014.

[101] D. Stange, "Group IV (Si)GeSn light emission and lasing studies," Dissertation, RWTH Aachen University, Jülich, 2019, druckausgabe: 2019. - Onlineausgabe: 2019. - Auch veröffentlicht auf dem Publikationsserver der RWTH Aachen University; Dissertation, RWTH Aachen University, 2019.

[102] S. Wirths, "Group IV epitaxy for advanced nano- and optoelectronic applications," Dissertation, RWTH Aachen, Jülich, 2016, druckausgabe: 2016. - Onlineausgabe: 2016. - Auch veröffentlicht auf dem Publikationsserver der RWTH Aachen University; Dissertation, RWTH Aachen, 2015.

[103] N. W. Ashcroft and N. D. Mermin, *Solid State Physics*. Holt, Rinehart and Winston, 1976.

[104] G. F. Bassani and G. Pastori Parravicini, *Electronic States and Optical Transitions in Solids*, 1st ed., ser. International Series of Monographs in the Science of the Solid State, v. 8. Pergamon Press, 1975.

[105] E. Kane, "Chapter 3 The k • p Method," in *Semiconductors and Semimetals*. Elsevier, 1966, vol. 1, pp. 75–100.

[106] J. Bardeen, "An improved calculation of the energies of metallic *li* and *na*," *The Journal of Chemical Physics*, vol. 6, no. 7, pp. 367–371, 1938.

[107] F. Seitz, *The Modern Theory of Solids*. McGraw-Hill Book, 1940, p. 352.

[108] T. Eißfeller, *Theory of the Electronic Structure of Quantum Dots in External Fields*, 1st ed., ser. Selected Topics of Semiconductor Physics and Technology. Verein zur Förderung des Walter-Schottky-Inst. der Techn. Univ. München, 2012, no. Vol. 146.

[109] T. B. Bahder, "Eight-band $\mathbf{k} \cdot \mathbf{p}$ model of strained zinc-blende crystals," *Physical Review B*, vol. 41, no. 17, pp. 11 992–12 001, 1990.

[110] R. Winkler, *Spin-Orbit Coupling Effects in Two-Dimensional Electron and Hole Systems*, ser. Springer Tracts in Modern Physics. Springer, 2003, no. v. 191.

[111] P. Löwdin, "A Note on the Quantum-Mechanical Perturbation Theory," *The Journal of Chemical Physics*, vol. 19, no. 11, pp. 1396–1401, 1951.

[112] G. L. Bir and G. E. Pikus, *Symmetry and strain-induced effects in semiconductors*. Wiley, 1974.

[113] J. M. Hinckley and J. Singh, "Influence of substrate composition and crystallographic orientation on the band structure of pseudomorphic Si-Ge alloy films," *Physical Review B*, vol. 42, no. 6, pp. 3546–3566, 1990.

[114] D. J. Paul, "8-band k · p modelling of mid-infrared intersubband absorption in Ge quantum wells," *Journal of Applied Physics*, vol. 120, no. 4, p. 043103, 2016.

[115] R. R. Reeber and K. Wang, "Thermal expansion and lattice parameters of group IV semiconductors," *Materials Chemistry and Physics*, vol. 46, no. 2-3, pp. 259–264, 1996.

[116] G.-E. Chang, S.-W. Chang, and S. L. Chuang, "Strain-Balanced Ge_zSn_{1-z}−$Si_xGe_ySn_{1-x-y}$ Multiple-Quantum-Well Lasers," *IEEE Journal of Quantum Electronics*, vol. 46, no. 12, pp. 1813–1820, 2010.

[117] O. Madelung, Ed., *Semiconductors. Group IV Elements and III-V Compounds*, ser. Data in Science and Technology. Springer-Verlag, 1991.

[118] M. Bertrand *et al.*, "Experimental Calibration of Sn-Related Varshni Parameters for High Sn Content GeSn Layers," *Annalen der Physik*, vol. 531, no. 6, p. 1800396, 2019.

[119] M. P. Polak, P. Scharoch, and R. Kudrawiec, "The electronic band structure of $Ge_{1-x}Sn_x$ in the full composition range: Indirect, direct, and inverted gaps regimes, band offsets, and the Burstein–Moss effect," *Journal of Physics D: Applied Physics*, vol. 50, no. 19, p. 195103, 2017.

[120] P. Lawaetz, "Valence-Band Parameters in Cubic Semiconductors," *Physical Review B*, vol. 4, no. 10, pp. 3460–3467, 1971.

[121] F. Szmulowicz, "Derivation of a general expression for the momentum matrix elements within the envelope-function approximation," *Physical Review B*, vol. 51, no. 3, pp. 1613–1623, 1995.

[122] S. Birner, *Modeling of Semiconductor Nanostructures and Semiconductor-Electrolyte Interfaces*, 1st ed., ser. Selected Topics of Semiconductor Physics and Technology. Verein zur Förderung des Walter Schottky Instituts der Technischen Universität München, 2011, no. vol. 135.

[123] T. Andlauer, *Optoelectronic and Spin-Related Properties of Semiconductor Nanostructures in Magnetic Fields*, 1st ed., ser. Selected Topics of Semiconductor Physics and Technology. Verein zur Förderung des Walter Schottky Inst. der Techn. Univ. München e.V, 2009, no. 105.

[124] H. J. Monkhorst and J. D. Pack, "Special points for Brillouin-zone integrations," *Physical Review B*, vol. 13, no. 12, pp. 5188–5192, 1976.

[125] D. J. Chadi and M. L. Cohen, "Special Points in the Brillouin Zone," *Physical Review B*, vol. 8, no. 12, pp. 5747–5753, 1973.

[126] D. Zaharioudakis, "Tetrahedron methods for Brillouin zone integration," *Computer Physics Communications*, vol. 157, no. 1, pp. 17–31, 2004.

[127] G. Lehmann and M. Taut, "On the Numerical Calculation of the Density of States and Related Properties," *Physica Status Solidi (b)*, vol. 54, no. 2, pp. 469–477, 1972.

[128] P. E. Blöchl, O. Jepsen, and O. K. Andersen, "Improved tetrahedron method for Brillouin-zone integrations," *Physical Review B*, vol. 49, no. 23, pp. 16 223–16 233, 1994.

[129] P. Enders, "Special-lines approximation to Brillouin zone integration," *Semiconductor Science and Technology*, vol. 11, no. 2, pp. 187–189, 1996.

[130] E. Kane, "Energy band structure in p-type germanium and silicon," *Journal of Physics and Chemistry of Solids*, vol. 1, no. 1-2, pp. 82–99, 1956.

[131] P. Enders, "Addendum to 'Special-lines approximation to Brillouin zone integration': Improved set of special lines," *Semiconductor Science and Technology*, vol. 11, no. 12, pp. 1927–1929, 1996.

[132] R. Hall, "Recombination processes in semiconductors," *Proceedings of the IEE - Part B: Electronic and Communication Engineering*, vol. 106, pp. 923–931(8), May 1959.

[133] F. Stern, "Calculated spectral dependence of gain in excited GaAs," *Journal of Applied Physics*, vol. 47, no. 12, pp. 5382–5386, 1976.

[134] C. B. Su *et al.*, "Carrier dependence of the radiative coefficient in III-V semiconductor light sources," *Applied Physics Letters*, vol. 44, no. 8, pp. 732–734, 1984.

[135] R. Olshansky *et al.*, "Measurement of radiative and nonradiative recombination rates in ingaasp and algaas light sources," *IEEE Journal of Quantum Electronics*, vol. 20, no. 8, pp. 838–854, 1984.

[136] G. P. .-. Agrawal, N. K. Dutta, and N. K. . Dutta, *Semiconductor lasers*, 2nd ed. Van Nostrand Reinhold, 1993. [Online]. Available: http://catalogue.bnf.fr/ark:/12148/cb37428446s

[137] A. R. Beattie and P. T. Landsberg, "Auger effect in semiconductors," *Proceedings of the Royal Society of London. Series A. Mathematical and Physical Sciences*, vol. 249, no. 1256, pp. 16–29, 1959.

[138] A. R. Beattie, "Quantum efficiency in InSb," *Journal of Physics and Chemistry of Solids*, vol. 23, no. 8, pp. 1049–1056, 1962.

[139] Q. Zhang *et al.*, "Theoretical analysis of performance enhancement in GeSn/SiGeSn light-emitting diode enabled by Si $_3$ N $_4$ liner stressor technique," *Applied Optics*, vol. 55, no. 34, p. 9668, dec 2016.

[140] L. A. Coldren, S. W. Corzine, and M. Mashanovitch, *Diode Lasers and Photonic Integrated Circuits*. Wiley, 2006, ch. 4, pp. 157–246.

[141] A. Sugimura, "Band-to-band Auger effect in GaSb and InAs lasers," *Journal of Applied Physics*, vol. 51, no. 8, pp. 4405–4411, 1980.

[142] A. R. Beattie and G. Smith, "Recombination in Semiconductors by a Light Hole Auger Transition," *Physica Status Solidi (B)*, vol. 19, no. 2, pp. 577–586, 1967.

[143] M. Takeshima, "Auger recombination in InAs, GaSb, InP, and GaAs," *Journal of Applied Physics*, vol. 43, no. 10, pp. 4114–4119, 1972.

[144] R. I. Taylor *et al.*, "Auger Recombination in a Quantum-Well-Heterostructure Laser." *IEE Proceedings, Part J: Optoelectronics*, vol. 132, no. 6, pp. 364–370, 1985.

[145] A. Haug, "Auger coefficients for highly doped and highly excited semiconductors," *Solid State Communications*, vol. 28, no. 3, pp. 291–293, 1978.

[146] R. N. Hall, "Electron-Hole Recombination in Germanium," *Physical Review*, vol. 87, no. 2, pp. 387–387, 1952.

[147] W. Shockley and W. T. Read, "Statistics of the Recombinations of Holes and Electrons," *Physical Review*, vol. 87, no. 5, pp. 835–842, 1952.

[148] R. K. Ahrenkiel, Ed., *Semiconductors and Semimetals. 39: Minority Carriers in III-V Semiconductors: Physics and Applications / Vol. Eds: Richard K. Ahrenkiel.* Academic Press, 1993.

[149] J. S. Blakemore and H. K. Henisch, *Semiconductor Statistics.* Pergamon Press, 1962.

[150] M. Grundmann, *The Physics of Semiconductors: An Introduction Including Nanophysics and Applications*, 2nd ed., ser. Graduate Texts in Physics. Springer-Verlag, 2010.

[151] A. S. Grove, *Physics and Technology of Semiconductor Devices.* Wiley, 1967.

[152] D. Macdonald and A. Cuevas, "Validity of simplified Shockley-Read-Hall statistics for modeling carrier lifetimes in crystalline silicon," *Physical Review B*, vol. 67, no. 7, p. 075203, 2003.

[153] A. M. Stoneham, "Non-radiative transitions in semiconductors," *Reports on Progress in Physics*, vol. 44, no. 12, pp. 1251–1295, 1981.

[154] I. V. Markov, *Crystal Growth for Beginners: Fundamentals of Nucleation, Crystal Growth and Epitaxy*, 2nd ed. WORLD SCIENTIFIC, 2003.

[155] M. J. Madou, *Fundamentals of Microfabrication and Nanotechnology, Three-Volume Set*, 0th ed. CRC Press, 2018.

[156] J. Hartmann *et al.*, "Reduced pressure chemical vapor deposition of Ge thick layers on Si(001), Si(011) and Si(111)," *Journal of Crystal Growth*, vol. 310, no. 24, pp. 5287–5296, 2008.

[157] J. M. Hartmann *et al.*, "Epitaxial growth of Ge thick layers on nominal and 6° off Si(0 0 1); Ge surface passivation by Si," *Semiconductor Science and Technology*, vol. 24, no. 5, p. 055002, 2009.

[158] J. Hartmann *et al.*, "Impact of the H2 anneal on the structural and optical properties of thin and thick Ge layers on Si; Low temperature surface passivation of Ge by Si," *Journal of Crystal Growth*, vol. 312, no. 4, pp. 532–541, 2010.

[159] S. Assali *et al.*, "Vacancy complexes in nonequilibrium germanium-tin semiconductors," *Applied Physics Letters*, vol. 114, no. 25, p. 251907, 2019.

[160] J. Margetis *et al.*, "Chemistry and kinetics governing hydride/chloride chemical vapor deposition of epitaxial $Ge_{1-x}Sn_x$," *Journal of Vacuum Science & Technology A*, vol. 37, no. 2, p. 021508, 2019.

[161] L. Milord *et al.*, "Inductively coupled plasma etching of germanium tin for the fabrication of photonic components," in *Silicon Photonics XII*, G. T. Reed and A. P. Knights, Eds., vol. 10108, International Society for Optics and Photonics. SPIE, 2017, pp. 53 – 59.

[162] D. Rainko *et al.*, "Impact of tensile strain on low Sn content GeSn lasing," *Scientific Reports*, vol. 9, no. 1, p. 259, 2019.

[163] R. W. Millar *et al.*, "Tensile strained GeSn mid-infrared light emitters," in *2017 IEEE 14th International Conference on Group IV Photonics (GFP)*, 2017, pp. 49–50.

[164] K. Nojiri, *Dry Etching Technology for Semiconductors*, 1st ed. Springer International Publishing : Imprint: Springer, 2015.

[165] R. Cheng *et al.*, "Relaxed and Strained Patterned Germanium-Tin Structures: A Raman Scattering Study," *ECS Journal of Solid State Science and Technology*, vol. 2, no. 4, pp. P138–P145, 2013.

[166] Y. Dong *et al.*, "Etching of germanium-tin using ammonia peroxide mixture," *Journal of Applied Physics*, vol. 118, no. 24, p. 245303, 2015-12-28.

[167] S. Gupta *et al.*, "Highly Selective Dry Etching of Germanium over Germanium–Tin ($Ge_{1-x}Sn_x$): A Novel Route for $Ge_{1-x}Sn_x$ Nanostructure Fabrication," *Nano Letters*, vol. 13, no. 8, pp. 3783–3790, 2013.

[168] A. Elbaz *et al.*, "Reduced Lasing Thresholds in GeSn Microdisk Cavities with Defect Management of the Optically Active Region," *ACS Photonics*, vol. 7, no. 10, pp. 2713–2722, 2020.

[169] K. Guilloy *et al.*, "High aspect ratio germanium nanowires obtained by dry etching," *MRS Advances*, vol. 1, no. 13, pp. 875–880, 2016.

[170] J. Aubin and J. Hartmann, "GeSn growth kinetics in reduced pressure chemical vapor deposition from Ge2H6 and SnCl4," *Journal of Crystal Growth*, vol. 482, pp. 30–35, 2018.

[171] N. S. Fernando *et al.*, "Band gap and strain engineering of pseudomorphic $Ge_{1-x-y}Si_xSn_y$ alloys on Ge and GaAs for photonic applications," *Journal of Vacuum Science & Technology B, Nanotechnology and Microelectronics: Materials, Processing, Measurement, and Phenomena*, vol. 36, no. 2, p. 021202, 2018.

[172] M. Fukuda *et al.*, "Control of $Ge_{1-x-y}Si_xSn_y$ layer lattice constant for energy band alignment in $Ge_{1-x}Sn_x$ / $Ge_{1-x-y}Si_xSn_y$ heterostructures," *Semiconductor Science and Technology*, vol. 32, no. 10, p. 104008, 2017.

[173] A. Gassenq *et al.*, "Gamma bandgap determination in pseudomorphic GeSn layers grown on Ge with up to 15% Sn content," *Applied Physics Letters*, vol. 109, no. 24, p. 242107, 2016.

[174] J. Margetis *et al.*, "Study of low-defect and strain-relaxed GeSn growth via reduced pressure CVD in H2 and N2 carrier gas," *Journal of Crystal Growth*, vol. 463, pp. 128–133, 2017.

[175] V. Reboud *et al.*, "Optically pumped GeSn micro-disks with 16% Sn lasing at 3.1 um up to 180 K," *Applied Physics Letters*, vol. 111, no. 9, p. 092101, 2017.

[176] Q. M. Thai *et al.*, "2D hexagonal photonic crystal GeSn laser with 16% Sn content," *Applied Physics Letters*, vol. 113, no. 5, p. 051104, 2018.

[177] C. Ferrari, E. Buffagni, and F. Rossi, "Chapter 3 - Strain and Composition Determination in Semiconductor Heterostructures by High-Resolution X-Ray Diffraction," in *Characterization of Semiconductor Heterostructures and Nanostructures (Second Edition)*, C. Lamberti and G. Agostini, Eds. Elsevier, 2013, pp. 75–111.

[178] M. O. Möller *et al.*, "New methods for depth profiling of heterostructures by X-ray diffraction," *Il Nuovo Cimento D*, vol. 19, no. 2, pp. 321–328, 1997.

[179] P. F. Fewster, "Multicrystal X-ray diffraction of heteroepitaxial structures," *Applied Surface Science*, vol. 50, no. 1, pp. 9–18, 1991.

[180] G. G. Stokes, "XXX. On the change of refrangibility of light," *Philosophical Transactions of the Royal Society of London*, vol. 142, pp. 463–562, 1852.

[181] V. P. Gribkovskii, *Theory of Luminescence*. Boston, MA: Springer US, 1998, pp. 1–43. [Online]. Available: https://doi.org/10.1007/978-1-4615-5361-8_1

[182] L. Pavesi and M. Guzzi, "Photoluminescence of AlxGa1-xAs alloys," *Journal of Applied Physics*, vol. 75, no. 10, pp. 4779–4842, 1994.

[183] A. A. Michelson and E. W. Morley, "On the relative motion of the Earth and the luminiferous ether," *American Journal of Science*, vol. s3-34, no. 203, pp. 333–345, 1887.

[184] N. Jaggi and D. Vij, *Fourier transform infrared spectroscopy*. Boston, MA: Springer US, 2006, pp. 411–450.

[185] J. Gronholz and W. Herres, "Understanding ftir data processing, combined reprint of huethig publishers," *Instruments and Computers*, vol. 1, 1984.

[186] F. Harris, "On the use of windows for harmonic analysis with the discrete Fourier transform," *Proceedings of the IEEE*, vol. 66, no. 1, pp. 51–83, 1978.

[187] S. Sauvage *et al.*, "Midinfrared unipolar photoluminescence in InAs/GaAs self-assembled quantum dots," *Physical Review B*, vol. 60, no. 23, pp. 15 589–15 592, 1999.

[188] J. Shao *et al.*, "Modulated photoluminescence spectroscopy with a step-scan Fourier transform infrared spectrometer," *Review of Scientific Instruments*, vol. 77, no. 6, p. 063104, 2006.

[189] C. J. Manning and P. R. Griffiths, "Noise Sources in Step-Scan FT-IR Spectrometry," *Applied Spectroscopy*, vol. 51, no. 8, pp. 1092–1101, 1997.

[190] L. Liu *et al.*, "Investigation on the effective mass of $Ge_{1-x}Sn_x$ alloys and the transferred-electron effect," *Applied Physics Express*, vol. 8, no. 3, p. 031301, 2015.

[191] E. Burstein, "Anomalous Optical Absorption Limit in InSb," *Physical Review*, vol. 93, no. 3, pp. 632–633, 1954.

[192] S. Assali *et al.*, "Optical study of the band structure of wurtzite gap nanowires," *Journal of Applied Physics*, vol. 120, no. 4, p. 044304, 2016.

[193] U. Kaufmann *et al.*, "Nature of the 2.8 eV photoluminescence band in Mg doped GaN," *Applied Physics Letters*, vol. 72, no. 11, pp. 1326–1328, 1998.

[194] T. Schmidt, K. Lischka, and W. Zulehner, "Excitation-power dependence of the near-band-edge photoluminescence of semiconductors," *Physical Review B*, vol. 45, no. 16, pp. 8989–8994, 1992.

[195] C. Rödl *et al.*, "Accurate electronic and optical properties of hexagonal germanium for optoelectronic applications," *Physical Review Materials*, vol. 3, no. 3, p. 034602, 2019.

[196] J. Dong and D. Xiong, "Applications of Light Emitting Diodes in Health Care," *Annals of Biomedical Engineering*, vol. 45, no. 11, pp. 2509–2523, 2017.

[197] W. Zeller *et al.*, "DFB Lasers Between 760 nm and 16 Mm for Sensing Applications," *Sensors*, vol. 10, no. 4, pp. 2492–2510, 2010.

[198] E. Bouthillier *et al.*, "Decoupling the effects of composition and strain on the vibrational modes of GeSn semiconductors," *Semiconductor Science and Technology*, vol. 35, no. 9, p. 095006, 2020.

[199] K. Gallacher *et al.*, "Ohmic contacts to n-type germanium with low specific contact resistivity," *Applied Physics Letters*, vol. 100, no. 2, p. 022113, jan 2012.

[200] E. M. T. Fadaly *et al.*, "Direct-bandgap emission from hexagonal Ge and SiGe alloys," *Nature*, vol. 580, no. 7802, pp. 205–209, 2020.

[201] V. R. D'Costa *et al.*, "Optical critical points of thin-film Ge 1-y Sn y alloys: A comparative Ge 1 - y Sn y / Ge 1-x Si x study," *Physical Review B*, vol. 73, no. 12, p. 125207, 2006.

[202] J. D. Gallagher *et al.*, "Compositional dependence of the bowing parameter for the direct and indirect band gaps in ge1-ysny alloys," *Applied Physics Letters*, vol. 105, no. 14, p. 142102, 2014.

[203] Y. Chibane, B. Bouhafs, and M. Ferhat, "Unusual structural and electronic properties of Sn_xGe_{1-x} alloys," *physica status solidi (b)*, vol. 240, no. 1, pp. 116–119, 2003.

[204] M. Khajavikhan *et al.*, "Thresholdless nanoscale coaxial lasers," *Nature*, vol. 482, no. 7384, pp. 204–207, 2012.

[205] G. Sun, R. A. Soref, and H. H. Cheng, "Design of an electrically pumped SiGeSn/GeSn/SiGeSn double-heterostructure midinfrared laser," *Journal of Applied Physics*, vol. 108, no. 3, p. 033107, Aug. 2010.

[206] H. Wen, B. Pinkie, and E. Bellotti, "Direct and phonon-assisted indirect Auger and radiative recombination lifetime in HgCdTe, InAsSb, and InGaAs computed using Green's function formalism," *Journal of Applied Physics*, vol. 118, no. 1, p. 015702, 2015.

[207] M. Takeshima, "Unified theory of the impurity and phonon scattering effects on Auger recombination in semiconductors," *Physical Review B*, vol. 25, no. 8, pp. 5390–5414, 1982.

[208] H. Wen and E. Bellotti, "Rigorous theory of the radiative and gain characteristics of silicon and germanium lasing media," *Physical Review B*, vol. 91, no. 3, p. 035307, 2015.

[209] S. Dominici *et al.*, "Numerical study on the optical and carrier recombination processes in GeSn alloy for E-SWIR and MWIR optoelectronic applications," *Optics Express*, vol. 24, no. 23, p. 26363, 2016.

[210] K. Yoshida, H. Nakanotani, and C. Adachi, "Effect of Joule heating on transient current and electroluminescence in p - i - n organic light-emitting diodes under pulsed voltage operation," *Organic Electronics*, vol. 31, pp. 287–294, 2016.

[211] I. N. Bronshtein *et al.*, *Handbook of Mathematics*. Springer Berlin Heidelberg, 2004.

APPENDIX A SPONTANEOUS EMISSION SPECTRUM AND JOINT DENSITY OF STATES

Here, we only consider the $\vec{\boldsymbol{k}}$-conserving transitions. The bands are also considered to be spin-degenerated. In that case, the spontaneous emission spectrum is given by

$$\begin{aligned} r^{spon}(\hbar\omega) &= \frac{2}{V}(\hbar\omega)\left(\frac{n_r e^2 M_b^2}{\pi c^3 \varepsilon_0 \hbar^4}\right)\sum_v \sum_{\vec{\boldsymbol{k}}} \delta\left(\epsilon_c(\vec{\boldsymbol{k}}_c) - \epsilon_v(\vec{\boldsymbol{k}}_v) - \hbar\omega\right) f\left(\epsilon_c, \mu_e\right)\left[1 - f\left(\epsilon_v, \mu_h\right)\right] \\ &= \frac{2\hbar\omega n_r e^2 M_b^2}{\pi c^3 \varepsilon_0 \hbar^4}\sum_v \int \delta\left(E_{c,v} + \frac{\hbar^2\left|\vec{\boldsymbol{k}}\right|^2}{2m_{c,v}} - \hbar\omega\right) f\left(\epsilon_c, \mu_e\right)\left[1 - f\left(\epsilon_v, \mu_h\right)\right]\frac{\mathrm{d}^3\vec{\boldsymbol{k}}}{(2\pi)^3} \end{aligned} \tag{A.1}$$

For a function g, the Dirac delta function $\delta\left(g(x)\right)$ is given by [211]

$$\delta\Big(g(x)\Big) = \sum_{i=1}^{n} \frac{1}{|g'(x_i)|}\delta\left(x - x_i\right) \text{ with } g(x_i) = 0 \text{ and } g'(x_i) \neq 0 \tag{A.2}$$

In our case, $g\Big(\left|\vec{\boldsymbol{k}}\right|\Big) = E_{c,v} + \frac{\hbar^2\left|\vec{\boldsymbol{k}}\right|^2}{2m_{c,v}} - \hbar\omega$ and $g'\Big(\left|\vec{\boldsymbol{k}}\right|\Big) = \hbar^2\left|\vec{\boldsymbol{k}}\right|/m_{c,v}$. We also define

$$\left|\vec{\boldsymbol{k}}_0\right| = \left(\frac{2m_{c,v}}{\hbar^2}\right)^{1/2}\Big(\hbar\omega - E_{c,v}\Big)^{1/2} H\Big(\hbar\omega - E_{c,v}\Big) \tag{A.3}$$

where H is the Heaviside step-function.
When we take the equations (A.2) and (A.3) into account, (A.1) becomes

$$\begin{aligned} r^{spon}(\hbar\omega) &= \frac{2\hbar\omega n_r e^2 M_b^2}{\pi c^3 \varepsilon_0 \hbar^4}\sum_v \int \frac{m_{c,v}}{\hbar^2 k_0}\delta\left(k - k_0\right) f\left(\epsilon_c, \mu_e\right)\left[1 - f\left(\epsilon_v, \mu_h\right)\right]\frac{k^2\,\mathrm{d}k}{2\pi^2} \\ &= \frac{2\hbar\omega n_r e^2 M_b^2}{\pi c^3 \varepsilon_0 \hbar^4}\sum_v \left[\frac{1}{2\pi^2}\left(\frac{m_{c,v}}{\hbar^2}\right)k_0\right] f\Big(\epsilon_c(k_0), \mu_e\Big)\Big[1 - f\Big(\epsilon_v(k_0), \mu_h\Big)\Big] \\ r^{spon}(\hbar\omega) &= \left(\frac{n_r e^2 \hbar\omega M_b^2}{\pi c^3 \varepsilon_0 \hbar^4}\right)\sum_v \rho_{JDOS}\left(\hbar\omega - E_{c,v}\right) f\Big(\epsilon_c(\hbar\omega), \mu_e\Big)\Big[1 - f\Big(\epsilon_v(\hbar\omega), \mu_h\Big)\Big] \end{aligned} \tag{A.4}$$

with

- $\rho_{JDOS}(\epsilon) = \frac{1}{2\pi^2}\left(\frac{2m_{c,v}}{\hbar^2}\right)^{3/2} H(\epsilon)\sqrt{\epsilon}$ the joint density of states,
- $\epsilon_c(\hbar\omega) = E_c + \frac{m_{c,v}}{m_c^*}\Big(\hbar\omega - E_{c,v}\Big)$, $\epsilon_v(\hbar\omega) = E_v - \frac{m_{c,v}}{m_v^*}\Big(\hbar\omega - E_{c,v}\Big)$

APPENDIX B CARRIER DENSITIES, QUASI-FERMI LEVELS AND LOW INJECTION REGIME

For a non-degenerately doped semiconductor at thermal equilibrium, the quasi-Fermi level lies within the bandgap and away from the different band edges by several k_BT. In that case, the electrons charge density n in a semiconductor material is given by

$$n = \frac{2}{V}\sum_{\vec{k}} \int \delta\left(\epsilon - \epsilon_c(\vec{k})\right) \exp\left(-\frac{\epsilon - E_f}{k_BT}\right) \mathrm{d}\epsilon \tag{B.1}$$

With the SBEMA, $\epsilon_c(\vec{k})$ is written as presented in equation (3.3). We can also turn the summation over the wavevector k into an integral over the BZ. In that case, the equation above becomes

$$\begin{aligned}
n &= \frac{1}{4\pi^3} \int_k \int_\epsilon \mathrm{d}^3k \times \delta\left(\epsilon - \epsilon_c(k)\right) \exp\left(-\frac{\epsilon - E_f}{k_BT}\right) \mathrm{d}\epsilon \\
&= \frac{1}{4\pi^3} \int_k \exp\left(-\frac{\epsilon_c(k) - E_f}{k_BT}\right) \mathrm{d}^3k \\
&= \frac{1}{\pi^2} \int \exp\left[-\frac{1}{k_BT}\left(E_c + \frac{\hbar^2k^2}{2m_c} - E_f\right)\right] k^2 \,\mathrm{d}k \\
&= \frac{1}{2\pi^2}\left(\frac{2m_c}{\hbar^2}\right)^{3/2} \int_{E_c}^{+\infty} \sqrt{\epsilon - E_c} \times \exp\left(-\frac{\epsilon - E_f}{k_BT}\right) \mathrm{d}\epsilon \\
n &= \frac{1}{2\pi^2}\left(\frac{2m_ck_BT}{\hbar^2}\right)^{3/2} \left(\int_0^{+\infty} x^{1/2}e^{-x}\,\mathrm{d}x\right) \exp\left(-\frac{E_c - E_f}{k_BT}\right)
\end{aligned} \tag{B.2}$$

The integral inside the bracket is nothing more than the gamma function Γ evaluated on $3/2$ and, the result is $\sqrt{\pi}/2$. We, therefore, get

$$n = 2\left(\frac{m_ck_BT}{2\pi\hbar^2}\right)^{3/2} \exp\left(\frac{E_f - E_c}{k_BT}\right) \tag{B.3}$$

Using the same method as above, we show that the hole's charge density p is also given by equation (B.4), in which we have ignored the contribution from the split-off band.

$$p = 2\left(\frac{k_BT}{2\pi\hbar^2}\right)^{3/2} \left[m_{hh}^{3/2} \exp\left(\frac{E_{hh} - E_f}{k_BT}\right) + m_{lh}^{3/2} \exp\left(\frac{E_{lh} - E_f}{k_BT}\right)\right] \tag{B.4}$$

When the semiconductor is exposed to an external excitation so that a sufficiently weak injection is performed, the thermal equilibrium Fermi level E_f is replaced by the newly formed quasi-Fermi levels which, will also lie within the bandgap and away from the different band edges by several k_BT. In that case, the carriers charge densities are still defined by the same formulas as before with E_f replaced by μ_e in equation (B.3) and by μ_h in equation (B.4). The coefficients D_{hh} and D_{lh} from equation (3.7) can therefore be written as

$$\begin{aligned} D_{hh} &= \left(\frac{2m_{c,hh}}{m_c}\right)^{3/2} \frac{np}{K_{hh}(T)}\hbar\omega \\ D_{lh} &= \left(\frac{2m_{c,lh}}{m_c}\right)^{3/2} \frac{np}{K_{lh}(T)}\hbar\omega \end{aligned} \tag{B.5}$$

where we have

$$\begin{aligned} K_{hh}(T) &= \left(\frac{k_B^3T^3c^3\varepsilon_0\hbar}{n_re^2M_b^2}\right)\left[m_{hh}^{3/2} + m_{lh}^{3/2}\exp\left(\frac{E_{lh}-E_{hh}}{k_BT}\right)\right] \\ K_{lh}(T) &= \left(\frac{k_B^3T^3c^3\varepsilon_0\hbar}{n_re^2M_b^2}\right)\left[m_{lh}^{3/2} + m_{hh}^{3/2}\exp\left(\frac{E_{hh}-E_{lh}}{k_BT}\right)\right] \end{aligned} \tag{B.6}$$

Based on these equations, we can write equation (3.7) as

$$r^{spon}(\hbar\omega) \approx \hbar\omega\left[\sum_v \left(\frac{2m_{c,v}}{m_c}\right)^{3/2} \frac{(\hbar\omega - E_{c,v})^{1/2}}{K_v(T)} \exp\left(-\frac{\hbar\omega - E_{c,v}}{k_BT}\right)\right] np, \quad \hbar\omega \geq E_{c,v} \tag{B.7}$$

The total spontaneous emission rate R_{sp} can in general be calculated by [88]

$$R_{sp} = \int_0^{+\infty} r^{spon}(\hbar\omega)\,\mathrm{d}\hbar\omega \tag{B.8}$$

With the spontaneous emission spectrum defined by equation (B.7) we have

$$R_{sp} = \sum_v \left(\frac{2m_{c,v}}{m_c}\right)^{3/2} \frac{np}{K_v(T)} \int_{E_{c,v}}^{+\infty} \mathrm{d}\hbar\omega \cdot \hbar\omega\,(\hbar\omega - E_{c,v})^{1/2} \exp\left(-\frac{\hbar\omega - E_{c,v}}{k_BT}\right) \tag{B.9}$$

In equation (B.9), the integral can be split into two contributions by substituting $x = (\hbar\omega - E_{c,v})/k_BT$. In that case, we obtain

$$\begin{aligned} R_{sp} &= \sum_v \left(\frac{2m_{c,v}k_BT}{m_c}\right)^{3/2} \frac{np}{K_v(T)}\left[k_BT\int_0^{+\infty} x^{3/2}e^{-x}\,\mathrm{d}x + E_{c,v}\int_0^{+\infty} x^{1/2}e^{-x}\,\mathrm{d}x\right] \\ R_{sp} &= \left[\sum_v \left(\frac{2m_{c,v}k_BT}{m_c}\right)^{3/2} \frac{E_{c,v}}{K_v(T)}\frac{\sqrt{\pi}}{2}\left(1 + \frac{3k_BT}{2E_{c,v}}\right)\right] np = B(T)\cdot np \end{aligned} \tag{B.10}$$

APPENDIX C STEADY-STATE RADIATIVE CARRIER LIFETIME AND NON-DEGENERATE SEMICONDUCTOR

The steady-state radiative carrier lifetime for a non-degenerate semiconductor in weak optical injection regime is given by (see appendix B)

$$\tau_{rad} = \frac{1}{B(n_0 + p_0)} \tag{C.1}$$

For the sake of simplification, we consider an unstrained semiconductor with the assumption that $\frac{3k_BT}{2E_g} \ll 1$. In that case, we have

$$\begin{aligned} K_{hh}(T) &= \left(\frac{k_B^3 T^3 c^3 \varepsilon_0 \hbar}{n_r e^2 M_b^2}\right)\left[m_{hh}^{3/2} + m_{lh}^{3/2}\right] \\ B &= \left[\sum_v \left(\frac{2m_{c,v}}{m_c}\right)^{3/2}\right] \frac{E_g}{K_{hh}(T)} \frac{\sqrt{\pi}}{2} (k_BT)^{3/2} \end{aligned} \tag{C.2}$$

- For a n-doped semiconductor, p_0 is negligible in front of n_0 and if we denote by B_1 the result of the summation in the previous expression of B, we have

$$\tau_{rad}(T) = \frac{1}{\sqrt{\pi}\left(\frac{m_c}{2\pi\hbar^2}\right)^{3/2} B_1 \frac{E_g}{K_{hh}(T)} (k_BT)^3 \exp\left(\frac{E_f - E_c}{k_BT}\right)} \propto \frac{1}{E_g(T)} \exp\left(\frac{E_c - E_f}{k_BT}\right) \tag{C.3}$$

- For a p-doped semiconductor, n_0 is negligible in front of p_0 and we have

$$\frac{p_0}{K_{hh}(T)} = \frac{2\left(\frac{k_BT}{2\pi\hbar^2}\right)^{3/2} \exp\left(\frac{E_{hh} - E_f}{k_BT}\right)}{\left(\frac{k_B^3 T^3 c^3 \varepsilon_0 \hbar}{n_r e^2 M_b^2}\right)} \propto (k_BT)^{-3/2} \exp\left(\frac{E_{hh} - E_f}{k_BT}\right) \tag{C.4}$$

  which leads us to

$$\tau_{rad}(T) \propto \frac{1}{B_1 E_g \frac{p_0}{K_{hh}(T)} \frac{\sqrt{\pi}}{2} (k_BT)^{3/2}} \propto \frac{1}{E_g(T)} \exp\left(\frac{E_f - E_{hh}}{k_BT}\right) \tag{C.5}$$

We could have use $n_0 \approx N_D$ or $p_0 \approx N_A$ during the calculations but these approximations would help only if we consider the doping concentrations to be independent of the temperature. In the case where this condition is verified, the steady-state radiative lifetime is $\tau_{rad} \propto T^{3/2}$.

APPENDIX D COMPUTATION OF THE SHOCKLEY-READ-HALL RECOMBINATION RATE

The different steps presented here are based on the well-developed approach from Shockley and Read article [147]. Here, this approach is just extended to the case of degenerate semiconductors. The total rate of electron capture in the trap level of energy E_t is represented by the symbol U_{cn} and given by [147]

$$U_{cn} = f_{pt} N_t \Big[1 - \exp\Big(\frac{\mu_t - \mu_e}{k_B T}\Big)\Big] \int_{E_c}^{\infty} f(E) N(E) c_n(E) \mathrm{d}E \tag{D.1}$$

In this equation, f represents the Fermi-Dirac distribution, and $f_{pt} = 1 - f(E_t)$ is the probability that a trap is empty. μ_e and μ_t are the quasi-Fermi levels for the electrons in the conduction band and the traps level, respectively. $N(E)\mathrm{d}E$ is the total number of quantum states in the energy range $\mathrm{d}E$ and N_t the density of trapping centers per unit volume. $c_n(E)$ is defined as the average probability per unit time for an electron in the range $\mathrm{d}E$ to be captured by an empty trap. E_c is, as usual, the conduction band edge.

Let us write the electron carrier density n as $N_c \exp\left(\frac{\mu_e - E_c}{k_B T}\right)$ with N_c given in equation (D.2).

$$N_c = \int_{E_c}^{\infty} f(E) N(E) \exp\Big(\frac{E_c - \mu_e}{k_B T}\Big) \mathrm{d}E \tag{D.2}$$

With this definition, we have

$$\begin{aligned}
U_{cn} &= \frac{n}{n} f_{pt} N_t \Big[1 - \exp\Big(\frac{\mu_t - \mu_e}{k_B T}\Big)\Big] \int_{E_c}^{\infty} f(E) N(E) c_n(E) \mathrm{d}E \\
&= \frac{n}{N_c \exp\left(\frac{\mu_e - E_c}{k_B T}\right)} f_{pt} N_t \Big[1 - \exp\Big(\frac{\mu_t - \mu_e}{k_B T}\Big)\Big] \int_{E_c}^{\infty} f(E) N(E) c_n(E) \mathrm{d}E \\
&= f_{pt} N_t n \Big[1 - \exp\Big(\frac{\mu_t - \mu_e}{k_B T}\Big)\Big] \Big[\frac{1}{N_c} \int_{E_c}^{\infty} f(E) \exp\Big(\frac{E_c - \mu_e}{k_B T}\Big) N(E) c_n(E) \mathrm{d}E\Big] \\
&= f_{pt} N_t n \Big[1 - \exp\Big(\frac{\mu_t - \mu_e}{k_B T}\Big)\Big] \langle c_n \rangle \\
U_{cn} &= \Big[1 - \exp\Big(\frac{\mu_t - \mu_e}{k_B T}\Big)\Big] f_{pt} n C_n
\end{aligned} \tag{D.3}$$

As mentioned above, the quantity f_{pt} is linked to the function f_t, and the relation between them is

$$f_{pt} = 1 - f_t = f_t \exp\left(\frac{E_t - \mu_e}{k_B T}\right) \tag{D.4}$$

.

After injecting equation (D.4) in equation (D.3), we find

$$U_{cn} = C_n(f_{pt} n - f_t n_1) \tag{D.5}$$

, where $n_1 = N_c \exp\left[(E_t - E_c)/k_B T\right]$, is the electrons charge concentration in the conduction band for the case in which the Fermi level falls at E_t.

Equation (D.5) is the same as equation (3.8) in [147]. This equation has the merit of not relying on a specific type of band structure. It was derived with arbitrary band structures. We showed that no specific assumption has to be made on the semiconductor to establish it. All the complexities in this equation are hidden behind the estimation of the quantities C_n, N_c, N_t, and E_t. For non-degenerate semiconductors, equation (D.2) becomes equation (D.6), and the quantities mentioned before are estimated the same way as in [147].

$$N_c = \int_{E_c}^{\infty} N(E) \exp\left(\frac{E_c - E}{k_B T}\right) \mathrm{d}E \tag{D.6}$$